

*The beauty of a living thing is not the atoms that go into it,
but the way those atoms are put together.*

— Carl Sagan

University of Alberta

Microscopic Superfluidity in Small Helium Clusters Doped with
Hydrogen Cyanide

by

Steve Peter Dempster

A thesis submitted to the Faculty of Graduate Studies and Research
in partial fulfillment of the requirements for the degree of

Master of Science

Department of Chemistry

©Steve Peter Dempster
Fall 2012
Edmonton, Alberta

Permission is hereby granted to the University of Alberta Libraries to reproduce single copies of this thesis and to lend or sell such copies for private, scholarly or scientific research purposes only. Where the thesis is converted to, or otherwise made available in digital form, the University of Alberta will advise potential users of the thesis of these terms.

The author reserves all other publication and other rights in association with the copyright in the thesis and, except as herein before provided, neither the thesis nor any substantial portion thereof may be printed or otherwise reproduced in any material form whatsoever without the author's prior written permission.

In memory of
Ryan Joseph Huskins
1983-2005

ABSTRACT

The construction and use of a broadband Fourier-transform microwave spectrometer utilizing linear frequency sweeps will be presented along with a brief theoretical description of its operation principle. This instrument and a narrowband, cavity-based spectrometer were used to measure the high resolution microwave spectra of the $J = 1-0$ transitions of small $\text{He}_N\text{-H}^{12}\text{C}^{14}\text{N}$, $\text{He}_N\text{-H}^{13}\text{C}^{14}\text{N}$, $\text{He}_N\text{-H}^{12}\text{C}^{15}\text{N}$, $\text{He}_N\text{-D}^{12}\text{C}^{14}\text{N}$, and $\text{He}_N\text{-D}^{13}\text{C}^{14}\text{N}$ clusters produced in a supersonic jet expansion. Spectroscopic analysis revealed that the observed effective rotational constants, B_{eff} , initially decreased with the number of the attached helium atoms before reaching a minimum at $N = 3$ helium atoms for all isotopologues. The subsequent increase in B_{eff} for $N \geq 4$ is indicative of the onset of microscopic superfluidity. Comparison of our experimental B_{eff} constants with those from quantum Monte Carlo simulations reveals a nearly congruent trend in B_{eff} up to $N = 6$. An analysis of the hyperfine structure of the ^{14}N containing isotopologues and the isotopic data is also provided.

ACKNOWLEDGEMENTS

I would like to express my sincerest gratitude towards my supervisor, Wolfgang Jäger. Over these past three years I've come to see him as less of a superior and more of a role model and mentor. Anyone who has had the privilege of working with Wolfgang would agree that he is a brilliant scientist, an excellent boss, and an okay table tennis player.

I am particularly grateful to Oleksandr Sukhorukov, without whom the CP-FTMW spectrometer would not have been built. Our relationship at times felt more like a rollercoaster ride than a typical postdoc-grad student mentorship, but I am truly indebted to his tutelage, guidance, and friendship. Wherever he is, I wish him all the best of luck in his endeavors.

In regards to my research, I would like thank Roman Lipiecki, Qi-Yi Lei, Gary Grubbs II, Stephen Cooke, Jennifer van Wijngaarden, Steven Shipman, and Johannes Rebling for their contribution in the construction of the new CP-FTMW spectrometer. I would also like to express my appreciation to Eric Rivard, Gary Douberly and Jason Dibbs for their help with the synthesis of hydrogen cyanide—thanks to them I am alive and currently goiter free! And, of course, for discussions regarding their quantum Monte Carlo simulations, I would like to thank David Farrelly, Stefano Baroni, and Stefano Paolini.

I would also like to acknowledge Yunjie Xu for her valuable and helpful suggestions on the analysis of spectroscopic data. A big thank you to my supervisory committee, Eric Rivard and Rod Wasylshen, for their sage advice and counsel provided innumerable times during the course of my graduate studies. To my academic family, the Jäger and Xu groups, I am grateful for their much needed support and friendship.

Finally, I am deeply indebted to the emotional support provided by my family and close friends. In particular, I am grateful to my loving parents for their continual support and encouragement. And, on behalf on my sanity, I must also thank Zahra Dezhahang, Sarah Hamilton, Yonghoon Kwon, Adam Malcolm, and Mohammad Reza Poopari—I could not have done this without your friendship.

TABLE OF CONTENTS

CHAPTER 1: INTRODUCTION	1
1.1 A New State of Matter	1
1.1.1 Superfluidity	1
1.1.2 Liquid Helium.....	2
1.1.3 Two-Fluid Model	3
1.2 Microscopic Superfluidity	4
1.2.1 Helium Nanodroplet Spectroscopy	4
1.2.2 Evidence of Microscopic Superfluidity	6
1.2.3 From Clusters to Solvated Molecules	8
1.2.4 Hydrogen Cyanide: A Molecular Probe	10
1.3 Outline of This Study	12
CHAPTER 2: EXPERIMENTAL CONSIDERATIONS	13
2.1 Sample Preparation	13
2.1.1 Synthesis of Hydrogen Cyanide.....	13
a) <i>Dangers and safety precautions</i>	13
b) <i>Synthesis</i>	15
c) <i>Isotopologues</i>	17
d) <i>Disposal</i>	17
e) <i>Alternate synthesis</i>	18
2.1.2 Generation of Clusters	18
a) <i>Sample concentrations</i>	18
b) <i>Supersonic jet-expansion</i>	18
c) <i>Complex Formation</i>	20

2.2 Microwave Spectroscopy.....	21
2.2.1 Theory.....	21
a) <i>Rigid rotor</i>	21
b) <i>Transition dipole moment</i>	22
c) <i>Semi-rigid linear rotor</i>	23
d) <i>Population of states</i>	24
e) <i>Hyperfine structure</i>	25
f) <i>Kraitchman coordinates</i>	27
2.2.2 Transition Dynamics.....	28
a) <i>Relevance</i>	28
b) <i>Superposition states</i>	28
c) <i>Rabi frequency and detuning</i>	30
d) <i>Ensemble average and density matrix</i>	32
e) <i>Optical Bloch equations</i>	34
f) <i>Relaxation processes</i>	36
2.3 Balle-Flygare Cavity Fourier-Transform Microwave Spectrometer.....	38
2.3.1 Theoretical Description.....	39
a) <i>Single rigid rotor</i>	39
b) <i>Transient absorption</i>	39
c) <i>Transient emission</i>	42
2.3.2 Instrument Design.....	43
a) <i>Fabry-Pérot cavity</i>	46
b) <i>Excitation pulse</i>	48
c) <i>Double superheterodyne detection</i>	48
d) <i>Timing</i>	49
2.4 Chirped-Pulse Broadband Fourier-Transform Microwave Spectrometer.....	51
2.4.1 Theoretical Description.....	52

	a) <i>Fast passage</i>	52
	b) <i>Emission signal</i>	56
2.4.2	Instrument Design.....	57
	a) <i>Chirp excitation pulse</i>	59
	b) <i>Sample chamber</i>	59
	c) <i>Detection system</i>	60
	d) <i>Timing</i>	63
2.4.3	Optimization.....	63

**CHAPTER 3: THE STUDY OF HYDROGEN CYANIDE EMBEDDED
IN SMALL HELIUM-4 CLUSTERS USING FOURIER-TRANSFORM
MICROWAVE SPECTROSCOPY..... 65**

3.1	Introduction.....	65
3.1.1	Previous Work.....	65
3.1.2	Theoretical Predictions.....	66
3.2	Experimental.....	68
3.3	Results and Discussion.....	69
3.3.1	Rotational Spectra.....	69
3.3.2	Rotational Constants.....	75
3.3.3	¹⁴ N Nuclear Quadrupole Hyperfine Structure.....	80
3.3.4	Helium Density Distribution.....	83
3.4	Summary.....	86

CHAPTER 4: CONCLUDING REMARKS..... 87

BIBLIOGRAPHY..... 89

LIST OF TABLES

Table 3.1 Measured frequencies of the α -type, $J = 1-0$, rotational transitions (in MHz) of $\text{He}_N\text{-HCN}$ clusters and its isotopologues.....	74
Table 3.2 Summary of the ^{14}N nuclear quadrupole coupling constants, χ_{aa} , in MHz and $P_2(\cos\theta)$ values for the ^{14}N containing isotopologues of $\text{He}_N\text{-HCN}$ clusters	81
Table 3.3 The $ z $ coordinates of $\text{He}_N\text{-HCN}$ determined by the Kraitchman substitution procedure.....	84
Table 3.4 A comparison of the molecular radii, r_s , determined from Kraitchman substitution analysis, of two light rotors (HCN and CO) and two heavy rotors (OCS and N_2O) weakly bound to $N^4\text{He}$ atoms	84

LIST OF FIGURES

Figure 2.1 Diagram of apparatus used in the synthesis of HCN.....	16
Figure 2.2 A comparison of various superposition states composed of the $J = 0$ and $J = 1$ stationary states of a rigid rotor.....	31
Figure 2.3 The Bloch variables of an ensemble of HCN molecules exposed to a monochromatic pulse of radiation.....	41
Figure 2.4 The Feynman-Vernon-Hellwarth representation of the response of an ensemble of HCN molecules to a microwave pulse either (a) on resonance or (b) near resonance.....	42
Figure 2.5 A schematic diagram of the Balle-Flygare Fourier-transform microwave spectrometer	44
Figure 2.6 A typical pulse sequence used in the Balle-Flygare Fourier-transform microwave spectrometer	45
Figure 2.7 The Bloch variables of an ensemble of OCS (left) and HCN (right) molecules in response to identical chirped-pulses optimized for the OCS $J = 1 \leftarrow 0$ transition	54
Figure 2.8 A Feynman-Vernon-Hellwarth representation of the transition dynamics of (a) OCS and (b) HCN molecules during a chirped-pulse optimized for the OCS $J = 1 \leftarrow 0$ transition	55

Figure 2.9 The Bloch variables of an ensemble of OCS (left) and HCN (right) molecules in response to identical chirped-pulses optimized for the HCN $J = 1 \leftarrow 0$ transition	56
Figure 2.10 A schematic diagram of the broadband chirped-pulse Fourier transform microwave spectrometer.....	58
Figure 2.11 A comparison of an actual rotational spectrum during a 0.2–1 GHz chirp pulse centered on ν and the “folded” spectrum observed after mixing down the broadband signal with ν	61
Figure 2.12 A typical pulse sequence used in the chirped-pulse Fourier-transform microwave spectrometer	62
Figure 3.1 The pressure dependence of the a -type, $J = 1-0$, transitions of He_N -HCN clusters with $N = 1$ to 5, recorded on the broadband CP-FTMW spectrometer	70
Figure 3.2 A comparison of the $J = 1-0$ transition of He_6 -HCN measured on the cavity FTMW spectrometer for the most abundant isotopologue, HCN, and HC^{15}N	72
Figure 3.3 The high resolution spectrum of $J = 1-0$ transition of He_7 -DCN measured on the cavity FTMW spectrometer.....	73
Figure 3.4 The effective rotational constants, B_{eff} , plotted against the number of ^4He atoms, N , of several isotopologues of He_N -HCN clusters	75
Figure 3.5 Incremental moments of inertia, $\Delta I = I_N - I_{N-1}$, for He_N -DCN and He_N -CO clusters.....	77

Figure 3.6 Comparison of the effective rotational constants, B_{eff} , of $\text{He}_N\text{-HCN}$ clusters from experiment with previous theoretical predictions 79

Figure 3.7 A comparison of $P_2(\cos \theta)$ values from the ^{14}N hyperfine structures of rotational transitions of $\text{He}_N\text{-HCN}$, $\text{He}_N\text{-N}_2\text{O}$, and $\text{He}_N\text{-HCCCN}$ isotopologues as a function of cluster size 82

LIST OF SYMBOLS

α	sweep rate
γ	heat capacity ratio
$\underline{\Gamma}$	matrix representation of a phenomenological relaxation term
$\Delta(t)$	detuning frequency
$\Delta\nu$	frequency bandwidth
$\Delta\nu_{ch}$	chirp bandwidth
$\Delta\nu_D$	Doppler splitting width
$\Delta\nu_m$	offset of molecular emission signal from the incident frequency
Δm	mass change upon isotopic substitution
Δ_0	initial detuning
Δ_f	final detuning
$\vec{\mathcal{E}}(t)$	electric field
\mathcal{E}_0	magnitude of electric field
θ	azimuthal angle
$\vec{\Theta}(t)$	Bloch vector
$\vec{\Theta}_{eq}$	vector representation of a phenomenological correction term
μ	electric dipole moment; reduced mass
$\underline{\mu}$	transition dipole matrix
$\overline{\mu}_g$	projection of the electric dipole operator along the g -axis
$\overline{\mu}_{g_{f \leftarrow i}}$	transition dipole moment between $ i\rangle$ and $ f\rangle$ along the g -axis
$\langle \vec{\mu} \rangle$	average transition dipole moment
ν	frequency of radiation

$\nu_{J+1 \leftarrow J}$	transition frequency between rotational states J and $J + 1$
ν_m	molecular emission frequency
$\underline{\rho}$	density matrix
$^1\Sigma$	singlet, electronic ground state term symbol
τ	pulse length
τ_c	cavity decay constant
$\vec{Y}(t)$	torque vector
ϕ	polar angle; phase of electric field
$\chi_0, \chi_{gg}, e q Q$	electric nuclear quadrupole coupling constant
ψ	time-independent wavefunction
$\psi(\theta, \phi)$	angular wavefunction
Ψ	total wavefunction; superposition wavefunction
$\omega, \omega(t)$	angular frequency of radiation
ω_{21}	transition (angular) frequency between $ 1\rangle$ and $ 2\rangle$
$\Omega(t)$	Rabi frequency
B, \tilde{B}	rotational constant in energy or frequency units, respectively
B_0	gas phase rotational constant for ground vibrational state
B_{eff}	effective rotational constant of He_N -molecule cluster or molecule embedded in ^4He nanodroplet
c	speed of light
$c_i, a_{i,N}$	probability amplitude
C	$C = F(F + 1) - I(I + 1) - J(J + 1)$
C_P, C_V	heat capacity at constant pressure and volume, respectively
D, \tilde{D}, D_J, H	centrifugal distortion constants
E_Q	nuclear quadrupole interaction energy

E_J^{rr}	energy for the rigid rotor J rotational state
$f(I, J, F)$	Casimir's function
F	total angular momentum quantum number
h, \hbar	Planck constant
\hat{H}	Hamiltonian matrix
\hat{H}_0	time-independent energy operator
\hat{H}_0, \hat{H}_1	the time-independent and time-dependent Hamiltonian matrix
I	nuclear spin quantum number
\hat{I}	moment of inertia tensor
J	rotational quantum number
\vec{k}	wavevector
k_B	Boltzmann constant
m, m_i, M	mass
m, M_J	magnetic quantum number
M	Mach number
N	number of particles
\vec{P}	macroscopic polarization
$P_J^{ m }$	associated Legendre function
$\langle P_2(\cos \theta) \rangle$	average second-order Legendre polynomial of $\cos \theta$
q	electric field gradient
Q	electric quadrupole moment; quality factor
r	radial distance
r_s	molecular radial distance determined from substitution analysis
t	time

T	absolute temperature
T_λ	lambda point or superfluid transition temperature
T_1	relaxation time of the ensemble population difference to w_{eq}
T_2	relaxation time related to the loss of ensemble coherence
T_B	Bose-Einstein condensation temperature
T_{tr}, T_{rot}, T_{vib}	translational, rotational, and vibrational temperatures, respectively
$u(t), v(t)$	Bloch variables relating to the coherence of an ensemble
v^*	most probable velocity in a Maxwell distribution of speeds
$w(t)$	Bloch variable relating to the ensemble population difference
w_0, w_{eq}	Boltzmann equilibrium population difference
w_f	final population difference
$Y_J^m(\theta, \phi)$	spherical harmonic function
$ z $	Kraitchman substitution coordinates

LIST OF ABBREVIATIONS

A/D	analog-to-digital converter
ATP	adenosine triphosphate
AWG	arbitrary waveform generator
BEC	Bose-Einstein condensation
c.o.m.	center of mass
CP-FTMW	chirped-pulse Fourier-transform microwave
DMC	diffusion Monte Carlo
EPR	electron paramagnetic resonance
FTMW	Fourier-transform microwave
FVH	Feynman-Vernon-Hellwarth
HENDI	helium nanodroplet isolation
IF	intermediate frequency
IR	infrared
NMR	nuclear magnetic resonance
PDRO	phase-locked dielectric resonator oscillator
PES	potential energy surface
PIN	<i>p-i-n</i> diode
POITSE	projector operator imaginary-time spectral evolution
ppm	parts per million
RAP	rapid adiabatic passage
RBDMC	rigid body diffusion Monte Carlo
RBF	round bottom flask
RF	radio frequency

Rg	rare gas
RQMC	reputation quantum Monte Carlo
RWA	rotating wave approximation
SACI-FTMW	search accelerated correct intensity Fourier-transform microwave
S/N	signal-to-noise
SPST	single-pole-single-throw
TTL	transistor-transistor logic
UV	ultraviolet

CHAPTER 1: INTRODUCTION

1.1 A New State of Matter

1.1.1 Superfluidity

Under specific conditions, such as tremendously low temperatures or extremely high densities, a new state of matter emerges: the *superfluid*. This remarkable phase transition has been observed in liquid helium at temperatures approaching absolute zero [1-4] and its pervasiveness in nature is far reaching. For example, the concept of superfluidity has been used to explain phenomena related to the constituents of matter itself, like the pairing of nucleons within atomic nuclei [5], to even the behaviour of celestial bodies, as in the periodicity of pulsar emissions [6].

Now as impressive as these statements are, they fail to satisfy the lingering question that undoubtedly plagues the uninitiated: what *is* a superfluid? Strictly speaking, a superfluid is characterized as having neither viscosity nor entropy and, thus, is a highly ordered and coherent system where all the individual constituents (whether they be protons, neutrons, atoms, or even molecules) can be described by a single macroscopic wavefunction [6]. In the case of liquid helium, specifically the helium-4 isotope, once the transition temperature T_λ has been reached, this coherent behaviour begins to manifest itself in the form of several bizarre properties, including the Fountain effect [7], Rollin film [8], quantized vortices and the propagation of additional sound modes [6, 9].

So how is superfluidity achieved? It should come as no surprise that a rigorous treatment of such a puzzling phenomenon would be long, complicated and far beyond the scope of this work. So, for the sake of brevity, only a qualitative description will be given. It turns out the mechanism of superfluidity depends on which class the constituent particles fall under: *fermions* or *bosons*?

This classification represents a fundamental dichotomy of nature with the distinction being the spin quantum number. If the spin of a particle is half-integer valued, then it is classified as a fermion and, therefore, obeys Fermi-Dirac statistics [6]. Chemists are all too familiar with fermions as a few notable examples include protons, neutrons and, of course, electrons. Additionally, particles of half-integer spin, such as electrons, are described by an anti-symmetric wavefunction with respect to exchange, which forbids two particles from occupying the same quantum state. This provides a more general extension of the Pauli Exclusion Principle to not just electrons, but to all fermions.

Bosons, on the other hand, correspond to particles with integer spin and are governed by Bose-Einstein statistics. Succinctly put, bosons do not follow the Pauli Exclusion Principle, meaning that multiple particles can coexist in the same state. This is a direct result of the exchange symmetry of the bosonic wavefunction [6].

The contrasting behaviour of fermions and bosons is best exemplified by the two stable isotopes of helium at low temperatures. In fact, so far the only bulk superfluids observed at liquid-like densities have been ^3He (its nuclear spin, I , is $\frac{1}{2}$ and it is thus a fermion) and ^4He (a boson with $I = 0$). Therefore, a brief discussion on the inviscid phase of each helium isotope would provide an appropriate description of how superfluidity is achieved in these disparate systems.

1.1.2 *Liquid Helium*

Below 2.17 K liquid ^4He begins to display non-classical behaviour. This transition is marked by a sharp increase in the specific heat capacity as the temperature drops and is aptly referred to as the *lambda point*, T_λ —since a plot of the specific heat versus temperature bears a striking resemblance to the Greek letter lambda. By convention, the *normal* liquid existing above T_λ is known as helium I, while the non-classical fluid that forms below the lambda point is referred to as helium II [6].

It was realised in 1938 that the behaviour of the He II phase was a result of superfluidity [1, 2] and that the transition at T_λ is closely related to Bose-Einstein condensation (BEC) [10]. To elaborate, BEC occurs when the individual particles of a weakly interacting boson gas begin to occupy the lowest energy level as the temperature approaches absolute zero. Since bosons do not abide by the Pauli Exclusion Principle, below a critical temperature, T_B , a significant portion of the ensemble *condense* into the ground quantum state. Consequently, the individual particles of the condensate become indistinguishable amongst the collective and are thereby described by a single macroscopic wavefunction [6].

For the purpose of this study, the microscopic description of BEC provides a sufficient, qualitative mechanism for superfluidity in He II. However, it is worth noting that superfluid ^4He is different than a Bose-Einstein condensate and the disparity lies in the non-ideal, attractive interatomic forces of helium-4. Reference [6] provides a more complete description of superfluidity in liquid ^4He .

As mentioned above, the helium-3 isotope is a fermion due to its half-integer nuclear spin. The superfluid phases of ^3He were discovered in 1972 by Osheroff *et al.* [3, 4], with a staggeringly low transition temperature of ~ 2.5 mK. At these low temperatures, the movement of the atoms begin to couple with one another through their nuclear magnetic moments and leads to pairing of ^3He atoms. Consequently, the total spin for these coupled pairs becomes an integer value and they accordingly form a composite boson [6, 9]. (This is analogous to the formation of “Cooper pairs” of electrons in superconductors, according to the theory proposed by Bardeen, Cooper and Schrieffer [11].) The onset of superfluidity in helium-3 then occurs by condensation of these composite bosons as described above for BEC.

1.1.3 Two-Fluid Model

It is worthwhile to address the very strange and somewhat inconsistent behaviour observed in bulk He II. For example, a container of liquid ^4He cooled to temperatures below T_λ will exhibit super flow if the contents are forced through a narrow capillary. However, if the viscosity of the liquid is determined by

another method, for example, by measuring the resistance of a moving object within the medium, then a rather different observation is made [9]. In fact, the drag force experienced by the object in liquid ^4He is roughly the same just above and below the lambda point.

These opposing observations can be explained phenomenologically in terms of the *two-fluid model*, where He II can be considered as a concoction of two different liquids: a classical, normal fluid and a superfluid. As previously mentioned, the superfluid has zero viscosity and no entropy and, for that reason, only the normal fluid possesses these properties. Each component has its own mass density and local velocity, and yet it is impossible to isolate either constituent from the mixture [6, 9].

In an experiment by Andronikashvili [12], however, it proved possible to actually measure the fraction of each fluid in He II as a function of temperature. This was accomplished by submerging a stack of thin discs, connected by a thin fibre, into a vessel containing liquid helium-4 and measuring the frequency of rotation. The spacing between discs was sufficiently narrow to *trap* any normal fluid, which would in turn oscillate with the assembly and contribute to the total moment of inertia—that is, its rotational resistance. As the temperature was lowered, Andronikashvili found that the oscillation frequency increased dramatically and that this response corresponded with a concomitant reduction of the normal fluid fraction. By simply relating the oscillator periodicity to its moment of inertia, the normal fluid fraction was determined and, by doing so, proved the validity of the two-fluid model.

1.2 Microscopic Superfluidity

1.2.1 Helium Nanodroplet Spectroscopy

Without a doubt, the most significant application of superfluid helium to physical chemistry has been in its use in molecular beam experiments, such as helium nanodroplet isolation (HENDI) spectroscopy [13]. One of the key aspects

of the HENDI technique is the formation of microscopic droplets of helium that can be as small as several hundred and as large as several million atoms. Their diameter is given by the relation $r(\text{Å}) = 2.22N^{1/3}$, and is in the nanometer range, hence the term *nanodroplet*. Creation of these nanodroplets is achieved through supersonic expansion of a cooled helium gas into an evacuated chamber [14]. The source of the molecular beam is provided by a cooled pinhole-nozzle (orifice diameter $\sim 5\mu\text{m}$, $T < 40\text{ K}$) with a backing pressure ranging from 20 to 100 bar.

The composition of the nanodroplet can either be isotopically pure (i.e., consisting of only ^3He or ^4He) or mixed, and greatly influences the final temperature of the droplet. For example, pure nanodroplets of ^4He reach a final temperature of 0.38 K, while mixed or pure ^3He achieve temperatures of 0.15 K [14, 15]. What makes helium nanodroplets such an attractive matrix in which to perform isolation spectroscopy of solvated molecules, is the promise of ultra-cold temperatures, a weakly-interacting helium environment, an optically transparent solvent (for frequencies below vacuum UV) and the ability to study individually isolated impurity molecules [14-17].

In HENDI experiments, the molecular beam travels through a long evacuated chamber partitioned by several compartments. As the nanodroplets traverse the instrument, they capture an impurity molecule by crossing through a “pick-up” cell containing a dilute vapour of a particular molecular species (typical pressures are on the order of 0.1 μbar for pick-up cells only a few centimeters wide) [14]. The kinetic and internal energies of the embedded molecule are rapidly dissipated by evaporative cooling of He atoms. With a series of adjacent pick-up cells, each with different chemical species, the droplets can systematically be doped multiple times, allowing the formation of tailor-made clusters. A few examples of these novel complexes created in helium nanodroplets include Ar_N -tetracene ($N = 1-5$) [18], $(\text{H}_2)_N$ -OCS ($N = 1-16$) [19, 20] and even end-to-end chains consisting of hydrogen cyanide (HCN) [21].

The rotational or vibrational spectrum of the impurity molecule or complex, for example, can be indirectly measured by monitoring the signal recorded by either a mass spectrometer or a bolometer. In one particular

instrument design [15], the seeded nanodroplets are probed by a collinear, counter-propagating laser beam of variable frequency. Absorption of a single photon by the embedded chromophore results in rapid evaporation of He atoms from the nanodroplet and, thus, a depletion of the mass spectrometer signal.

1.2.2 Evidence of Microscopic Superfluidity

One of the first indications that helium nanodroplets were potentially superfluid was in the high-resolution infrared (IR) spectrum of sulfur hexafluoride (SF_6) embedded in approximately 3000 ^4He atoms [22]. Typically in condensed phase spectroscopic measurements, the fine rotational structure is ill-defined due to non-uniform interactions of solute molecules with their local environment, which, in turn, causes significant line broadening. However, in the helium nanodroplet study, not only were the rotational lines resolved, but the spacing between these transitions—which is dependent on the rotational constant, B , of the molecule—was significantly reduced when compared the gas phase spectrum of SF_6 . The former observation revealed that the local helium environment facilitated rotational coherence of the impurity molecule. Unfortunately, it was unclear at the time whether this behaviour of the ^4He nanodroplets was due to the extremely weak interactions of the helium solvent or the existence of a superfluid phase [17].

The answer came a few years later in an elegant study by Grebenev *et al.*, dubbed the “microscopic Andronikashvili experiment” [23]. The authors measured the high resolution IR spectrum of carbonyl sulfide (OCS) in pure nanodroplets of ^4He and observed similar results as in the SF_6 study—namely resolved rotational lines with narrower spacing when compared to the gas phase spectrum. However, when the same experiment was repeated with ^3He nanodroplets, which is not superfluid under these experimental conditions, the sharp lines were replaced by a broad feature. The authors found that the rotational lines were restored with the addition of ~ 60 ^4He atoms to the nonsuperfluid ^3He droplet and attributed this as the minimum number of ^4He atoms required for the superfluid phase to manifest itself. This also showed that the embedded OCS

molecule was insulated from the bulk of the nanodroplet by approximately two solvation shells of superfluid ^4He .

Since these early pioneering studies, a considerable number of molecules embedded in superfluid helium nanodroplets have been investigated. Yet despite the rich spectroscopic information available, a complete proper description of the interactions between the ^4He *quantum* solvent and the impurity is still lacking. This can be seen by the measured rotational dynamics of the embedded chromophores. As mentioned previously, the rotational constant B —which is inversely proportional to the moment of inertia—of helium solvated molecules can be considerably reduced, or *renormalized*, compared to the gas phase value. However, for other molecules the extent of renormalization can be negligible. Furthermore, it appears that in general the heavier molecules (termed *heavy rotors*; e.g., SF_6 and OCS) experience greater renormalization than lighter molecules (*light rotors*; e.g., HF and H_2O).

For physical explanation of these results, two molecular properties of the chromophore can be considered: the magnitude of its gas phase rotational constant, B_0 , and the anisotropy of the He–molecule interaction potential energy surface (PES)—a measure of the interaction strength between solute and solvent as function of separation and orientation [24]. To elaborate on the second point, if there is a strong interaction between the impurity molecule and the superfluid He solvent, then a portion of the helium density will become localised near the molecule and dragged along with the molecular rotation [25]. Thus, the embedded molecule induces a local nonsuperfluid fraction. Now if the movement of the molecule is relatively slow, i.e., B_0 is small, then the localised helium density can “adiabatically follow” the molecular rotation and, therefore, contribute to the effective moment of inertia [24]. In the case of light rotors, the rotation is too fast for the helium density to *keep up*. This description helps explain the previously noted trend for heavy and light rotors but fails to accurately predict the extent of renormalization.

Theoretical studies utilizing path integral and diffusion Monte Carlo simulations on solvated molecules have provided considerable advances in our

understanding of microscopic superfluidity and quantum solvation [24-26]. However, the success of theoretical simulations in predicting the spectra of solvated species is greatly limited by the accuracy of the He–molecule and He–He PESs used [27]. It is of great importance to understand the delicate interplay between the molecular properties of a solvated impurity and the observed spectroscopic features. For one, this knowledge would provide a better interpretation of experimental results and allow the gas phase spectra of tailor-made species, which typically cannot be synthesized by conventional methods, to be accurately predicted [27]. More importantly, the embedded chromophores can be used to probe the dynamics of the quantum solvent and provide valuable information on confined quantum systems and microscopic superfluidity [16].

1.2.3 From Clusters to Solvated Molecules

Spectroscopic measurements of weakly bound molecular dimers can provide a wealth of information about the nature and strength of the intermolecular interactions between the two species [28, 29]. (By convention these systems are dubbed as *dimers* since the complex consists of two separate molecules or atoms, and with larger cluster sizes it is common to adopt a similar nomenclature, e.g., *trimers*, *tetramers*, etc.) Such weakly bound systems are often referred to as *van der Waals molecules* given that the complex is usually bound merely by London dispersion forces and are readily formed in seeded jet expansions, along with larger aggregates [30]. By monitoring the progression of spectroscopic constants as the number of binding partners increase and the weakly bound clusters evolve from a van der Waals molecule to a solvated molecule, one can track the emergence and evolution of certain bulk properties on microscopic scales.

In a key study by Tang *et al.* [31], the microwave and high-resolution IR spectra of small $\text{He}_N\text{-OCS}$ clusters (with N , the number of solvating helium atoms, from 2 to 8) were measured with the hope of detecting the spectroscopic signatures of microscopic superfluidity. Analysis of their data revealed that the rotational constants of the cluster monotonically decrease with the addition of

helium atoms. What was particularly remarkable about this trend was that the value of the rotational constants becomes lower than the measured nanodroplet limit ($N \sim 10^4$) for clusters with $N > 5$. This implied that at some point beyond $N = 8$ the rotational constants must increase—in other words, the moment of inertia would have to decrease—in order to approach the asymptotic value measured in helium nanodroplets. Since such behaviour cannot be explained by classical mechanics, it must represent the emergence of a superfluid phase.

Additional spectroscopic experiments on $\text{He}_N\text{-OCS}$ clusters, with N reaching 72 ^4He atoms, were done in the IR and microwave ranges [32-35]. It was found that the effective rotational constants of the clusters decrease initially until a turnaround occurs at $N = 9$ with a following steep increase and subsequent oscillations. This non-classical behaviour clearly indicates decoupling of some helium density from the rotational motion of the OCS molecule and was taken as an indicator of the onset of microscopic superfluidity [31]. This interpretation was confirmed by subsequent theoretical simulations [36-38].

Suárez and coworkers [39] have suggested that the extent and the rate of renormalization in B_{eff} of molecules embedded in helium nanodroplets falls in three different regimes: heavy rotors, with low B_0 -values, experience a pronounced renormalization; light rotors, with large B_0 -values, and hence small renormalization; and an intermediate regime where both B_0 and the anisotropy of the interaction potential influence the degree of renormalization. It appears that this behaviour is also reflected in the characteristics of the smaller $\text{He}_N\text{-molecule}$ clusters, where helium density decouples from the rotational motion of a relatively lighter rotor at much smaller critical N -values than in the case of heavier molecules. Such is the case for $\text{He}_N\text{-CO}$, with the observed turnaround point at $N = 3$ [40-45].

The critical N -value and the evolution of B with N also depend sensitively on the He–molecule interaction potential, in particular its angular anisotropy. For example, the critical N values for $\text{He}_N\text{-CO}_2$ [46, 47], $\text{He}_N\text{-N}_2\text{O}$ [48-52], and $\text{He}_N\text{-HCCCN}$ [53] are at $N = 5, 8,$ and 9 , respectively. There has also been significant theoretical work aimed at understanding which factors influence the

renormalization of the rotational constants. For example, the $\text{He}_N\text{-N}_2\text{O}$ and $\text{He}_N\text{-HCCCN}$ simulations [49, 51, 53] could reproduce the trends in the rotational constants well up to cluster sizes of $N = 19$ and 30 , respectively. However, in the case of $\text{He}_N\text{-OCS}$, where experimental data are now available up to $N = 72$ [33], theory can reproduce the experimental trend only up to $N \sim 8$. In regards to $\text{He}_N\text{-N}_2\text{O}$ [52], $\text{He}_N\text{-CO}_2$ [46, 47], and $\text{He}_N\text{-OCS}$ [33], the experimental rotational constants show oscillatory behaviour with N after the turnaround with a concomitant slow approach to the nanodroplet limit. As of yet, these oscillations and the rather slow approach to the nanodroplet limit (probably at $N > 100$) have not been reproduced by simulations.

1.2.4 *Hydrogen Cyanide: A Molecular Probe*

Hydrogen cyanide has earned significant attention in scientific research. In prebiotic chemistry, it is speculated that HCN played an important role in the origins of molecular life as many biologically relevant molecules, e.g., amino acids and purines, are directly synthesized by reactions of HCN with aldehydes in the presence of ammonia (known as the *Strecker synthesis*) or simply by HCN polymerization (i.e. in the case of adenine) [54, 55]. In radio astronomy, the $J = 1 \rightarrow 0$ emission line of HCN is used to trace dense molecular gas in the interstellar medium, which are regions strongly associated with star formation [56]. Astronomers are able to measure the density of molecular clouds by exploiting the prevalence of HCN in the cosmos, its relatively high critical density (astronomical spectroscopy parlance for the local particle density required for the rate of spontaneous emission to equal the frequency of collisional de-excitation [57]), and a relatively high electric dipole moment.

In this study, however, hydrogen cyanide was chosen as a molecular probe to investigate the onset of microscopic fluidity in small clusters of ^4He . The question remains, why HCN? Why helium clusters? These questions are particularly valid when it is noted that considerable work has already been done with OCS [31-35], N_2O [50-52], CO_2 [46, 47, 58], HCCCN [53], and CO [40, 41] as molecular probes. Simply put, of all these $\text{He}_N\text{-molecule}$ systems only CO and

HCN fall within the intermediate size regime, as defined by Suárez and coworkers [39]. It is this class of rotors that proves to be the most difficult to model and, as experiments have shown, the extent of renormalization of these intermediate rotors shows the greatest variation of all the dynamical regimes [16]. Therefore, there is a clear need for more spectroscopic data on He_N -molecule clusters of this type. In the specific case of hydrogen cyanide, this is evidenced by the prediction of rotational energies for He_N -HCN clusters by three separate theoretical studies [59-61].

In addition, studying helium clusters seeded with hydrogen cyanide offers several significant experimental advantages. Measuring weakly bound clusters can be quite challenging as experimental conditions (e.g., concentration, backing pressure, molecular beam and microwave pulse duration, nozzle temperature, etc.) are critically important and must be each individually fine tuned to generate *and* detect clusters of a certain size distribution. To complicate matters further, the He_N -molecule clusters themselves are so weakly bound that typical probe-He distances are on the order of several angstroms and exhibit large amplitude bending motions. Consequently, predicting the rotational spectra of these van der Waals complexes and clusters is notoriously difficult and even state-of-the-art Monte Carlo simulations of rotational energies can be off by several GHz. Therefore, it is a significant advantage to choose a molecular probe with a high electric dipole moment like HCN, $\mu = 2.98$ D (compared to $\mu = 0.72$ D for OCS) [62], to increase signal intensity and, with that, the likelihood of discovering a cluster's rotational transition in a vast ocean of noise.

Another valuable property that HCN possesses is hyperfine splitting of rotational levels. The observed *hyperfine structure* is due to nuclear quadrupole coupling of the ^{14}N nucleus (nuclear spin $I = 1$) with the molecular rotation. This topic will be discussed in more detail in the subsequent section; however, suffice it to say, nuclear quadrupole splitting can yield structural information of the cluster when compared to that of the bare molecule—a potentially important point that might provide experimental evidence for incremental changes in helium density around HCN. Hyperfine structure does provide another advantage in

searching for ${}^4\text{He}_N\text{-HCN}$ rotational lines: a spectral fingerprint. This allows for one to immediately determine if the cluster contains a single HC^{14}N molecule or not, what type of transition (i.e., $J = 1-0$ or higher) was detected, and whether the signal is real or an artifact due to frequency mixing.

1.3 Outline of This Study

In total, this dissertation is separated into four chapters. The following section, Chapter 2, consists of the relevant experimental details and is further divided into four main subsections. The first of these, §2.1, describes the synthesis of hydrogen cyanide and information regarding the formation of small clusters of $\text{He}_N\text{-HCN}$ by means of a supersonic jet-expansion. Next, §2.2 provides a basic theoretical framework of microwave spectroscopy and transition dynamics that will be used through the remainder of this document. An overview of the narrowband, cavity-based Fourier-transform microwave spectrometer used in this study is given in §2.3, along with a brief theoretical description of its operation principle. A summary of the new broadband microwave spectrometer built as part of my Master's research project, specifically the relevant theory of its operation and the experimental design, is provided in §2.4.

The main focus of this study, probing microscopic fluidity in small clusters of $\text{He}_N\text{-HCN}$ using rotational spectroscopy, is concentrated in Chapter 3. This portion of my thesis includes a brief overview of previous work pertinent to my research; results obtained from rotational spectra of various isotopologues of $\text{He}_N\text{-HCN}$, such as, rotational constants, hyperfine structure parameters, and isotopic substitution analysis; and a discussion of the findings, possible interpretations, and comparisons with theoretical work where applicable. Finally, a brief summary is given in Chapter 4.

CHAPTER 2: EXPERIMENTAL CONSIDERATIONS

2.1 Sample Preparation

2.1.1 *Synthesis of Hydrogen Cyanide*

a) Dangers and safety precautions

One of the first obstacles encountered in my graduate research project was getting a hold of a sample of HCN gas. Despite having important industrial applications, (HCN is, for example, used in the production of methyl methacrylate and adiponitrile, a nylon precursor), and being produced on a million tonnes-per-annum scale globally [63], it is surprisingly difficult to purchase affordable, high purity HCN for research purposes. The only alternative was to produce my own—a seemingly simple and straight forward synthesis.

The challenge quickly became producing sufficient amounts of HCN without wiping out half of the Chemistry Department in the process, as poisoning is unquestionably a very real concern. HCN is readily absorbed through the skin and mucous membranes upon contact and can be immediately fatal if inhaled (270 ppm) or ingested (50–100 mg) [63, 64]. Once in the blood stream, HCN rapidly spreads through the body, inhibiting various enzymes including cytochrome oxidase—the last of four mitochondrial protein complexes that comprise the electron transport chain—thereby disrupting oxidative phosphorylation, ceasing adenosine triphosphate (ATP) production and causing histotoxic anoxia (inability of cells to utilize available oxygen) [54, 65]. This is the source of the ruddy complexion attributed to the first signs of cyanide poisoning. However, certain areas of the body, like the central nervous system, brain, and cardiovascular system, are particularly sensitive to cyanide intoxication. Symptoms of acute cyanide toxicity have been divided into 3 stages [66] and can occur within minutes of exposure:

1. Initial rapid breathing followed by shortness of breath, headache, vertigo, weak and rapid pulse, nausea, vomiting, and a staggering gait.
2. Convulsions, lockjaw, urination, and weaker and more rapid pulse rate.
3. Irregular, slow heartbeat; decreased body temperature; cyanosis (bluish discolouring) of the lips, face and extremities; coma; bloody saliva frothing from the mouth; and eventually death.

In fact, the rapid rate of poisoning essentially nullifies the use of an antidote after exposure to relatively large amounts of HCN—death can literally occur within minutes or even seconds. However, the body does have an endogenous cyanide detoxification mechanism in which the mitochondrial enzyme, rhodanese, catalyzes the conversion of cyanide (CN^-) into thiocyanate (SCN^-) which is roughly 300 times less toxic than HCN and is readily excreted in the urine [67]. Therefore, as long as a person is removed from the source of HCN, given that the amount inhaled, absorbed or consumed is insufficient to cause immediate death, a full recovery is possible with essentially no permanent damage.

Chronic exposure to cyanide, on the other hand, can result in optic nerve damage, hypertonia, and goiter formation [66]. It is interesting to note that when I started my graduate studies I had perfect vision whereas now, near the end of my degree, I wear glasses. (Not one to jump to conclusions, I am nervously waiting for the goiter to develop before confirming that this is due to cyanide poisoning.)

As if the prospect of deformity, blindness, and death were not enough discouragement, HCN can also undergo violent polymerization. This can occur when liquid HCN is heated to temperatures $\geq 50\text{ }^\circ\text{C}$, in contact with alkalis, exposed to an ignition source, or even spontaneously if stored for an extended period of time [64, 68-70]. This last, terrifying point can typically be avoided if an acid inhibitor, such as phosphoric acid, is present in the sample.

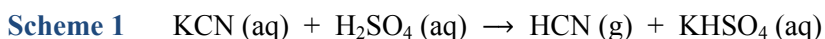
Now in light of all this unsettling information, it is obvious that the synthesis of HCN must be performed in contained reaction vessel with safety being a top priority. The apparatus constructed for synthesizing HCN is based on an original design provided by Gary Douberly (University of Georgia). The resulting

procedure and safety considerations, given below, were developed with the help of Eric Rivard (University of Alberta).

b) Synthesis

The HCN gas was produced under an inert helium atmosphere using the apparatus depicted in Figure 2.1. The amount of reagents used increased with each subsequent reaction. The most recent synthesis required over 4 grams of KCN and generated approximately 1.5 grams of HCN (or 86 % yield). The procedure for the initial reactions is given below.

Approximately 2.4 grams of KCN (Fluka Analytical, purity $\geq 97\%$) were dissolved in 25 mL of distilled water in the 100 mL round bottom flask (RBF), see Figure 2.1). After flushing the apparatus repeatedly with helium gas (Praxair, purity 99.995 %), 25 mL of 20% w/w H₂SO₄ solution was then added drop-wise to the contents of the RBF. The subsequent reaction follows that given in Scheme 1. A porous glass frit blowing helium gas was used to agitate the solution and help drive any evolving HCN gas through a drying tube, containing CaCl₂ (Fisher Chemical), before being condensed in a sample cold trap immersed in liquid nitrogen.



A gas bubbler system, consisting of three glass bulbs, was used to equalize the pressure inside the apparatus and maintain the inert atmosphere. The first is a mineral oil bubbler used to monitor the flow rate of helium gas, which is followed by an empty glass bulb and then a third bubbler containing a 10% w/w NaOH (Sigma-Aldrich, purity $\geq 97.0\%$) solution. The NaOH solution was a precautionary measure aimed at isolating any “escaping” HCN gas from the apparatus. The empty glass bulb was used to avoid any cross-contamination.

The hydrogen cyanide was collected over a 2 hour period. After this time, the helium gas flow was stopped, the reaction vessel isolated (refer to stopcock “C” in Figure 2.1), and the excess vapour was removed using a mechanical

vacuum pump. The vacuum line itself also contained a cold trap to prevent any HCN gas from reaching the vacuum pump and leaching into the oil or laboratory. For such reasons, the laboratory was equipped with a sensitive HCN gas sensor which would alarm if concentrations over 4.7 ppm were detected.

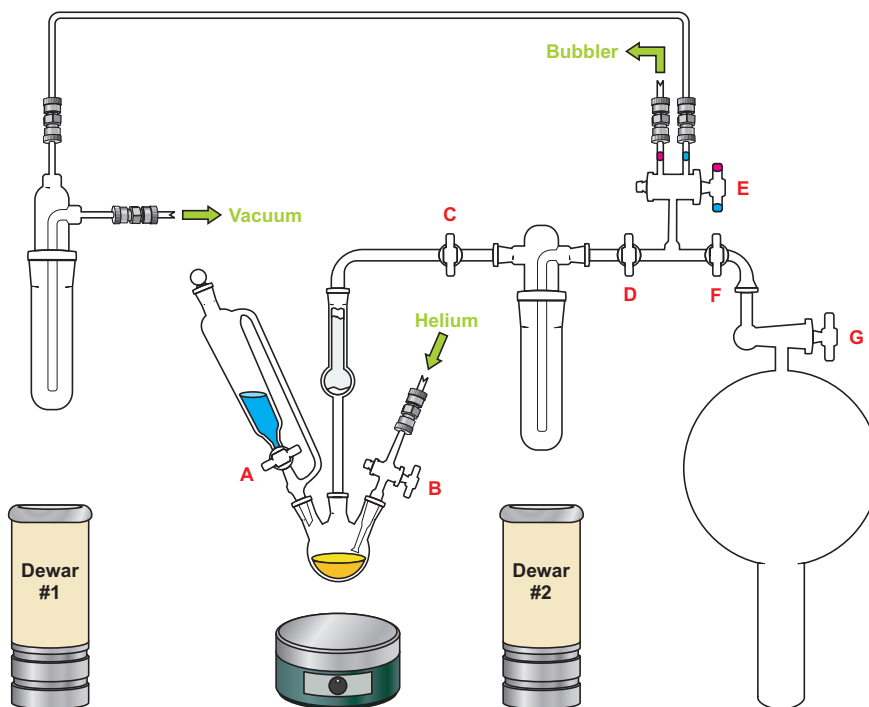


Figure 2.1 Diagram of apparatus used in the synthesis of HCN. The stopcocks, labelled A through G, were used to: introduce H_2SO_4 (aq) to KCN (aq) in the round bottom flask (A), control the flow rate of helium gas (B), isolate evolved HCN (C, D, E and F), and toggle between vacuum system and mineral oil bubbler (E). The cold traps, located directly above Dewar flasks #1 and #2, were used to condense any evolved HCN gas.

After sufficient pumping, the contents of the sample cold trap were expanded into an evacuated 3 L glass bulb for storage. The large volume and the high vapour pressure of HCN (0.88 bar at ~ 22 °C [69]) prevented any liquid hydrogen cyanide from forming or any HCN gas leaking out. As mentioned above, the former case is a serious concern as liquid HCN can polymerize

explosively. The outlined procedure provides nearly pure HCN gas with water being the only detectable impurity. The extent of H₂O contamination is assessed by monitoring the $J = 2-1$ transition of the HCN–H₂O dimer [71].

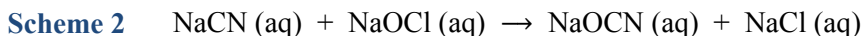
c) Isotopologues

The carbon-13 and nitrogen-15 containing isotopologues of HCN were synthesized by using isotopically enriched potassium cyanide, K¹³CN (Isotec Inc., 99.1 atom % ¹³C) and KC¹⁵N (Isotec Inc., 99.4 atom % ¹⁵N), respectively. The deuterated isotopologue was initially synthesized using sulfuric acid-d₂ solution in D₂O (Sigma Aldrich, purity 96-98 wt. % with 99.5 atom % D); however, it was discovered that the D¹³CN isotopologues could be generated by conditioning the gas-handling system of the instrument with D₂O, as a result of H/D exchange between H¹³CN and the surface bound D₂O.

d) Disposal

Given the high acute toxicity of cyanides and the hazards they pose to the environment, containment and proper disposal of HCN and KCN were serious concerns. To reduce the release of HCN to the environment, all excess gas samples were first fed through a bubbler containing a 10% w/w NaOH solution before being vented into the fume hood. The contents of the RBF in Figure 2.1, likewise, had to be neutralized with NaOH (aq) after each reaction.

The pH values of both mixtures were required to be ≥ 10 before proceeding with the oxidation of cyanide (Scheme 2) [64]. This involved cooling the alkali solutions, with a salt-ice-water bath, to 4–10 °C and slowly adding 1.5 equivalents of household bleach (containing at least 0.75 M sodium hypochlorite). This mixture was typically left to stand overnight before being poured down the drain with excess water. Note that the cyanate produced in this reaction is harmless to the environment and essentially nontoxic to organisms.



e) Alternate synthesis

Another common procedure for producing HCN gas involves heating equal molar amounts of dry stearic acid and potassium cyanide *in vacuo* to 350 K (refer to Scheme 3) [72-74]. The subsequent collection process follows the same procedure outlined above. In fact, this method can easily be implemented using the same apparatus represented by Figure 2.1 and is advantageous in its simplicity, easy cleanup, and high yield. However, common impurities encountered include H₂O [74] and CO₂ [72, 73], which still persist even after purification.



2.1.2 Generation of Clusters

a) Sample concentrations

In order to form He_N-HCN clusters, hydrogen cyanide had to be transferred to a stainless-steel gas cylinder and then diluted with helium. In previous studies, the typical sample concentrations were on the order of ~0.1% [31, 33, 35, 40, 41, 48, 50, 53, 75]. However, preliminary experiments with He_N-HCN clusters indicated that this concentration was still too high and led to the formation of aggregates of HCN—this was confirmed by measuring the $J = 3-2$ transition of the HCN-HCN dimer [76]. Instead, concentrations of ~20–75 ppm (or 0.0025–0.0050%) were needed to generate clusters with relatively high backing pressures of 40–100 bar helium.

b) Supersonic jet-expansion

The main components required for a *supersonic* jet-expansion, produced in a pulsed molecular beam experiment, include: a gas reservoir, a valve, and an evacuated sample cell. The gas reservoir, in this case, is the sample mixture mentioned in the preceding section with a stagnation pressure between 40 and 100 bar and a temperature of $T_0 \sim 300$ K; while the valve used in these experiments

was actually a pulsed nozzle (General Valve Series 9) with an orifice diameter of 0.8 mm.

Prior to an experiment, the atoms and molecules in the reservoir possess a range of random atomic and molecular motion with zero net velocity. Since the concentration of HCN is on the order of 10 ppm, the expansion properties of the sample can be safely assumed to be dictated by the carrier gas helium [77, 78]. Consequently, the range of atomic velocities is described by a Maxwell distribution, with the most probable speed of [79]:

$$v^* = \sqrt{\frac{2k_B T_0}{m}}. \quad 2.1$$

Equation 2.1 represents the velocity of the Maxwell distribution peak, where k_B is the Boltzmann constant and m represents the mass of a single carrier gas atom, e.g., ^4He .

When the nozzle is opened (typically only for 500–800 μs), the random kinetic energy of the reservoir gas is transformed into directed forward motion through binary collisions [77, 80]. The valve is opened only briefly to ensure that the vacuum pump is not overloaded [77]. As the gas expands into the evacuated sample cell, v^* decreases, the Maxwell velocity distribution narrows and in turn the translational temperature of gas decreases rapidly.

The internal degrees of freedom of the seed molecule—i.e., the rotational and vibrational energies of HCN—relax through collisional cooling with the *cold* gas atoms [80]. However, during the expansion the density of particles decreases with increasing distance from the nozzle and so does, therefore, the number of collisions. As a result of this, equilibrium is not fully achieved between the translational, rotational and vibrational modes. As such, typical translational, rotational and vibrational temperatures in a supersonic jet-expansion are $T_{tr} = 0.1\text{--}1$ K, $T_{rot} = 0.1\text{--}1$ K, and $T_{vib} \gtrsim 50$ K, respectively [78, 81].

Analysis of the Doppler splitting of transition lines by Campbell *et al.* [82], revealed that the velocity of the dopant molecules is equal to the carrier gas speed. If the internal energy of the dopant was completely converted into the

translational energy of the directed flow, then the terminal velocity of the expansion would be [77]

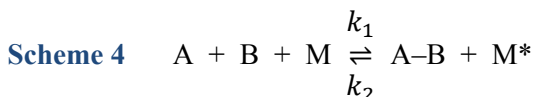
$$v_T = \sqrt{\frac{2\gamma}{\gamma-1} \frac{k_B T_0}{m}}, \quad 2.2$$

with the heat capacity ratio $\gamma = C_P/C_V = 5/3$ for rare gases. Using Equation 2.2, the terminal velocity of helium atoms and HCN molecules in a supersonic expansion is 1.77×10^3 m/s. However, the term “supersonic” refers to the Mach number, M , of the expansion and is defined as the ratio of the gas velocity to the speed of sound in the medium. As the temperature drops, the local speed of sound decreases and, thus, M increases rapidly. The Mach number for supersonic jet-expansions can reach $M > 50$ [80].

c) Complex Formation

The formation of clusters in supersonic jet-expansion proceeds through three-body kinetics [77], following Scheme 4, which dominates within 4 mm (or 5 orifice diameters) from the nozzle [80]. The third body, $M \equiv {}^4\text{He}$, is required to remove the excess kinetic energy. Given the extent of dilution, the species A and B correspond to ${}^4\text{He}$ and HCN, respectively. The rate constants, k_1 and k_2 , are dependent on the three- and two-body collision frequencies [77].

Once formed, the weakly bound ${}^4\text{He}_N\text{-HCN}$ clusters persist due to the low translational temperatures of the jet-expansion. The rapid drop in number density (a 500-fold decrease in the first 8 mm [80]), creates a collisionless environment for the clusters to exist in isolation until they reach the opposite wall of the sample cell.



2.2 Microwave Spectroscopy

Microwave radiation spans the electromagnetic spectrum from approximately 1 to 10^{-4} meters (0.3 to 3000 GHz; 0.01 to 100 cm^{-1}) and predominantly interacts with matter by driving transitions between molecular rotational quantum states as is done in rotational spectroscopy. Microwave radiation is also used in electron paramagnetic resonance (EPR) and even in electronic spectroscopy (between near-degenerate electronic states), while, in a few exceptional cases, infrared light can rotationally excite low mass molecules, such as hydrogen chloride. Although EPR does fall under the umbrella of “microwave spectroscopy”, microwave spectra owe their vast richness to the plethora of rotational energies that lie in the microwave region.

2.2.1 Theory

a) Rigid rotor

The derivation of rotational energy levels of a polyatomic system is best introduced through the “rigid rotor” model [83-85] which considers the end-over-end rotation of two point masses about their center of mass (c.o.m.) and separated by a fixed distance—as in a rotating diatomic molecule with a rigid bond. To obtain the eigenfunctions which describe the *stationary states* of an isolated rigid rotor, the time-independent Schrödinger equation can be used (Equation 2.3) with the energy operator \hat{H}_0 written in spherical coordinates for convenience, see Equation 2.4 [85]:

$$\hat{H}_0\psi(q) = E\psi(q), \tag{2.3}$$

$$-\frac{\hbar^2}{2I} \left[\frac{1}{\sin\theta} \frac{\partial}{\partial\theta} \left(\sin\theta \frac{\partial}{\partial\theta} \right) + \frac{1}{\sin^2\theta} \left(\frac{\partial^2}{\partial\phi^2} \right) \right] \psi(\theta, \phi) = E\psi(\theta, \phi), \tag{2.4}$$

$$\hat{I}_g = \sum m_i r_i^2(g). \tag{2.5}$$

Where \hat{I}_g is the moment of inertia, a measure of a body's resistance to rotation; m_i is the mass of the i^{th} particle and $r_i(q)$ is its distance to the c.o.m. perpendicular to the g -axis. The set of eigenfunctions, $\psi(\theta, \phi)$, that satisfy Equation 2.4 and the rigid rotor model are the spherical harmonics, $Y_J^m(\theta, \phi)$, defined by:

$$Y_J^m(\theta, \phi) = i^{m+|m|} \left[\frac{(2J+1)}{4\pi} \frac{(J-|m|)!}{(J+|m|)!} \right]^{1/2} P_J^{|m|}(\cos \theta) e^{im\phi}, \quad 2.6$$

$$J = 0, 1, 2, \dots,$$

$$m = 0, \pm 1, \dots, \pm J;$$

where $P_J^{|m|}$ are the associated Legendre functions. The above spherical harmonic wavefunctions yield the following energies,

$$E_J^{rr} = \frac{\hbar^2}{2I} J(J+1) = BJ(J+1). \quad 2.7$$

These E_J^{rr} are the energies of the discrete, quantized rotational states of the rigid rotor. In Equations 2.6 and 2.7, the variables J and m (or M_J) are the rotational and magnetic quantum numbers, respectively, that define rotational quantum states, while B is the rotational constant (in Joules) and is inversely proportional to the moment of inertia—thus, it is a measure of the ease at which a molecular system rotates. Note that the magnetic quantum number m does not influence the energy of an isolated rigid rotor (Equation 2.7), and, consequently, each rotational state is $(2J+1)$ -fold degenerate. This degeneracy can be fully (or partially) removed in the presence of an external magnetic or electric field in what is known as the Zeeman or Stark effects, respectively.

b) Transition dipole moment

The energies of these rotational states can be determined by probing the system with light (nearly) matching the energy difference between states. The strength of the interaction between a rotor and radiation depends on the transition dipole moment:

$$\overrightarrow{\mu}_{g_{f \leftarrow i}} = \langle \psi_f | \overrightarrow{\mu}_g | \psi_i \rangle = \int \psi_f^* \overrightarrow{\mu}_g \psi_i \partial \tau. \quad 2.8$$

Here, $\overrightarrow{\mu}_g$ is the projection of the electric dipole operator along the g -axis (where g can be replaced by the Cartesian coordinate axes x , y , and z). Equation 2.8 states that in order for any type of rotor to interact with radiation, it must possess a permanent electric dipole moment and that the projection of this dipole moment, along the axis of the electric field, must be nonzero. This is the “handle” at which the radiation grabs onto the rotor and applies a torque—the larger the handle, the greater the interaction. Another requirement is based on the orthogonality of the initial and final states’ wavefunctions, ψ_i and ψ_f , and limits the number of allowed transitions to those that result in $\Delta J = \pm 1$, i.e., between adjacent levels.

c) Semi-rigid linear rotor

Despite being a reasonable approximation, the rigid rotor model tends to overestimate rotational energies of even simple diatomic molecules. This is due to the bond stretching under centrifugal distortion and can become quite significant for weakly bound systems like van der Waals complexes [86-91]. The spectra become even more complicated for polyatomic molecules.

In microwave spectroscopy, molecules are classified into five categories based on their principle moments of inertia: linear molecules ($\hat{I}_a = 0$, $\hat{I}_b = \hat{I}_c$), spherical-tops ($\hat{I}_a = \hat{I}_b = \hat{I}_c$), prolate symmetric-tops ($\hat{I}_a < \hat{I}_b = \hat{I}_c$), oblate symmetric-tops ($\hat{I}_a = \hat{I}_b < \hat{I}_c$), and asymmetric-tops ($\hat{I}_a < \hat{I}_b < \hat{I}_c$). Since HCN is linear and the spectra of $\text{He}_N\text{-HCN}$ clusters resemble that of a linear system, I will forgo any discussion on the nonlinear categories; however, References [83] and [84] provide rigorous and comprehensive description for each of the above classifications.

The energies and transition frequencies for a semi-rigid linear rotor are given below. As can be seen from Equation 2.9, the energies differ from those of the rigid rotor by the inclusion of centrifugal distortion constants: D , H , and even higher order distortion terms when applicable. Dropping the higher order terms

and abiding by the selection rules governed by Equation 2.8, the transition frequencies of a linear rotor are conveniently given by Equation 2.10. (Note: to differentiate between units, constants unaccented are typically in energy units, unless otherwise stated, while those with a tilde accent are in frequency units.)

$$E_J = BJ(J + 1) - DJ^2(J + 1)^2 + HJ^3(J + 1)^3 + \dots \quad 2.9$$

$$\nu_{J+1 \leftarrow J} = 2\tilde{B}(J + 1) - 4\tilde{D}(J + 1)^3 \quad 2.10$$

d) Population of states

At any temperature above absolute zero, a whole range of possible energy levels can be *occupied*. If an ensemble of molecules is in thermal equilibrium the number of molecules occupying the i^{th} quantum state, N_i , can be determined via the Boltzmann distribution [79]:

$$N_i = \frac{g_i N}{q} e^{-E_i/k_B T}, \quad 2.11$$

$$q = \sum_i g_i e^{-E_i/k_B T}. \quad 2.12$$

The terms q and g_i , in Equations 2.11 and 2.12, represent the molecular partition function and the number of states with energy E_i , respectively.

Equation 2.11 can be used to determine the relative populations, N_J/N_{J+1} , and most occupied rotational level, J^* , for a rigid rotor:

$$N_J/N_{J+1} = \frac{2J+1}{2J+3} e^{2\hbar B(J+1)/k_B T}, \quad 2.13$$

$$J^* = \sqrt{\frac{k_B T}{2\hbar B}} - \frac{1}{2}. \quad 2.14$$

For a rigid rotor, with a rotational constant comparable to HCN, J^* reaches ~ 21 while $N_0/N_1 \sim 0.33$ for $T_0 \sim 300$ K. However, in the case of a rigid rotor in a supersonic jet-expansion (see §2.1.2 on page 18), where temperatures reach $T_{rot} \sim$

0.1 K, the most probable occupied state becomes $J = 0$ with $N_0/N_1 \sim 300$. As will be shown later (§2.3.1), this substantial population difference plays an important role in modern microwave spectroscopy.

e) Hyperfine structure

As mentioned above, applying an external magnetic or electric field to a rotor will split the rotational levels into m sublevels—where the degree of splitting is dependent on the field strength. However, the microwave spectra of certain rotors reveal small splitting patterns or shifts in energy levels, even in the absence of an external field (apart from the probe field). This “hyperfine structure” can be due to a wide range of interactions occurring within the molecule that may be electrostatic or magnetic in origin. If, for example, a molecule is in a $^1\Sigma$ state (typically the case for most molecules in their electronic ground state [84]), then the hyperfine splitting can occur through nuclear electric quadrupole coupling (an electrostatic interaction that requires a nucleus to have a nuclear spin $I > \frac{1}{2}$), through magnetic nuclear spin-molecular rotation interaction ($I > 0$), or through nuclear spin-nuclear spin interactions (for two or more nuclei with $I > 0$). On the other hand, if the molecule has at least one unpaired electron (i.e., is not in a $^1\Sigma$ state); then, in addition to the above interactions, the spin of the electron can couple with: the molecular rotation, the nuclear spin (for any nuclei with $I > 0$), or the spin of another unpaired electron to produce hyperfine splittings.

Only the first interaction mentioned above, nuclear electric quadrupole coupling, is relevant to HCN and $\text{He}_N\text{-HCN}$ clusters ($I = 1$ for ^{14}N) at the resolution and accuracy achieved in these studies. The origin of this interaction is in the nonspherical nuclear charge distribution (found in atomic nuclei with spins $I > \frac{1}{2}$) which leads to an electric quadrupole moment, Q . Generally speaking, in an inhomogeneous electric field, the energy of an electric quadrupole depends on its orientation and the electric field gradient, $q \equiv \frac{\partial^2 V}{\partial t^2}$ (where V is the electrostatic potential)—such as those generated by the valence electrons surrounding

molecular nuclei; this is the means by which the nuclear spin couples with the molecular rotation [92]. Changes to the quadrupole's orientation relative to the molecular axis can alter the total angular momentum and, thus, also the interaction energy. A new quantum number can be introduced to describe this coupling, the total angular momentum (including nuclear spin): $F = J + I, J + I - 1, \dots, |J - I|$ [83, 84].

The nuclear quadrupole interaction energy for a linear rotor is given by

$$E_Q = -eqQf(I, J, F) = -\chi_0 f(I, J, F). \quad 2.15$$

Where e is the electron charge, $\chi_0 \equiv eqQ$ is the nuclear quadrupole coupling constant, and $f(I, J, F)$ is Casimir's function which is defined as

$$f(I, J, F) = \frac{3/4C(C+1) - J(J+1)I(I+1)}{2(2J-1)(2J+3)I(2I-1)}, \quad 2.16$$

with $C = F(F + 1) - I(I + 1) - J(J + 1)$. For HCN, the $J = 1$ rotational state is split into 3 hyperfine levels (with $F = 2, 1$, and 0) and the ^{14}N nuclear quadrupole coupling constant, χ_0 , is $-4.70789(8)$ MHz [62]. Since the ground rotational state itself ($J = 0, F = 1$) is not split, the $J = 1-0$ transition reveals three hyperfine lines with relative intensities of 3:5:1 for the $F = 1-1, 2-1$, and $0-1$ transitions, respectively; whereas all higher order transitions are split into six lines with different relative intensities [83, 84].

This unique splitting pattern for $J = 1-0$ transitions served as an invaluable fingerprint for easy identification of $\text{He}_N\text{-HCN}$ clusters in the course of this study. Furthermore, in the case of weakly bound clusters, such as van der Waals complexes, the magnitude of the hyperfine splitting typically decreases upon complex formation and this change in the coupling constant is related to the structure of the complex [29, 93-96]. Therefore, the hyperfine structure of $\text{He}_N\text{-HCN}$ clusters could provide experimental evidence of solvation dynamics as a function of cluster size.

f) Kraitchman coordinates

Analysis of nuclear quadrupole hyperfine splitting is not the only method to investigate molecular structure. Owing to its high resolution, microwave spectroscopy allows for the determination of bond lengths, and angles to an extremely high degree of accuracy. One established method of investigating molecular structure from microwave spectra, developed by Kraitchman [97], involves comparing the moments of inertia (determined from the experimental rotational constants) of one molecular system with that of other, singly- or multiply-isotopically substituted ones.

By assuming that the substituted heavy atom lies along the symmetry axis of the cluster—a reasonable assumption given the fact that the rotational spectra of the $\text{He}_N\text{-HCN}$ clusters follow that of a linear system—the distance of the substituted atom from the cluster’s center of mass, measured along the symmetry z -axis (or the a -axis using the principle coordinate system), is given by

$$|z| = \sqrt{\mu^{-1}(\hat{I}'_X - \hat{I}_X)}, \quad 2.17$$

$$\mu = \frac{M \cdot \Delta m}{M + \Delta m}, \quad 2.18$$

where $\hat{I}'_X \equiv \hat{I}'_Y$ and $\hat{I}_X \equiv \hat{I}_Y$ are the moments of inertia of the substituted and original molecular species along either the principle b - or c -axes, respectively; M is the mass of the original species and Δm is the “mass change” upon isotopic substitution.

Solving Equation 2.17 yields the position of each nucleus within the molecular complex and can subsequently be used to determine bond lengths. In spite of the merits of this substitution analysis, Kraitchman acknowledged several important approximations that this procedure relies on. The most important assumption is that the equilibrium structures of a family of isotopologues are equivalent and, thus, the equilibrium rotational constants must be used. In the case when equilibrium values of B are not available, but instead the ground state constants are used, the resulting effective moments of inertia calculated are

averaged over the zero-point energy motion of the complex (or more specifically, r^2 of Equation 2.5 is averaged over this vibrational motion) and, as a result, the atomic coordinates will be in error by some amount [97].

2.2.2 *Transition Dynamics*

a) *Relevance*

The above theory gives a basic understanding of microwave spectroscopy in terms of line positions and splitting, but fails to explain the mechanism of spectroscopic transitions. Does a quantum system instantaneously jump to and from eigenstates or does its wavefunction constantly evolve during the transition? The answer to this seemingly philosophical question is typically overlooked during undergraduate physical chemistry courses. However, insight into the behaviour of quantum systems, from a single particle to an ensemble, and their response to an applied perturbation is necessary to understand which experimental parameters govern the transition dynamics and how they can be adjusted to optimize signal strength. Before jumping to specific applications in microwave spectroscopy, a brief overview of the underlying principles is required. The following is merely a summary of several important topics relevant to my discussion and are by no means comprehensive. For significantly more detailed explanations, the reader should consult References [98-103].

b) *Superposition states*

As mentioned above, the eigenstates of Equation 2.3 are often referred to as stationary states, so named because their probability densities, $\psi_i^*\psi_i$, are constant over time. However, these are not the only states the quantum system is allowed to exist in. In fact, any state represented by a linear combination of eigenstates is not only permissible but necessary for a transition to occur [98].

To illustrate this point, consider an isolated, nondegenerate, two-level quantum system existing in one of these *superposition states*,

$$\Psi_s(q, t) = c_1\Psi_1(q, t) + c_2\Psi_2(q, t); \quad 2.19$$

where $\Psi_i(q, t)$ represents the total wavefunction of the state (with both spatial, $\psi_i(q)$, and temporal, $e^{-iE_it/\hbar}$, dependencies); c_i are the probability amplitudes which, in the absence of radiation, are constant and can be thought of as the “amount” of Ψ_i contributing to the overall wavefunction. The absolute square of the probability amplitudes, $c_i^*c_i$, represents the likelihood of observing the system in eigenstate ψ_i and, therefore, the sum of $c_i^*c_i$ must equal unity [103].

$$\Psi_s^*\Psi_s = |\Psi_s|^2 = |c_1|^2|\Psi_1|^2 + |c_2|^2|\Psi_2|^2 + 2\text{Re}\{c_1^*c_2\Psi_1^*\Psi_2\} \quad 2.20$$

$$\Psi_1^*\Psi_2 = \psi_1^*(q)\psi_2(q)e^{-i\omega_{21}t} \quad 2.21$$

$$\omega_{21} = \frac{E_2 - E_1}{\hbar} \quad 2.22$$

The probability density of the above superposition state is given by Equation 2.20. It can be seen from Equation 2.21 that $\Psi_s^*\Psi_s$ has an explicit, undulating time dependency and, furthermore, it must oscillate at a frequency ω_{21} proportional to the energy difference of eigenstates Ψ_1 and Ψ_2 (see Equation 2.22).

To illustrate this point, Figure 2.2 contains several snapshots of $\Psi_s^*\Psi_s$ for a rigid rotor with $|c_1|^2$ equal to 0.98, 0.75, 0.50, 0.25, and 0.02. Each of these $\Psi_s^*\Psi_s$ distributions oscillate at the same frequency, ω_{21} , and shown in Figure 2.2 is half a period. By comparing the first row to the last, it is clear that the greatest change in amplitude occurs when $|c_1|^2 = |c_2|^2 = 0.50$. Now, if these rigid rotors possess a permanent electric dipole, then Figure 2.2 actually depicts several oscillating dipoles that can interact with an applied electromagnetic field. In fact, $\Psi_s^*\Psi_s$ is the physical representation of the transition dipole moment defined in Equation 2.8. More importantly, since accelerating charges emit radiation, a quantum particle in a superposition state is, in a classical picture, a nanoscale antenna

broadcasting at a steady frequency ω_{21} . The intensity of the emitted light would be greatest for the particle in the superposition state with $|c_1|^2 = |c_2|^2$.

c) Rabi frequency and detuning

In the presence of light the behaviour of $\Psi_s^* \Psi_s$ becomes slightly more complicated as the probability amplitudes are no longer independent of time. Instead, c_i are very much dependent on the polarization of light and its pulse shape; phase, ϕ ; electric field strength, \mathcal{E}_0 ; and its frequency, ω —some of which may or may not vary with time. A linearly polarized light, for example, can be described by Equation 2.23; with the wavevector, \vec{k} , containing information about the wavelength of light and the direction of propagation (see Equation 2.24).

$$\vec{\mathcal{E}}(t) = \mathcal{E}_0 \cos(\vec{k}z - \omega t + \phi) \quad 2.23$$

$$|\vec{k}| \equiv k = \frac{2\pi}{\lambda} \quad 2.24$$

Continuing with this example, the probability density for a quantum particle interacting with a linearly polarized pulse is described by two coupled linear differential equations (see Equations 2.25a-b) [103]. The evolution of the probability densities over time are completely dependent on just two parameters: the *Rabi frequency*, $\Omega(t)$, and the *detuning*, $\Delta(t)$ —both of which may have either an explicit time dependence or not.

$$\left. \begin{aligned} \dot{c}_1(t) &= -\frac{i}{2}\Omega(t)e^{i\phi}c_2(t) \\ \dot{c}_2(t) &= -\frac{i}{2}\Omega(t)e^{i\phi}c_1(t) - i\Delta(t)c_2(t) \end{aligned} \right\} \quad 2.25\text{a-b}$$

$$\Omega(t) = \frac{\vec{\mu}_{q \leftarrow i} \cdot \vec{\mathcal{E}}(t)}{\hbar} \quad 2.26$$

$$\Delta(t) = \omega(t) - \omega_{21} = \Delta_0 + \alpha t \quad 2.27$$

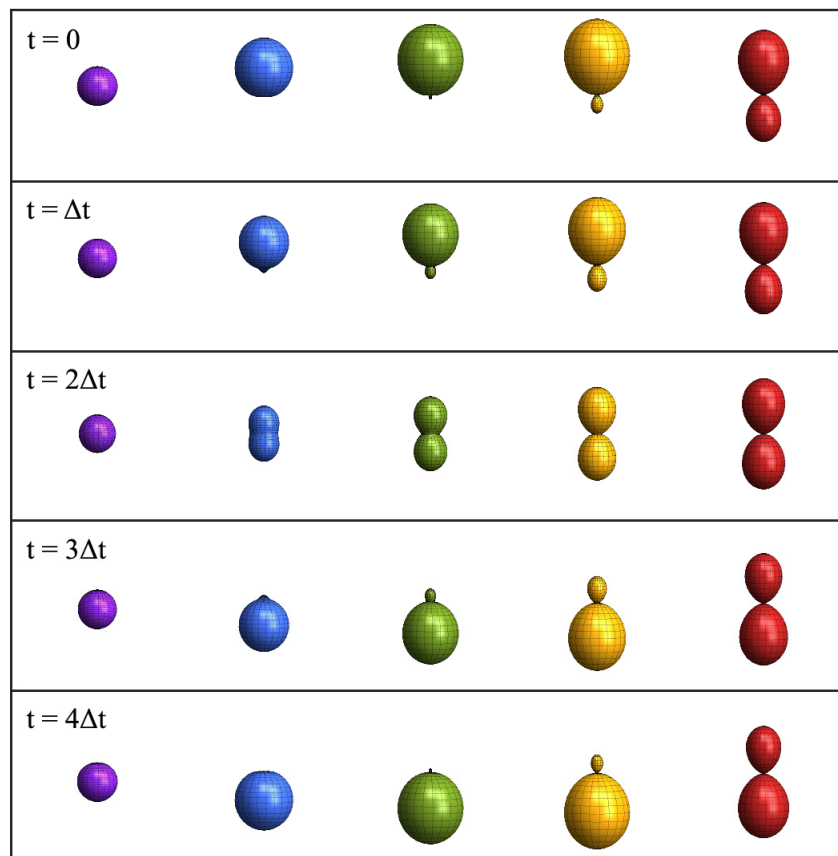


Figure 2.2 A comparison of various superposition states composed of the $J = 0$ and $J = 1$ stationary states of a rigid rotor. A series of snapshots of one half-cycle of the oscillating probability density of Ψ_s described by Equation 2.19 with $|c_1|^2$ equal to 0.98 (purple), 0.75 (blue), 0.50 (green), 0.25 (yellow), and 0.02 (red). The time step between each successive row is $\Delta t = 1/8\omega_{21}$.

As seen in Equation 2.26, the Rabi frequency is a measure of the strength of interaction between the quantum system and the electric field of the light, $\vec{\mathcal{E}}(t)$. Furthermore, since the probability amplitude explicitly depends on $\Omega(t)$, the Rabi frequency is sometimes referred to as the *flip-flop* frequency and is the rate at which the superposition state evolves from Ψ_1 , through Ψ_2 , and then back to Ψ_1 . The detuning is simply the difference between the frequency of light, $\omega(t)$, and

the transition frequency, ω_{21} , and can be set to a constant value, Δ_0 , or vary linearly with a sweep rate α .

A few important notes on Equations 2.25a-b need to be made. First, several approximations were made in the derivation of these coupled differential equations. These include transforming to a rotating frame and invoking the rotating wave approximation (RWA) and neglecting the nonresonant, high frequency terms. Second, these approximations are valid when the detuning is negligible relative to $\omega(t)$ and ω_{21} —the *near resonance* condition—and, furthermore, the Rabi frequency is significantly lower than $\omega(t)$ —the *weak field* condition.

The difficulty in dealing with these coupled differential equations is that they typically can only be solved analytically for a few specific cases, such as on resonance ($\Delta = 0$) and constant electric field ($\dot{\Omega} = 0$), whereas, under different circumstances, one must rely on numerical integration methods. In either way, these equations describe the evolution of the state of a quantum system as it is perturbed by a classical pulse of radiation and are vital in understanding the generation of superposition states.

d) Ensemble average and density matrix

The theory above dealt with a single quantum particle, which is quite useful and necessary, but most spectroscopists typically do not study a single particle. Instead, there is a myriad of particles—say, in a molecular beam experiment—each prepared in a slightly different way. A few examples include different orientations, velocities, quantum states, and local environments. Therefore, what is observed during an experiment is an ensemble average, or expectation value, of some property of the bulk system.

Consider an ensemble of N two-level quantum particles each potentially existing in a unique state, as described below by Equation 2.28 (for the sake of brevity, the spatial and temporal dependencies are implied):

$$\Psi_N = c_{1,N}\psi_1 e^{-iE_1 t/\hbar} + c_{2,N}\psi_2 e^{-iE_2 t/\hbar} = a_{1,N}\psi_1 + a_{2,N}\psi_2. \quad 2.28$$

(Note that $a_{i,N}$ is the collection of all time-dependent factors.) To understand the behaviour of the ensemble in response to an electromagnetic field, the average transition dipole moment, $\langle \vec{\mu} \rangle$, must be determined—and with limited information of the system. This is achieved by taking the resulting trace of the density matrix and transition dipole matrix dot product [98-103], i.e.,

$$\langle \vec{\mu} \rangle = \frac{1}{N} \sum_{i=1}^N \vec{\mu}_i = \text{Tr} \{ \underline{\rho} \cdot \underline{\mu} \}. \quad 2.29$$

Where the density matrix, $\underline{\rho}$, carries all the time-dependent information of the ensemble (Equation 2.30) and $\underline{\mu}$ is merely the matrix representation of the transition dipole moments for the system (Equation 2.31).

$$\underline{\rho} = \begin{bmatrix} \rho_{11} & \rho_{12} \\ \rho_{21} & \rho_{22} \end{bmatrix} = \begin{bmatrix} \frac{1}{N} \sum_{i=1}^N a_{1,i} a_{1,i}^* & \frac{1}{N} \sum_{i=1}^N a_{1,i} a_{2,i}^* \\ \frac{1}{N} \sum_{i=1}^N a_{2,i} a_{1,i}^* & \frac{1}{N} \sum_{i=1}^N a_{2,i} a_{2,i}^* \end{bmatrix} \quad 2.30$$

$$\underline{\mu} = \begin{bmatrix} 0 & \vec{\mu}_{2 \leftarrow 1} \\ \vec{\mu}_{1 \leftarrow 2} & 0 \end{bmatrix} \quad 2.31$$

As seen in Equation 2.30, the diagonal elements of the density matrix, i.e., ρ_{ii} , are the *populations* of state Ψ_i ; while the off-diagonal elements, ρ_{ij} , are referred to as the *coherences* and describe the phase relation between the two eigenstates.

Determining the average transition dipole moment, $\langle \vec{\mu} \rangle$, can be taken one step forward by calculating the net induced dipole moment, otherwise known as the *macroscopic polarization*, \vec{P} . This is possibly the most important parameter to an experimentalist as the signal strength is completely dependent on the magnitude of \vec{P} . As is made evident by Equation 2.32 below, the polarization is greatest at maximum coherence of the ensemble. This is not surprising, as the

strength of a signal emitted by a myriad of nanoscale antennas is greatest when they are broadcasting in unison.

$$\vec{P} = N\langle\vec{\mu}\rangle = N \vec{\mu}_{2\leftarrow 1}(\rho_{12} + \rho_{21}) \quad 2.32$$

e) *Optical Bloch equations*

To understand how coherence is generated, the time-dependent Schrödinger equation must be solved, for example, in the density matrix formalism:

$$i\hbar \frac{\partial \underline{\rho}}{\partial t} = [\underline{\hat{H}}, \underline{\rho}] = \underline{\hat{H}}\underline{\rho} - \underline{\rho}\underline{\hat{H}}. \quad 2.33$$

Where $\underline{\hat{H}}$ is the matrix representation of the Hamiltonian operator and is comprised of two parts: $\underline{\hat{H}}_0$, the time-independent Hamiltonian (equivalent to the energy operator in Equations 2.3 and 2.4); and $\underline{\hat{H}}_1$, which describes the time-dependent perturbation caused by an external oscillating electromagnetic field (see Equation 2.35).

$$\underline{\hat{H}} = \underline{\hat{H}}_0 + \underline{\hat{H}}_1 \quad 2.34$$

$$\underline{\hat{H}}_1 = -\underline{\mu} \vec{\mathcal{E}}(t) = -\underline{\mu} \varepsilon_0 \cos(\vec{k}z - \omega t + \phi) \quad 2.35$$

The elements of $\underline{\rho}$ can be solved through expansion of Equation 2.33. By switching the coordinates of ρ_{ii} and ρ_{ij} to a rotating reference frame and applying the RWA, the following coupled first-order differential equations can be derived [99]:

$$\left. \begin{aligned} \dot{u}(t) &= \Delta(t) \cdot v(t), \\ \dot{v}(t) &= -\Delta(t) \cdot u(t) - \Omega(t) \cdot w(t), \\ \dot{w}(t) &= \Omega(t) \cdot v(t). \end{aligned} \right\} \quad 2.36a-c$$

These variables are the optical analogs of the Bloch equations of nuclear magnetic resonance (NMR) [104] and provide a description of the interaction of an ensemble of two-level quantum particles with a classical electric field (so long as the near resonance and weak field conditions are met). The variables $u(t)$ and $v(t)$ represent the coherence of the ensemble, while $w(t)$ is the population difference between eigenstates ψ_1 and ψ_2 . Despite the simplicity of Equations 2.36a-c, analytical solutions are only possible for a few specific cases and, even still, approximations must be made.

The Bloch variables can also be used to redefine the macroscopic polarization originally given by Equation 2.32. By compensating for the rotating reference frame and change of variables, the polarization is described by

$$\vec{P} = N \vec{\mu}_{2\leftarrow 1} [u(t) \cdot \cos(\omega t) + v(t) \cdot \sin(\omega t)]. \quad 2.37$$

To help visualize the dynamics of the ensemble, the Feynman-Vernon-Hellwarth (FVH) representation [105] of Equations 2.36a-c is required. In essence, the variables $u(t)$, $v(t)$, and $w(t)$ represent the procession of the *Bloch vector*, $\vec{\Theta}(t)$, acted on by a torque $\vec{Y}(t)$ as described by Equations 2.38 to 2.40 [102, 103]. The Bloch and torque vectors exist in a three-dimensional space defined by the coordinate axes u , v , and w .

$$\frac{d}{dt} \vec{\Theta}(t) = \vec{Y}(t) \times \vec{\Theta}(t), \quad 2.38$$

$$\vec{Y}(t) \equiv \begin{pmatrix} \Omega(t) \\ 0 \\ -\Delta(t) \end{pmatrix}, \quad 2.39$$

$$\vec{\Theta}(t) \equiv \begin{pmatrix} u(t) \\ v(t) \\ w(t) \end{pmatrix}. \quad 2.40$$

In this ideal example, the length of $\vec{\theta}(t)$ is equivalent to the initial population difference, w_0 , and thus traces a path along a sphere of radius w_0 . When the Bloch vector lies in the uv -plane there is maximum coherence and, as a result, maximum polarization of the ensemble. Since the only adjustable parameters available to the experimentalist, once the ensemble is created, are those pertaining to the radiation (i.e., frequency, amplitude, polarization, pulse shape and length, etc.); it is, therefore, crucial to understand the effects of each parameter on the coherence of the sample in order to exploit the potential of any given spectroscopic method.

f) Relaxation processes

Up to this point, the above theory has intentionally avoided the inclusion of relaxation terms. This omission is valid so long as the time period of the perturbation is much shorter than the time of the relaxation processes, which can be described by relaxation parameters T_1 and T_2 . The former decay time, T_1 , relates the relaxation of the generated population difference to the Boltzmann equilibrium value, $w_{eq} \equiv w_0$ [99, 101, 106], while the latter decay time, T_2 , is related to the loss of the coherence of the ensemble. Both T_1 and T_2 can be phenomenologically included the optical Bloch equations by rewriting Equations 2.36a-c as:

$$\left. \begin{aligned} \dot{u}(t) &= \Delta(t) \cdot v(t) - \frac{u(t)}{T_2} , \\ \dot{v}(t) &= -\Delta(t) \cdot u(t) - \Omega(t) \cdot w(t) - \frac{v(t)}{T_2} , \\ \dot{w}(t) &= \Omega(t) \cdot v(t) - \frac{w(t) - w_{eq}}{T_1} . \end{aligned} \right\} \quad 2.41a-c$$

Subsequently, the FVH representation of the Bloch vector can be described by [102]:

$$\frac{d}{dt} \vec{\theta}(t) = \vec{Y}(t) \times \vec{\theta}(t) - \underline{\Gamma} \cdot [\vec{\theta}(t) - \vec{\theta}_{eq}], \quad 2.42$$

$$\underline{\Gamma} \equiv \begin{pmatrix} \frac{1}{T_2} & 0 & 0 \\ 0 & \frac{1}{T_2} & 0 \\ 0 & 0 & \frac{1}{T_1} \end{pmatrix}, \quad 2.43$$

$$\bar{\theta}_{eq} \equiv \begin{pmatrix} 0 \\ 0 \\ w_{eq} \end{pmatrix}. \quad 2.44$$

2.3 Balle-Flygare Cavity Fourier-Transform Microwave Spectrometer

The pursuit for greater sensitivity and resolution in microwave experiments, necessary to measure the rotational spectra of ions and transient species, led to the development of the Fourier-transform microwave (FTMW) spectrometer by Ekkers and Flygare [107]. This instrument relies on an intense microwave pulse, of frequency ω and of length τ , to generate a macroscopic polarization of a gas sample contained in an absorption cell. That is to say, if ω is resonant or near resonant with a molecular transition of the sample and, additionally, if τ is short relative to any relaxation process. Once the incident pulse has dissipated, the induced polarization then decays at a rate governed by T_2 while emitting radiation at the characteristic molecular transition frequency. It is this time domain signal that is detected, phase-coherently averaged with subsequent emission signals, and converted to the frequency domain via a Fourier-transformation.

As is the case in Fourier-transform NMR spectroscopy [108], FTMW spectroscopy in its most basic application is concerned with the response of an ensemble of two-level quantum particles cast in an electromagnetic field that is suddenly brought into or out of molecular resonance such that $\tau \ll T_1, T_2$. These short-lived responses are termed *transient phenomena* and are described by the optical Bloch equations (Equations 2.41a-c) [109]. When the system is quickly brought into resonance, *transient absorption* (or *transient nutation* in NMR) occurs. On the other hand, when the system is taken out of resonance abruptly, *transient emission* (or *free-induction-decay* in NMR) is observed.

To allow the study of dimers and van der Waals complexes, Balle and Flygare replaced the gas cell of the FTMW spectrometer with an evacuated cavity, containing a Fabry-Pérot resonator, and instead introduced the sample as a supersonic beam generated by a pulsed nozzle [77]. This new spectrometer, herein referred to as a Balle-Flygare FTMW spectrometer, allows for even greater signal-to-noise ratio (S/N), increased resolution, the generation of clusters of

various sizes and constituents, and the formation of molecular systems with very low translational, rotational and even vibrational temperatures. A brief description of the Balle-Flygare FTMW spectrometer used in the Jäger group is provided below. A more detailed description of the experimental design and theoretical considerations are given in References [102], [77] and [78].

2.3.1 *Theoretical Description*

a) *Single rigid rotor*

Despite knowledge on the behaviour of a single quantum particle in an external electromagnetic field being important, its significance is limited in experiments considering an ensemble of N quantum particles. Since the density matrix explicitly contains this behaviour (see Equations 2.30 and 2.28), as do the optical Bloch equations, a detailed description for a single rigid rotor will be skipped. Suffice to say, the emission signal detected in these FTMW experiments result from the oscillating probability density of a superposition state, Equation 2.20, and the signal is the largest when $|c_1|^2 = |c_2|^2 = 0.50$.

b) *Transient absorption*

In order to generate maximum polarization, the molecular ensemble must first absorb energy from the microwave radiation to convert its initial Boltzmann equilibrium population difference (§2.2.1(d) on page 24), w_{eq} , to maximum coherence—this is achieved through transient absorption. This behaviour can be modeled using the optical Bloch equations which can be solved analytically under the following assumptions: $\tau \ll T_1, T_2$ such that all relaxation process can be neglected; the near resonance and weak field conditions are satisfied such that $\Omega(t) \gg \Delta(t)$ (i.e., a *strong pulse*); both the Rabi frequency and the detuning are constant during τ ; and initially the system has zero coherence and a population difference of w_{eq} . Under these circumstances the Bloch variables that describe transient absorption in a FTMW spectrometer are:

$$\left. \begin{aligned} u(t) &= 0, \\ v(t) &= -w_{eq} \sin(\Omega t), \\ w(t) &= w_{eq} \cos(\Omega t). \end{aligned} \right\} \quad 2.45a-c$$

It is clear by inspection of Equations 2.45a-c that the coherence of the ensemble is at its greatest when $\Omega\tau = \pi/2$ (or any half-integer π value) and is nonexistent when $\Omega\tau = \pi$ (or any integer π value). The length of a *pi-half pulse* is dependent on the transition dipole moment and the field strength of the external radiation.

To better understand this phenomenon, consider an ensemble of HCN molecules, predominantly residing in their ground rotational states, suddenly stimulated by a strong microwave pulse inside a Fabry-Pérot resonator. For the sake of simplicity, if HCN is considered a rigid rotor, then the transition dipole moment for $J = 1 \leftarrow 0$ becomes $\overline{\mu}_{z_{1 \leftarrow 0}} = 1.72$ D. Assuming the field strength inside the resonator is roughly 180 V/m and homogeneous, then the corresponding Rabi frequency is given by 9.8×10^6 rad/sec (or 1.56 MHz). Therefore, the necessary pi-half pulse to achieve maximum coherence would be $\tau_{\pi/2} = 160$ ns long. Note that the actual length of $\tau_{\pi/2}$ depends on the system being studied, the specific transition, and the electric field strength.

Figure 2.3 depicts the evolution of each Bloch variable, for the above example, during a 2 μ s microwave pulse. The pi-half pulse, population inversion and population return (also known as a *Rabi cycle*) are clearly seen at time multiples of 160 ns, when the microwave pulse is on resonance with the rotational transition. It is worth pointing out that maximum coherence can still be achieved if the frequency of the radiation is near, but not equal to, the resonance frequency—i.e., when $|\Delta(t)| \leq \Omega(t)$. Under such circumstances, the ensemble's rate of oscillation from w_{eq} , to some nonequilibrium value, back to w_{eq} is no longer described by $\Omega(t)$ but instead by $Y(t)$, the *generalized Rabi frequency*. (Note that $Y(t)$ is also the length of the torque vector $\vec{Y}(t)$ as seen in Equation 2.39.) The coherence is then maximized at some fraction of the generalized Rabi cycle.

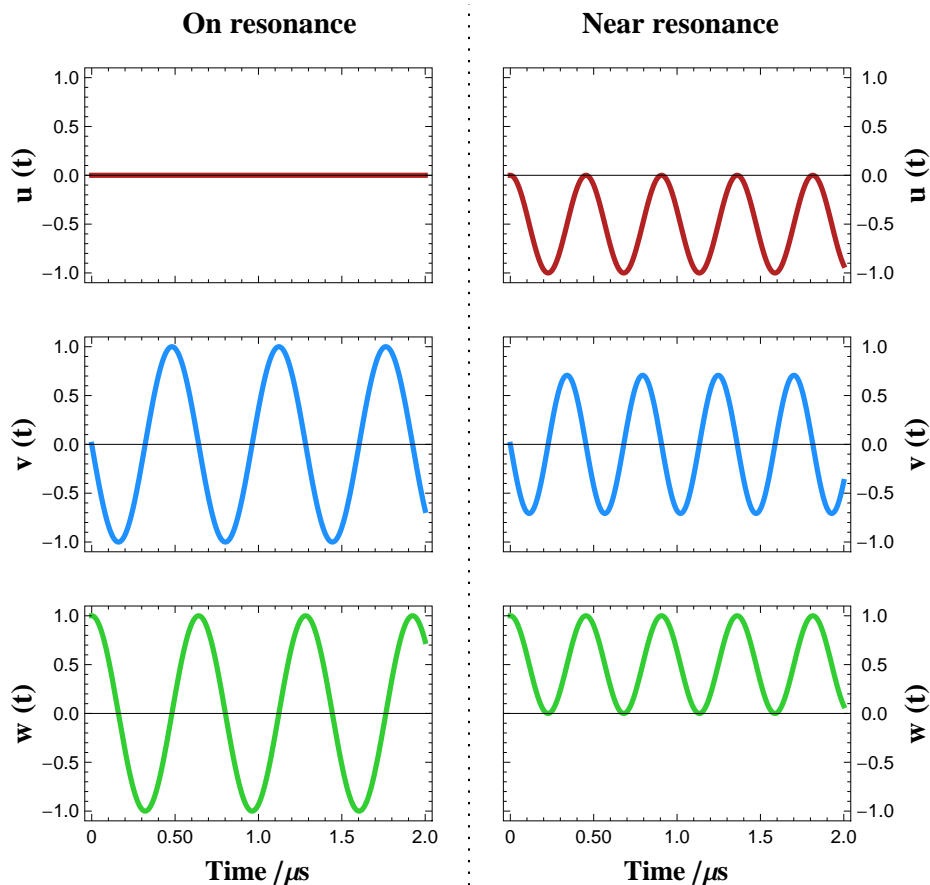


Figure 2.3 The Bloch variables of an ensemble of HCN molecules exposed to a monochromatic pulse of radiation. On the left, the radiation is on resonance ($\Delta = 0$) with the $J = 1 \leftarrow 0$ transition frequency. On the right, the detuning is equal to the Rabi frequency with maximum coherence still obtainable (see text for details). The Bloch variables have been normalized with respect to the initial population difference, w_{eq} , and all relaxation processes have been neglected.

Perhaps a more intuitive method to visualize the transition dynamics is to employ the FVH representation, characterized by Equations 2.38 to 2.40. In Figure 2.4a, the Bloch vector rotates in the vw -plane in response to on resonance radiation. The concept of pi-half and pi-pulses becomes quite clear in this depiction as the coherence is created or destroyed, respectively, at the expense of the population difference. This also seen in Figure 2.4b, where the frequency of

the perturbation is detuned by Ω from molecular resonance. Despite the qualitatively different transition dynamics of Figure 2.4b, maximum coherence can still be achieved.

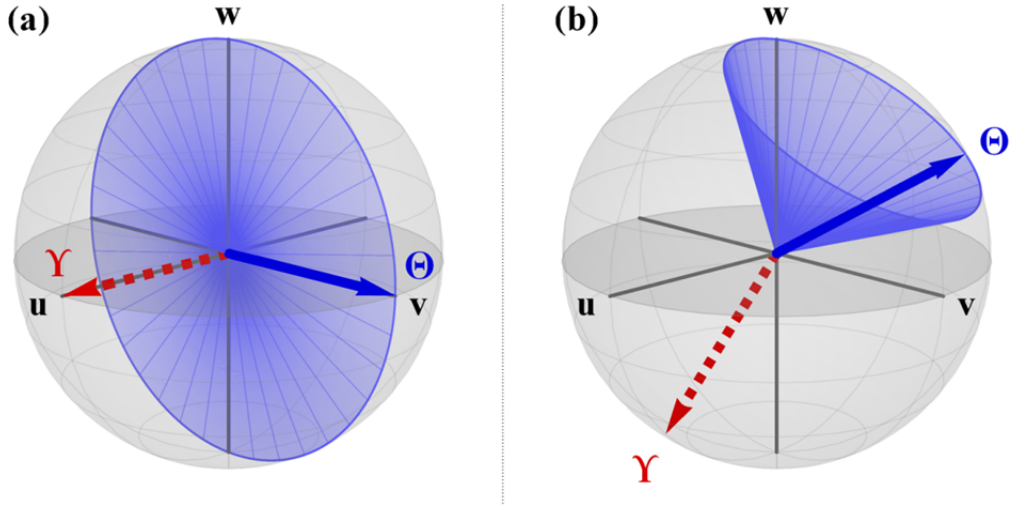


Figure 2.4 The Feynman-Vernon-Hellwarth representation of the response of an ensemble of HCN molecules to a microwave pulse either (a) on resonance or (b) near resonance. The Bloch vector $\vec{\theta}(t)$ traces a closed path along a sphere of radius w_{eq} . The red line representing the torque vector $\vec{\gamma}(t)$ has been scaled to fit into this diagram. Note that all relaxation processes have been neglected.

c) *Transient emission*

At the end of the initial pi-half pulse, the Bloch equations need to be solved for the *field free* case (i.e., $\Omega = 0$) using the result from the previous transient absorption example as the initial boundary condition. By ignoring relaxation terms, the ensemble is described by

$$\left. \begin{aligned} u(t') &= -w_{eq} \sin(\Delta t') , \\ v(t') &= -w_{eq} \cos(\Delta t') , \\ w(t') &= 0. \end{aligned} \right\} \quad 2.46a-c$$

Where $t' = 0$ is equivalent to $t = \tau_{\pi/2}$ and corresponds to the time the radiation is turned off. According to Equations 2.46a-c, the coherence terms will oscillate at the detuning frequency. By substituting $u(t)$ and $v(t)$ into Equation 2.37, the induced macroscopic polarization of the ensemble is therefore defined as

$$\vec{P} = N \vec{\mu}_{2\leftarrow 1} w_{eq} \sin(\omega_{21} t'). \quad 2.47$$

As can be seen from Equation 2.47, the magnitude of \vec{P} is directly proportional to the population difference w_{eq} , which, thanks to the use of a pulsed supersonic jet-expansion, can be of considerable magnitude, especially for low J transitions (refer to §2.1.2 and §2.2.1). Furthermore, \vec{P} will undulate at the molecular transition frequency ω_{21} and, in turn, this oscillating net charge will generate an electromagnetic field. More accurately, each molecule within the ensemble is residing in a superposition state and is, therefore, emitting radiation at the characteristic transition frequency coherently with respect to the rest of the ensemble. It is this molecular signal—known as transient emission—that is detected during an FTMW experiment. Note, if relaxation terms are considered, the emission signal will decay with the relaxation time T_2 .

2.3.2 Instrument Design

The Balle-Flygare FTMW spectrometer of the Jäger group has been described previously in the literature [110]. The instrument setup follows closely the original design proposed by Balle and Flygare [77] with a few notable exceptions. These include orientation of the pulsed-nozzle parallel with respect to the Fabry-Pérot resonator axis to yield a coaxial propagation of the molecular beam [111] and an automated step-scan capability [112]. A brief explanation of several of the key components is given below and a schematic diagram of the instrument is given in Figure 2.5.

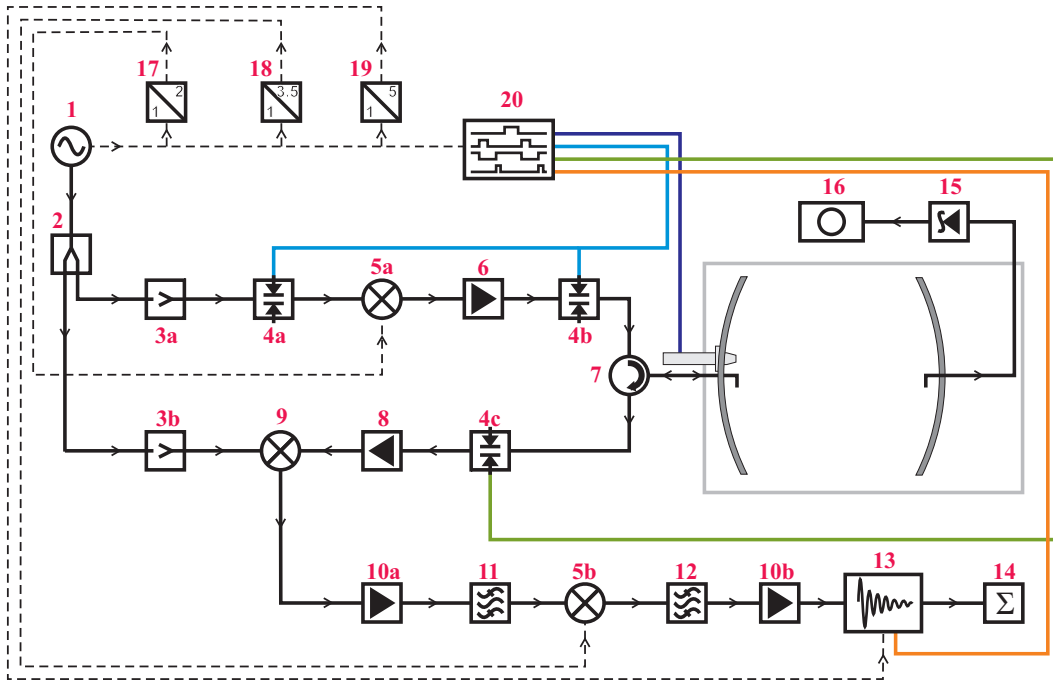


Figure 2.5 A schematic diagram of the Balle-Flygare Fourier-transform microwave spectrometer. The components of the above circuit diagram are defined as follows: (1) continuous-wave microwave synthesizer, (2) power divider, (3) isolators, (4) single-pole-single-throw PIN diode switches, (5) double balanced mixers, (6) microwave power amplifier, (7) circulator, (8) low noise microwave power amplifier, (9) image rejection mixer, (10) radio frequency power amplifier, (11) 20 MHz bandpass filter, (12) 15 MHz bandpass filter, (13) analog-to-digital transient recorder, (14) personal computer, (15) Schottky diode detector, (16) oscilloscope, (17) 2-fold frequency multiplier, (18) 3.5-fold frequency multiplier, (19) 5-fold frequency multiplier, and (20) pulse generator. The dashed black lines represent the radio frequencies used in the double superheterodyne detection that are phase-locked to the 10 MHz internal clock of the microwave synthesizer (1). The colored lines originating from #20 are the TTL trigger signals used to control the nozzle (purple), microwave pulse (light blue), the protective PIN diode switch (green), and the data acquisition (orange).

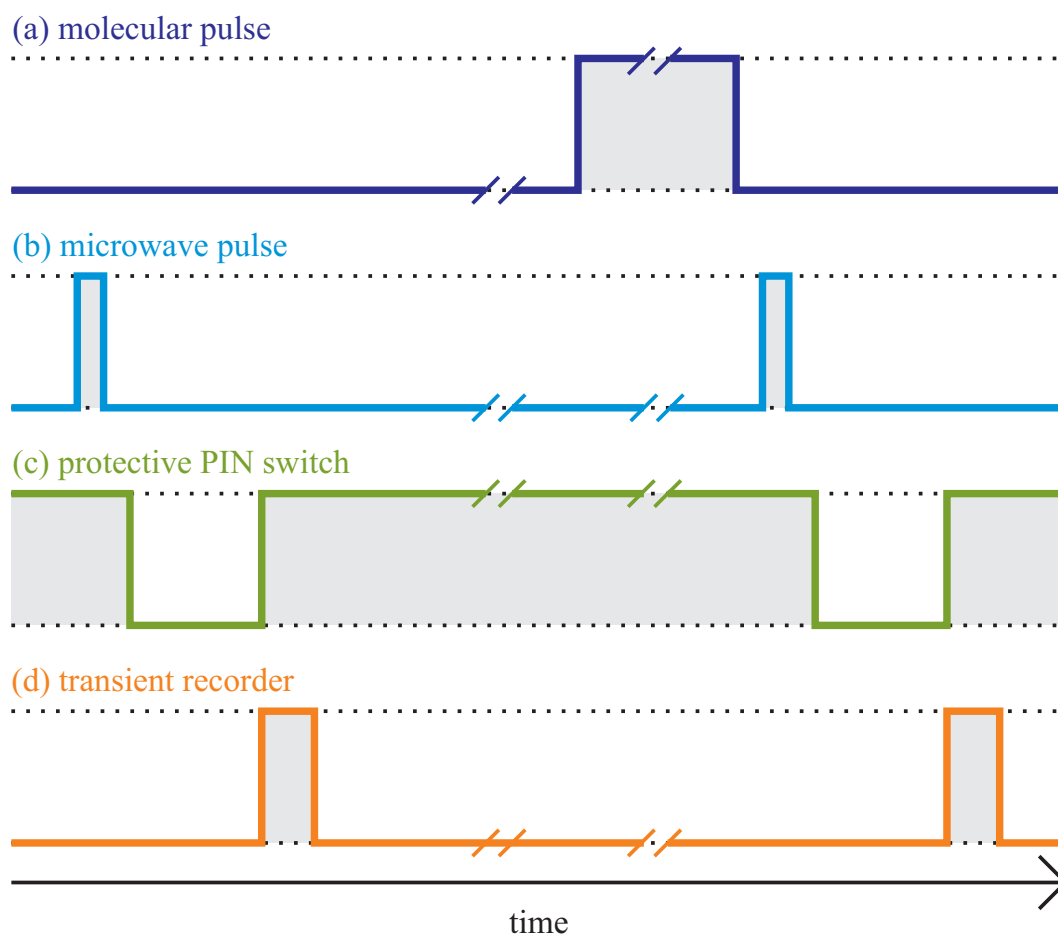


Figure 2.6 A typical pulse sequence used in the Balle-Flygare Fourier-transform microwave spectrometer. The top trace represents the “molecular pulse” (a), which triggers the nozzle to open for only 500–800 μs . The molecular pulse is triggered at half the repetition rate compared to the other triggers—this allows background scans to be measured with each experiment cycle. The “microwave pulse” (b) is subsequently generated, after a 10 μs delay, by switching two PIN switches into the low loss state for 0.5–3.5 μs . To protect the sensitive detection system, a third PIN switch is simultaneously set into the high loss state for 6–12 μs (c). Once the protective switch goes into low loss, data acquisition begins (d). Note, the top and bottom regions of each pulse trace represents that the device is *activated* and *deactivated*, respectively, and not the true electrical TTL signals produced by the pulse generator.

a) *Fabry-Pérot cavity*

The premade sample mixture (discussed in §2.1.2) is pulsed into an evacuated vacuum chamber containing a Fabry-Pérot resonator. This particular type of cavity resonator consists to two spherical aluminum mirrors (diameter 26 cm and radius of curvature 38 cm) separated by a length of 20–40 cm. The position of one of the mirrors can be adjusted along the resonator axis, by a computer controlled motor, in order to tune the cavity to generate a standing wave of the incident microwave radiation. Tuning is monitored by an L-shaped antenna, protruding from the center of the adjustable mirror, which transmits the microwave signal to a Schottky diode detector (#15 in Figure 2.5) and oscilloscope (#16; Tektronix 2220).

The second mirror's position is held fixed and it is conveniently mounted into one of the vacuum chamber flanges. The microwave radiation is coupled into and out of the resonator through the center of this mirror via another L-shaped antenna. The vacuum inside the chamber is maintained by a 12 inch diffusion pump (Edwards Diffstak 250), with a pumping speed of 2000 L/s, supported by a mechanical pump (Edwards E2M40).

The merits of this sample cell design are significant. The quality factor, Q , of this cavity resonator—the ratio of the total stored electromagnetic energy to the power dissipation—is high with typical values of $Q \sim 10^4$ [77, 78, 82, 113]. (Note, this quality factor includes power loss from non-ideal coupling and imperfections in the aluminum mirrors.) Furthermore, the open construction of the Fabry-Pérot resonator is perfectly suited for studying weakly bound clusters generated in a supersonic jet-expansion. If this expansion proceeds parallel to the resonator axis, versus the original perpendicular orientation of Balle and Flygare [77], a significant increase in signal intensity is obtained along with a concomitant 10-fold decrease in linewidths [100, 111].

The increased resolution and sensitivity of the coaxial orientation does come at a price: each transition is Doppler split by an amount $\pm \frac{1}{2} \Delta v_D$. The width of the Doppler splitting is given by the relation [102]

$$\Delta\nu_D = 2\frac{v}{c}\nu_{J+1\leftarrow J}, \quad 2.48$$

where c is the speed of light in a vacuum and v is the velocity of the dopant molecules (i.e., HCN). Assuming that $v = v_T = 1.77 \times 10^3$ m/s (see Equation 2.2 on page 20), the extent of Doppler splitting encountered in this study is predicted to be between $\Delta\nu_D = 0.09$ MHz and 0.31 MHz in the frequency region 8–26 GHz. The issues associated with Doppler splitting are simply complicated rotational spectra and the weaker lines of hyperfine structure potentially being *buried* by more intense peaks (this is especially a concern when the hyperfine splitting is comparable in magnitude to the Doppler splitting).

Another concern regarding this particular cavity resonator is the rate of dissipation of the stored energy. In order to protect the sensitive electronics used in the detection system, a single-pole-single-throw (SPST) PIN diode switch (#4c in Figure 2.5) is used to block the high power radiation from reaching the detector over a period time that includes the pulse duration and a suitable delay period. However, since the Fabry-Pérot resonator has a particularly large quality factor, the energy dissipates much more slowly and the delay period must be longer. The rate of dissipation is governed by the *cavity decay constant*, τ_c [77, 113]:

$$\tau_c = \frac{Q}{\omega} = \frac{Q}{2\pi\nu}. \quad 2.49$$

More specifically, τ_c is the time for the stored energy to reduce to $1/e$ of its original value (or $\sim 37\%$) [77, 84, 113]. For the frequency range of this study (8–26 GHz), calculated decay times using Equation 2.49 yield $\tau_c \approx 60$ ns to ~ 200 ns.

By far the greatest drawback to the Fabry-Pérot resonator is its extremely narrow bandwidth. Only a frequency range of $\nu \pm \frac{1}{2}\Delta\nu$ can be excited, where

$$\Delta\nu = \frac{\nu}{Q} \quad 2.50$$

and ν is the incident radiation frequency [77, 84, 113]. Equation 2.50 effectively limits the experiment bandwidth to $\Delta\nu \sim 1$ MHz. Considering that rotational constants of molecules are typically expressed in GHz and the spacing between rotational lines is on the order of $2B(J + 1)$, refer to Equation 2.10, the majority of rotational spectra consist of vast desolate spans of noise. The situation is dire for weakly bound clusters where theoretical predictions of rotational transitions can be \sim GHz off.

b) Excitation pulse

Macroscopic polarization of the generated $\text{He}_N\text{-HCN}$ clusters is achieved through a short microwave pulse of length τ . The pulse is generated through two switches (#4a and #4b in Figure 2.5) located *downstream* from the continuous-wave microwave synthesizer (HP 83711A). The switches are set to low loss only for a short period ($\tau = 0.5\text{--}3.5$ μs). The input power of the pulse is typically a few mW which, given the above quality factor, generates a field strength of ~ 180 V/m inside the Fabry-Pérot cavity [82, 113].

Besides the pulse length and power, there are other specifications of the microwave pulse that are set based on the detection method. For example, to ensure that the emission signals are properly averaged together with the correct phase, all microwave sources and radio frequencies (RF) are *phase-locked* with respect to a high accuracy frequency standard—for the Balle-Flygare FTMW spectrometer the internal 10 MHz internal clock of the microwave synthesizer is used. This internal reference has a stability of 1.5×10^{-9} parts per day. Note the additional technical considerations regarding the incident pulse given below.

c) Double superheterodyne detection

Since the transient emission signals are extremely weak—field strengths created by the oscillating net dipole of the sample are on the order of 1×10^{-3} V/m [99]—a sophisticated detection system is required. This is achieved through a double *superheterodyne* detection scheme. In order to properly implement this method of detection, the microwave frequency coupled into the cavity is actually

a sideband, offset by 20 MHz from the original microwave frequency, which is generated using a double balanced mixer (#17 in Figure 2.5).

Following a pi-half pulse, the transient emission signal is received through the same L-shaped antenna and is directed, via a circulator (#7), past the protective PIN diode switch (#4c) onto a low noise microwave amplifier (#8). The molecular emission signal can be represented by $\nu_m = \nu - 20 \text{ MHz} + \Delta\nu_m$, where $\Delta\nu_m$ represents the offset of the molecular signal relative to the incident radiation. An image rejection mixer (#9) generates an intermediate frequency (IF) of $20 \text{ MHz} + \Delta\nu_m$ by mixing the molecular emission signal, ν_m , with the original microwave frequency, ν . The IF signal is subsequently amplified (#10a) before transmitted through a 20 MHz bandpass filter (#11).

The resulting IF is then heterodyned a second time with another reference frequency of 35 MHz (produced by component #18). This procedure likewise produces a second IF of $15 \text{ MHz} + \Delta\nu_m$, which is also bandpass filtered at 15 MHz (#12) and amplified (#10b) prior to detection. Note, the prefix in the term superheterodyne refers to the *supersonic* frequency of the IF [114].

The $15 \text{ MHz} + \Delta\nu_m$ signal is digitized by an 8 bit analog-to-digital converter (A/D) transient recorder (#13) with built-in 32 k on-board memory and a sampling rate of 50 MHz, i.e., a sampling interval of 20 ns. The digitized time-domain signal is then transferred to a personal computer (#14), averaged with additional spectra, before being fast Fourier-transformed to yield the frequency power spectrum. Background corrections are included in the averaging process by recording the emission signal with the nozzle closed (this is achieved by only *firing* the nozzle every other cycle) and changing the sign of the double down-converted RF signal.

d) *Timing*

The magnificence of this architecture hinges on the precise control of several key events performed during each experiment cycle. This responsibility falls on the transistor-transistor logic (TTL) pulse generator (#20; BNC M555). A typical pulse sequence used in this study is given in Figure 2.6. Essentially the

sequence begins with a molecular pulse of $\sim 700 \mu\text{s}$ length (nozzle triggered every second cycle) that is followed by a delay time of $10 \mu\text{s}$ before broadcasting the sample with the incident microwave pulse (controlled by two SPST switches; $\tau \approx 2 \mu\text{s}$). During this pulse, a third, protective switch remains in the high loss state until the power inside the Fabry-Pérot resonator has sufficiently dissipated. This additional delay before the protective switch is set to low loss is usually between $5\text{--}8 \mu\text{s}$. At this point, the A/D transient recorder is triggered and the time-domain signal is acquired.

2.4 Chirped-Pulse Broadband Fourier-Transform Microwave Spectrometer

The element that gives the Balle-Flygare FTMW spectrometer unsurpassed sensitivity and resolution, is the very same that limits its bandwidth: the Fabry-Pérot resonator. To reiterate, the spectral window observable per measurement on this type of spectrometer is effectively less than 1 MHz wide and the time required to survey a region of only ~ 100 MHz can easily take over 12 hours using an automated step-scanning method. A significant portion of this time is used to tune the cavity mirrors for the excitation frequency and is sadly unavoidable.

The need for broadband techniques in microwave spectroscopy is undeniable. One such method, akin to the transient phenomena discussed in §2.3, occurs when the frequency of an external radiation field is swept through molecular resonance in a time span comparatively short with respect to T_1 and T_2 . Remarkably, by simply *chirping* the microwave pulse a considerable amount of polarization is created in the sample. This process is known as *fast passage* and one of the first experimental investigations and complete theoretical descriptions in rotational spectroscopy was provided by McGurk *et al.* in 1974 [115]. In their study, however, the authors held the frequency of the applied radiation constant and instead swept the molecular resonance frequency by means of the Stark effect.

Despite the groundbreaking work by the Flygare group, fast passage rotational spectroscopy did not actually come into fruition until ~ 30 years later. The reason for this lag is ascribed to several technical requirements, vital for this method to be properly utilized, which were only made available within the last ten years. These include a waveform generator capable of producing chirps spanning frequencies on the order of GHz in as little time as $1 \mu\text{s}$, which must also be phase-stable to allow coherent signal averaging. Additionally, a high-performance detection system is necessary in order to collect and process the massive amounts of data acquired in a single chirped-pulse experiment.

By exploiting recent breakthroughs in digital electronics, Brown *et al.* [116] developed the first chirped-pulse broadband Fourier-transform microwave (CP-FTMW) spectrometer, in 2006. Several of the key components used in instrument design by the Pate group are as follows. An arbitrary waveform generator (AWG) is used to produce a 1 μs chirp initially spanning 9.5 GHz, which is extended via a series of frequency multipliers, low-pass filters, and mixers to produce a 12 GHz chirp. The excitation pulse is amplified by a high-power 2 kW traveling wave tube amplifier to induce sufficient sample polarization over the spectral width of the chirp. The fast passage emission signal is recorded for 20 μs and phase-coherently averaged via a digital oscilloscope with a digitization rate of 50 Gsamples/s and a hardware bandwidth of 16 GHz. The phase-stability of each component is provided by an external rubidium frequency standard [116-118].

With the introduction of this new broadband FTMW spectrometer, the Pate group have sparked a recent resurgence in microwave spectroscopy. Consequently, my first task as a graduate student was to build a CP-FTMW spectrometer. Working alongside a post-doctoral fellow in the Jäger group, construction and optimization on the broadband instrument was completed within one year and was one of the first instruments of its kind in Canada.

2.4.1 Theoretical Description

a) Fast passage

The behaviour of a molecular ensemble in response to a chirped pulse of radiation can be modelled by means of the optical Bloch equations. Since the detuning frequency has an explicit time-dependence, analytical solutions to Equations 2.36a-c can be derived for fast passage, as shown by McGurk and coworkers [115]. However, the solutions obtained are far too convoluted and only limited information can only be extracted by solving the equations in the limit of infinite detuning or sweep rate.

An alternative method to solving the optical Bloch equations is to use numerical integration procedures, such as the Runge-Kutta method, which are

typically available with most scientific computational software packages. By varying several parameters such as sweep rate, α ; Rabi frequency, Ω ; pulse length, τ ; and initial detuning, Δ_0 ; it becomes quite clear that the transition dynamics are most sensitive to changes in α and Ω . In fact, the ideal values of either parameter, relatively speaking, can be approximated by $\alpha \approx \Omega^2$ and, therefore, any change in the transition dipole moment must be matched by a more significant change in the sweep rate.

To highlight this sensitivity, consider two separate chirped-pulse experiments: one probing the $J = 1 \leftarrow 0$ transition of OCS, $\overline{\mu}_{z_{1 \leftarrow 0}} = 0.42$ D, and another measuring the same transition but of an ensemble of HCN molecules, $\overline{\mu}_{z_{1 \leftarrow 0}} = 1.72$ D (the transition dipole moments are calculated using the rigid rotor approximation). If the electric field strength of the microwave chirp is roughly 2100 V/m, then the Rabi frequencies are approximately 2.8×10^7 rad/sec (4.4 MHz) and 1.1×10^8 rad/sec (18.2 MHz), respectively. In order to optimally excite either species, the sweep rates must be significantly different for these two molecular systems.

In Figure 2.7 the transition dynamics of both species are plotted under the exact same conditions. However, the sweep rate has been set to $\alpha = 1.73 \times 10^{15}$ rad/sec² (275 MHz/ μ s), which is optimized for the OCS transition. In both cases, the $J = 1 \leftarrow 0$ transition frequency is swept through the 2 μ s pulse at $t = 1$ μ s. As seen in Figure 2.7, the pulse generates a substantial amount of coherence almost immediately after $t = 1$ μ s, which persists for the remainder of the chirp. This is in stark contrast to the HCN plots where the greater Rabi frequency and slower sweep rate effectively yields coherent population inversion of the molecular system through *rapid adiabatic passage* (RAP) [102]. Despite this, the HCN sample does in fact become slightly polarized and, thus, will still produce a weak emission signal at the resonance frequency. The fact that a signal is still detectable under far-from-ideal conditions illustrates the strength of this technique.

The unique transition dynamics of OCS and HCN in the above example can easily be seen by their FVH representations in Figure 2.8. During the chirp for OCS, the torque vector inverts at such a rate that $\vec{\theta}$ cannot follow its movement

completely and by the end of the passage the precession of the Bloch vector around \vec{F} happens to occur in the uv -plane. However, for HCN the interaction between the electric dipole and the radiation is notably stronger and the Bloch vector can easily follow the torque vector during its transition. As mentioned above, this process is RAP and is undesirable in chirped-pulse microwave spectroscopy owing to the loss of population difference. As a general rule of thumb, RAP occurs when $\alpha \ll \Omega^2$ [102].

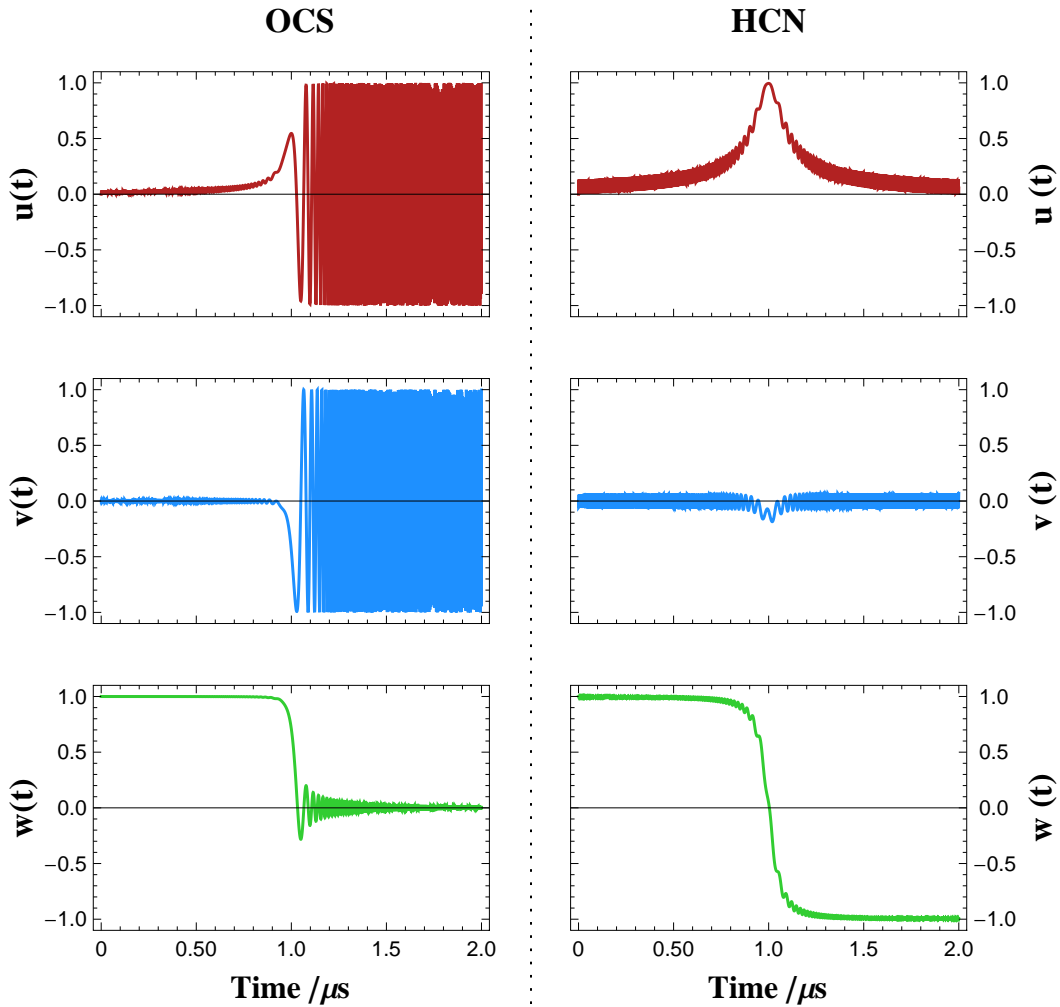


Figure 2.7 The Bloch variables of an ensemble of OCS (left) and HCN (right) molecules in response to identical chirped-pulses optimized for the OCS $J = 1 \leftarrow 0$ transition. The slower sweep rate ($275 \text{ MHz}/\mu\text{s}$) induces maximum coherence in the OCS sample almost immediately after

the resonance frequency is reached at $t = 1.0$. The same sweep rate drives the HCN population into the excited $J = 1$ rotational state.

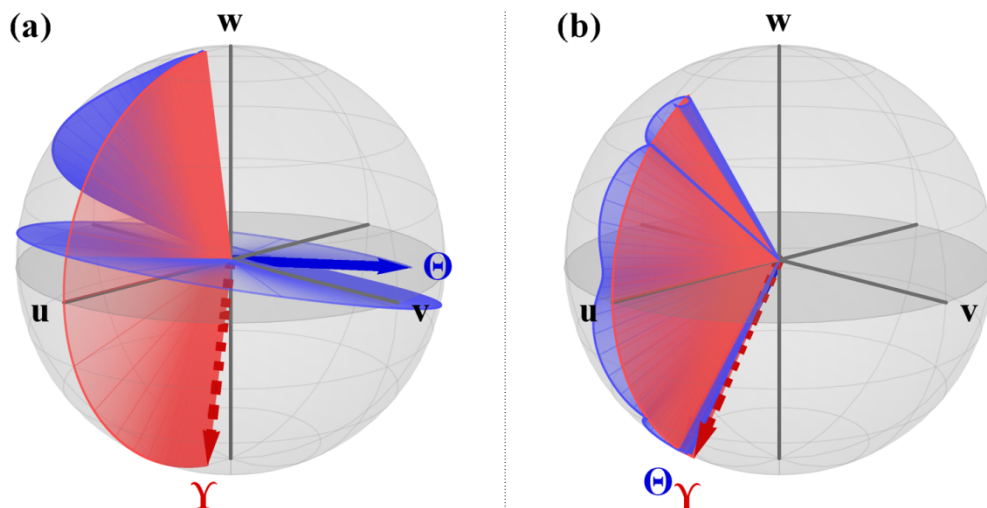


Figure 2.8 A Feynman-Vernon-Hellwarth representation of the transition dynamics of (a) OCS and (b) HCN molecules during a chirped-pulse optimized for the OCS $J = 1 \leftarrow 0$ transition. The paths of both the Bloch vector $\vec{\Theta}$ (blue) and torque vector $\vec{\Gamma}$ (red) for $t = 900\text{--}1100$ ns are shown. The rate of motion of each vector is captured by the opacity of their 200 ns paths—e.g., the diffuse regions represent relatively rapid movement, as seen in (a).

In order to optimize the HCN $J = 1 \leftarrow 0$ emission signal the sweep rate must be increased to roughly $\alpha = 2.98 \times 10^{16}$ rad/sec² (4750 MHz/ μ s), which is modelled in Figure 2.9. What is important to note is how the chirp still produces a considerable amount of coherence in the OCS ensemble, even though the sweep is over 16 times faster! This prediction has been confirmed by the pioneering work by the Pate group [117], who measured the $J_K = 1_0\text{-}0_0$ transition of 1-propyne ($\text{CH}_3\text{C}\equiv\text{CH}$) and monitored the response of signal intensity to various sweep rates from less than 6×10^{13} rad/sec² to nearly 2×10^{16} rad/sec² (10 MHz/ μ s to 3000 MHz/ μ s, respectively).

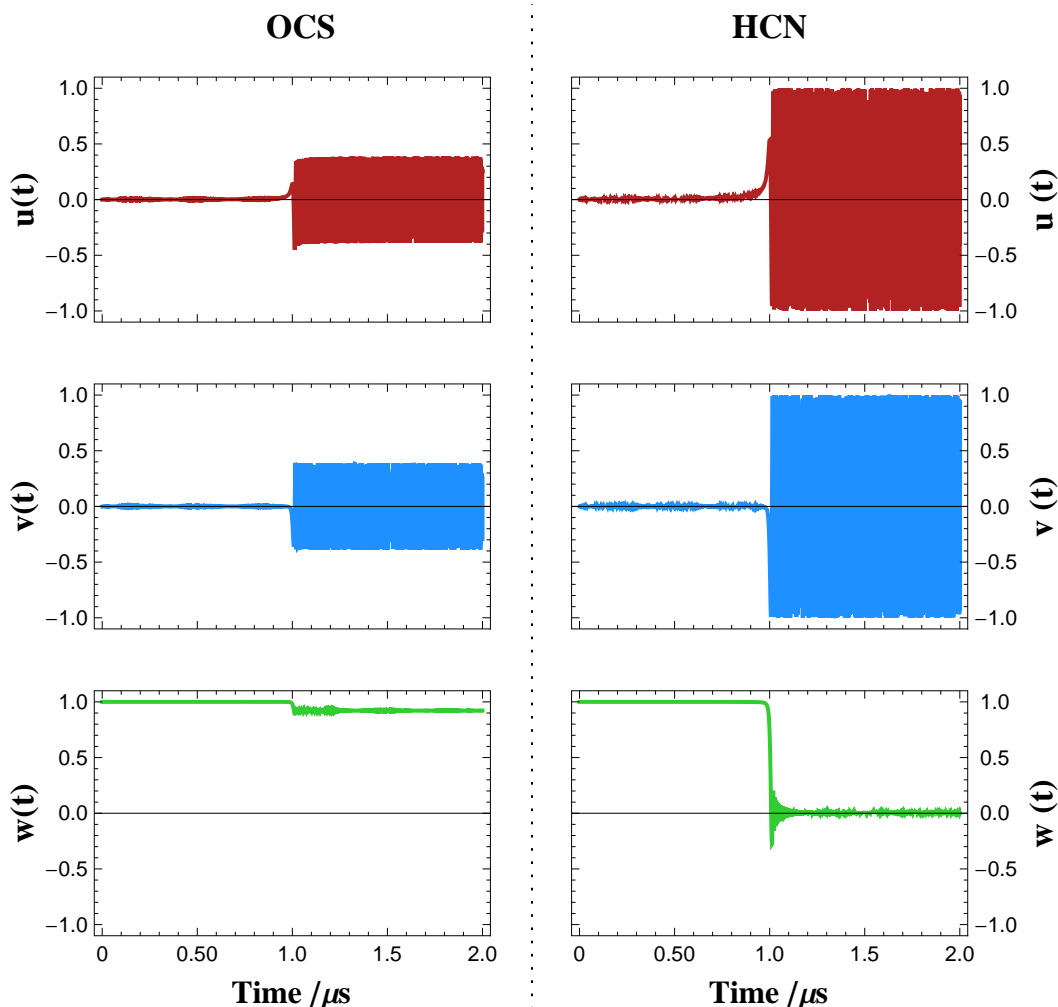


Figure 2.9 The Bloch variables of an ensemble of OCS (left) and HCN (right) molecules in response to identical chirped-pulses optimized for the HCN $J = 1 \leftarrow 0$ transition. The faster sweep rate ($4750 \text{ MHz}/\mu\text{s}$) generates maximum polarization in the HCN sample almost immediately after the resonance frequency is reached at $t = 1.0 \mu\text{s}$. Notice that the same chirp for the OCS ensemble still generates coherence.

b) Emission signal

The emission signal resulting from a fast passage induced polarization can be treated in essentially the same manner as the transient emission in §2.3.1(c). The state of the system at the end of the chirped microwave pulse defines the boundary conditions for the optical Bloch equations in the field free case. If the

sweep rate has been optimized for the molecular system and the transition—i.e., $w(t) \approx 0$ at the end of the chirp—then the solutions to the Bloch equations will be identical to Equations 2.46a-c and, therefore, the polarization will also be described by Equation 2.47.

In the more likely scenario where the sweep rate has not been optimized, then conversion of the Boltzmann population difference into coherence was either incomplete or resulted in coherent population inversion through rapid adiabatic passage. Under such circumstances, the Bloch vector will no longer oscillate in the uv -plane, but instead will repeatedly trace a closed, circular path along either the positive or negative w -hemisphere as described by:

$$\left. \begin{aligned} u(t') &= -\sqrt{w_{eq}^2 - w_f^2} \cdot \sin(\Delta_f t') , \\ v(t') &= -\sqrt{w_{eq}^2 - w_f^2} \cdot \cos(\Delta_f t') , \\ w(t') &= w_f . \end{aligned} \right\} \quad 2.51a-c$$

Here w_f and Δ_f represent the final population difference and detuning frequency, respectively. It is easily seen that the above set of equations are identical to Equations 2.46a-c if w_f equals zero. Consequently, the polarization created during a non-ideal chirp is nearly identical to Equation 2.47 with the exception that w_{eq} is replaced by $\sqrt{w_{eq}^2 - w_f^2}$.

2.4.2 Instrument Design

The setup of our CP-FTMW spectrometer is modelled after the design of Grubbs II *et al.* and their “search accelerated correct intensity” Fourier-transform microwave spectrometer (SACI-FTMW) [119]. The main difference between the SACI-FTMW and CP-FTMW spectrometers are: the inclusion of a Fabry-Pérot resonator for coupling to a second microwave source for double resonance experiments, a 5 W solid state amplifier, and an AWG and digital oscilloscope with lower sampling rates. The first point makes the SACI-FTMW instrument more versatile as it is essentially two microwave spectrometers in one. The remaining modifications were simply aimed at bringing the total cost of the

instrument down, as these three components are by far the most expensive. For example, the current cost of state-of-the-art AWGs, digital storage oscilloscopes, or traveling wave tube amplifiers are approximately \$100k; \$300k, and \$1.3M, respectively.

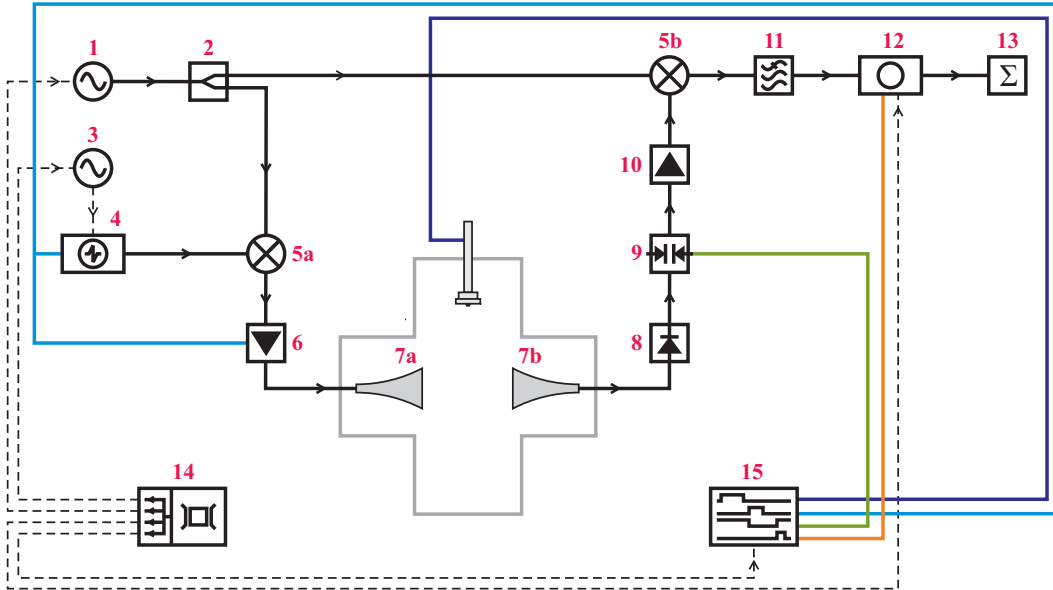


Figure 2.10 A schematic diagram of the broadband chirped-pulse Fourier transform microwave spectrometer. The components of the above circuit diagram are defined as follows: (1) microwave frequency synthesizer, (2) power divider, (3) 3.96 GHz PDRO, (4) AWG, (5) double balanced mixer, (6) 20 W solid state amplifier, (7) high-gain horn antenna, (8) power limiter, (9) PIN diode switch, (10) low noise amplifier, (11) low pass filter, (12) digital storage oscilloscope, (13) personal computer, (14) Rb-frequency standard, and (15) pulse generator. The dashed lines represent the frequency standards used to phase-lock components #1, #3, #4, #12, and #15. The colored lines originating from #15 represent the TTL signals used to control the pulsed-nozzle (purple), the AWG and high-power amplifier (blue), the protective PIN diode switch (green), and the data acquisition (orange).

For the broadband FTMW spectrometer in the Jäger group it was not necessary to include a cavity resonator, which allowed the use of a smaller vacuum chamber and diffusion pump. Furthermore, to increase the likelihood of detecting signals with low transition dipole moments, we opted to use a 20 W high-power solid state amplifier instead. Barring these two modifications, our broadband spectrometer is nearly an identical copy of the design by Grubbs II *et al.* [119] and only brief description of several essential components is given below. A schematic diagram of the CP-FTMW spectrometer is given in Figure 2.10.

a) Chirp excitation pulse

The chirp pulse is generated by a 4.2 Gsample/s AWG (#4 in Figure 2.10; Tektronix AWG710B) that is referenced to an external 3.96 GHz signal generated by a phase-locked dielectric resonator oscillator (PDRO; #3). The AWG produces a 4 μ s chirped pulse, $\Delta\nu_{ch}$, spanning 0.2 GHz to 1 GHz. The chirped pulse is then mixed with a fixed frequency, ν , produced by a microwave synthesizer (#1; Agilent Technologies E8257D) via double balanced mixer (#5a). Upconversion of the pulse produces a chirp, $\nu \pm \Delta\nu_{ch}$, with a spectral width of 2 GHz centered on ν and a *blackout window* of 400 MHz (this corresponds to the range $\nu \pm 200$ MHz that is not explicitly covered by the chirp). The chirped microwave pulse is then amplified to 20 W by means of a high-power solid state amplifier (#6; Microwave Power L0818-43) before being broadcast into an evacuated chamber through a horn antenna.

b) Sample chamber

Instead of a Fabry-Pérot cavity, the sample cell of the CP-FTMW spectrometer consists of a six-way cross aluminum chamber with the molecular beam propagating downward, along the vertical axis. As was the case for the Balle-Flygare FTMW spectrometer, the sample is introduced into the chamber by a pulsed-nozzle and the formation of weakly bound clusters is facilitated by the

supersonic jet-expansion of the molecular beam (refer to §2.1.2). The vacuum chamber is maintained by a 1300 L/s diffusion pump (Edwards Diffstak 160) that is supported by a rotary-vane mechanical pump (Edwards E2M30).

On an axis perpendicular to the molecular beam are two identical, wide-band, high-gain, microwave horn antennas (RF/Microwave Instrumentation ATH7G18) used to broadcast the high-power microwave chirp (#7a) and receive the fast passage emission signal (#7b). The antennas, facing toward one another, are separated by approximately 30 cm and their perpendicular orientation relative to the jet-expansion significantly reduces the extent of Doppler splitting. Unfortunately, this also limits the amount of the time the molecular sample can spend in the active region of the chamber.

By broadcasting such a breadth of frequencies into an aluminum vessel, it is not surprising that a series of spurious microwave signals can be detected in an emission spectrum. To help eliminate these artifacts, the inside of the vacuum chamber is lined with tiles of microwave absorbing foam. Additionally, a background scan is measured before an experiment to help identify spurious signals originating from several of the microwave electronics.

c) Detection system

The broadband fast passage emission signal following coherent excitation is measured via a single downconversion superheterodyne detection method. The detection system includes a power limiter (high-power PIN diode; #8) and SPST PIN diode switch (#9) that protects the low noise amplifier (#10) from the high power microwave pulse. The amplified emission signal, $\nu \pm \Delta\nu_{ch}$, is then heterodyned by another double balanced mixer (#5b) with the same microwave frequency ν , produced by the power divider (#2). This generates an IF of $|\pm\Delta\nu_{ch}|$, which results in *folding* of the rotational spectrum about the center frequency ν . An example of this process is given in Figure 2.11. In order to remove the ambiguity in the observed data, another spectrum must be recorded with a center frequency offset by +10 MHz, for example, and noting whether the peaks are either blue- or red-shifted.

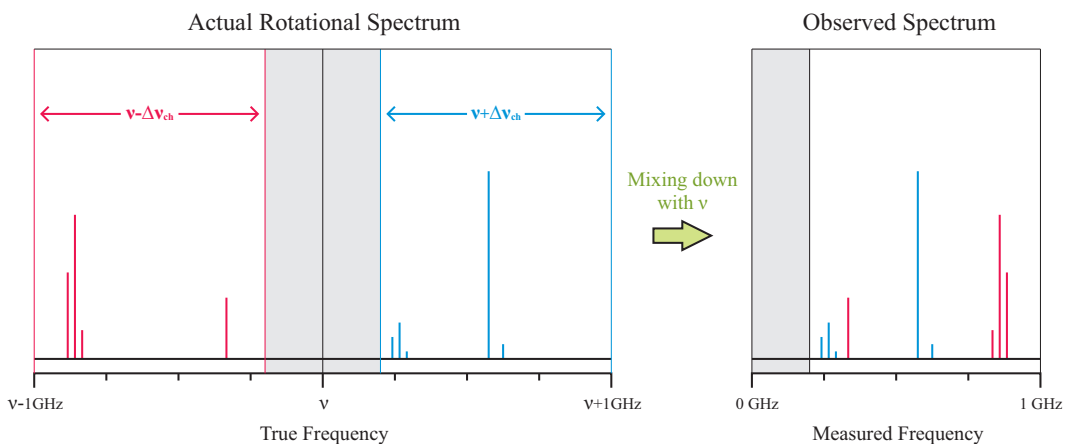


Figure 2.11 A comparison of an actual rotational spectrum during a 0.2–1 GHz chirp pulse centered on ν and the “folded” spectrum observed after mixing down the broadband signal with ν . The red and blue peaks correspond to transition frequencies that are less or greater than the center frequency ν , respectively. The grey area represents the blackout window of $\nu \pm 200$ MHz that is not covered by the chirp.

The IF is filtered with a 4.4 GHz low pass filter (#11) to remove any high frequency artifacts. The final signal is detected by the digital storage oscilloscope (#12; Tektronix TDS6124C), which has a hardware bandwidth of 12 GHz. The oscilloscope both records the time domain signal for 20 μ s with a digitization rate of 40 Gsamples/s for a single pulse and averages it with subsequent pulses during the course of an experiment. At the end of the experiment, the averaged time domain signal is transferred to a personal computer (#13) and is fast Fourier-transformed to generate the power spectrum using scientific software. Since only 1 GHz of bandwidth is being utilized, the resulting spectrum typically has to be truncated. The point-to-point separation of frequencies is only 50 kHz and is defined by the measurement time of 20 μ s. Consequently, to obtain the high-resolution spectra of molecular transitions the Balle-Flygare FTMW must still be used.

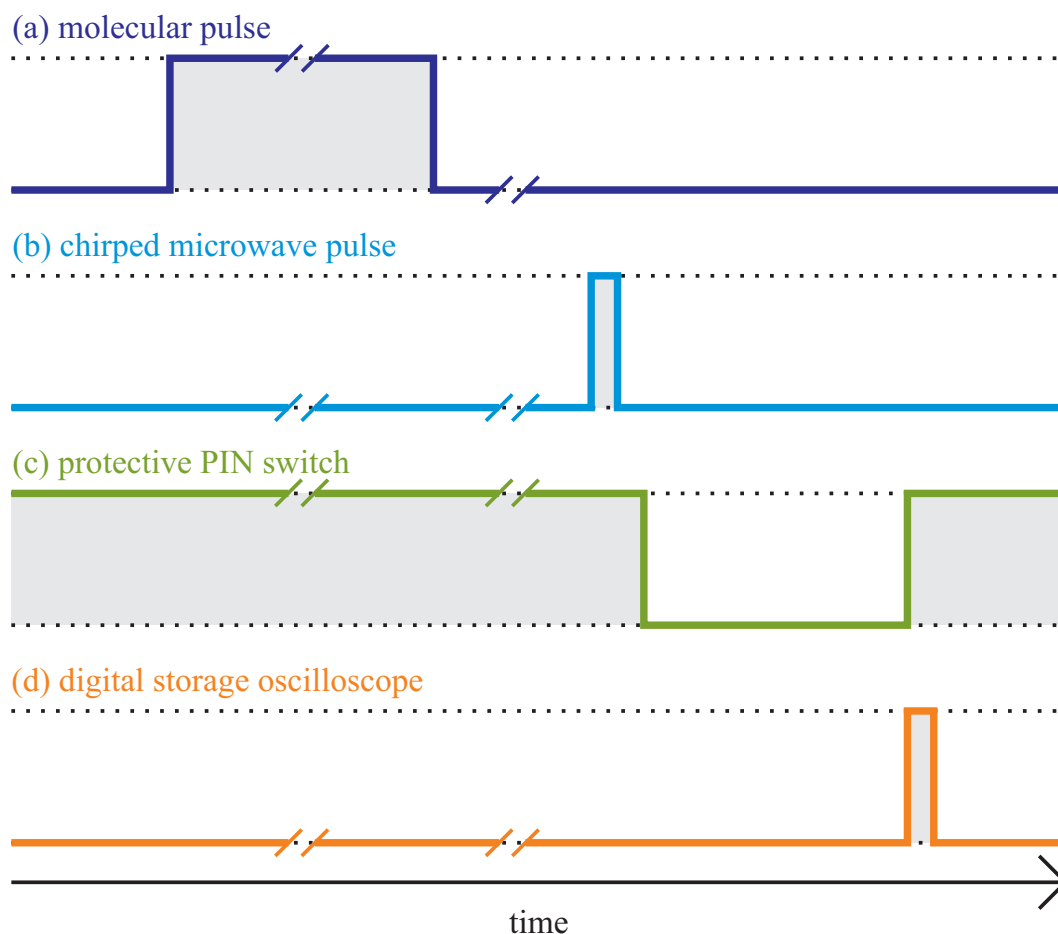


Figure 2.12 A typical pulse sequence used in the chirped-pulse Fourier-transform microwave spectrometer. The top trace represents the “molecular pulse” (a), which triggers the nozzle to open for roughly 300–400 μs . Next, the “chirped microwave pulse” (b) is generated, after a 100–200 μs delay, by activating both the AWG and high-power amplifier for approximately 4 μs . The considerably longer delay between (a) and (b) is necessary to allow time for the jet-expansion to move into the active region of the spectrometer. To protect the low noise amplifier from the high power pulse, a PIN switch is simultaneously set into the high loss state for roughly 5 μs (c). Once the protective switch goes into low loss, data acquisition begins (d). Note, the top and bottom regions of each pulse trace represents that the device is *activated* and *deactivated*, respectively, and not the true electrical TTL signals produced by the pulse generator.

d) Timing

The precise control of the pulsed-nozzle, AWG, hi-power amplifier, protective switch and digital oscilloscope is provided by TTL signals generated by a pulse generator (#15; Stanford Research Systems DG645). An example of the pulse sequence used in the CP-FTMW spectrometer is given in Figure 2.12. The first TTL signal activates the pulsed-nozzle, which opens for 300–400 μs . Since the nozzle is located approximately 20 cm above the horizontal axis of the vacuum chamber, a delay of 100–200 μs is required to allow sufficient time for the jet-expansion to reach the active region between the two horn antennas. At this point the generation of the 4 μs chirped microwave pulse is initiated. A protective switch is used to prevent the high-power pulse from damaging the low noise amplifier. Approximately 1 μs after the pulse, the switch is set to low loss and the oscilloscope is triggered to record the molecular emission signal.

Given the wide frequency ranges used in this instrument, it is crucial that all signals are phase-locked with respect to a high accuracy frequency standard. For this reason the 10 MHz reference signal from a benchtop rubidium frequency standard (#15; Stanford Research Systems FS725) is used. The Rb oscillator of the frequency standard has a short-term stability of less than 2×10^{-11} parts per second.

2.4.3 Optimization

Within the last year there have been several welcomed modifications made to the CP-FTMW spectrometer in our group. The first was simply using a second microwave synthesizer (Agilent Technologies E8257D) in the superheterodyne downconversion step to solve the aforementioned problem of folding observed in our recorded spectra (see Figure 2.11). The second synthesizer is typically set to $\nu + 1.5$ GHz, but any frequency greater than $\nu + \Delta\nu_{ch}$ or below $\nu - \Delta\nu_{ch}$ will suffice. Caution must still be exercised, as strong transitions can still be excited outside the chirp spectral range and depending which side of the offset frequency they fall, these transitions can be folded into the measured spectrum.

Thanks to the tireless efforts of one particularly industrious summer student, the interface and programming of the CP-FTMW spectrometer have been greatly enhanced. This includes control of the pulse generator timing scheme, the oscilloscope digitization parameters, and control of the waveform editor used by the AWG. An additional pulse generator (Stanford Research Systems DG535) was also introduced to independently control the pulsed-nozzle. This has allowed background scans to be measured immediately before a single experiment cycle and for multiple of microwave chirps, or *bursts*, to be measured for a single molecular pulse. These improvements have greatly improved the S/N ratio of molecular signals and reduced measurement times considerably, while almost completely eliminating all artifacts in our microwave spectra.

CHAPTER 3: THE STUDY OF HYDROGEN CYANIDE EMBEDDED IN SMALL HELIUM-4 CLUSTERS USING FOURIER-TRANSFORM MICROWAVE SPECTROSCOPY*

3.1 Introduction

3.1.1 Previous Work

Prior experimental spectroscopic studies of Kr–HCN [86, 89], Ar–HCN [88, 91, 121-125], Ne–HCN [90], and He–HCN [87, 126], have revealed several unusual properties of these van der Waals complexes. They are highly non-rigid, have exceptionally high D_J centrifugal distortion constants which are unusually sensitive to isotopic substitution, require a sixth order centrifugal distortion term for a satisfactory spectroscopic fit, have large amplitude bending angles, show a J -dependence on the ^{14}N nuclear quadrupole coupling constant χ_{aa} [89, 90, 124], and have unusually short bond lengths.

Ab initio calculations of the potential energy surfaces for the rare gas (Rg)–HCN complexes by Toczyłowski and coworkers [127] revealed global minima at the linear, H–bonded configuration and local minima near the T-shaped structure. These results agree with experiment as rotational spectra of Rg–HCN follow that of a linear rotor, with the exception of Ne–HCN, for which Gutowsky *et al.* [90] reported transitions with $K \neq 0$, thus supporting a bent equilibrium structure. However, this assignment is surprising considering previous analyses

* The work presented here has been reproduced in part from Ref. [120] S.P. Dempster, O. Sukhorukov, Q.-Y. Lei, W. Jäger, "Rotational spectroscopic study of hydrogen cyanide embedded in small ^4He clusters", submitted to J. Chem. Phys., 2012.

of Ar–HCN [91, 127] and the authors of Reference [90] acknowledged the difficulty in differentiating rotational K doublets from vibrational l -type doublets.

To date, two experimental studies of HCN doped into helium nanodroplets with $N > 10^3$ were reported. Nauta and Miller [128] determined the rotational constants of HCN and DCN in ^4He nanodroplets in the $\nu(\text{CH stretch}) = 1$ vibrational state, using Stark spectroscopy. Conjusteau *et al.* [129] measured microwave spectra of the ground state, $J = 1-0$ transition of HCN and DCN in ^4He nanodroplets and obtained approximate values for their rotational constants ($B_{\text{eff}} = 1.204(3) \text{ cm}^{-1}$ and $0.999(1) \text{ cm}^{-1}$ for HCN and DCN, respectively). These studies revealed a decrease of only 19% in the gas phase rotational constant of the bare HCN, $B_0 = 1.47822183(4) \text{ cm}^{-1}$ [130]. This small change in B_{eff} is attributed to a breakdown of adiabatic following of the normal-fluid helium density [24, 129, 131].

3.1.2 Theoretical Predictions

Several theory groups have predicted the trend in B_{eff} of $^4\text{He}_N\text{-HCN}$ clusters in the range from $N = 1$ to $N \geq 20$ using quantum Monte Carlo methods [59-61]. The first of these predictions was provided by Viel and Whaley [61] using mixed-frame rigid body diffusion Monte Carlo (RBDMC) and their projector operator imaginary-time spectral evolution (POITSE) implementation. By comparison of the wavefunction amplitudes for the $^4\text{He-HCN}$ dimer, both rotating and nonrotating, the authors suggest that there is negligible adiabatic following of the helium density and, therefore, it cannot be the cause of the 19% reduction in B_{eff} of HCN, but instead claim that this is a result of the proximity of the $^4\text{He-HCN}$ ground state to the potential barrier.

The POITSE simulation also predicts a turnaround in B_{eff} at $N = 3$; which is followed by a gradual, relatively slow approach to the nanodroplet rotational constant limit of HCN—in fact, the authors claim the asymptotic value of B_{eff} will not be reached until well after the first solvation shell. However, the value for B_{eff} at $N = 25$ point is suspiciously large. Not only does it lie well above that of the

nanodroplet limit but, as noted by Paolini *et al.* [60], it is also significantly larger than the gas phase rotational constant of HCN.

The same system was later studied by Paolini *et al.* using *reptation* quantum Monte Carlo (RQMC)—a stochastic technique able to determine the exact expectation values of local observables while lacking the problem of mixed-estimate or population-control biases which have plagued other methods, like diffusion Monte Carlo (DMC) [132]—and determined the *a*-type and *b*-type transitions of ${}^4\text{He}_N\text{-HCN}$ clusters [60]. Their prediction of the rotational energy of the *a*-type transitions ($\approx 2B_{\text{eff}}$) as a function of cluster size N lacked a turnaround point—suggesting that the decoupling of helium density already begins at $N \geq 1$ —and also displays a relatively sudden convergence to the nanodroplet limit at $N \approx 12$, in stark contrast to Viel and Whaley’s results [61]. While the predicted *b*-type transitions also increase in energy before ultimately disappearing at $N \sim 10$.

Paolini *et al.* [60] also attempted to “disentangle” the entwined influence of B_0 and the anisotropy of the He–molecule interaction potential on the dynamics of the solvated chromophores in ${}^4\text{He}$. By creating “fudged” molecular versions of HCN and OCS—the chromophore retaining its potential anisotropy would be calculated using the B_0 of the *other* molecule—and comparing with the results of the *real* HCN and OCS systems, the authors were able to determine that the potential anisotropy of the rotor had the greatest influence on the rotational dynamics of $\text{He}_N\text{-molecule}$ clusters.

The most recent theoretical work on $\text{He}_N\text{-HCN}$ clusters were performed by Mikosz *et al.* [59], who employed fixed-node DMC calculations to predict the evolution of the *a*-type and *b*-type transition frequencies with increasing N . This method requires knowledge of the nodal surfaces of the system’s wavefunctions. The authors obtained these nodal surfaces through a process involving the adiabatic decoupling of angular and radial motions of small $\text{He}_N\text{-HCN}$ clusters in a Borne-Oppenheimer-like approximation, originally proposed by Holmgren and colleagues [133]. By virtue of this procedure, the authors are able to track the solvation dynamics of the $\text{He}_N\text{-HCN}$ clusters and ascribe their behavior to the

efficiency of angular momenta coupling between the HCN molecule and the ^4He atoms.

The DMC predictions of Mikosz *et al.* [59] reveal a turnaround point at $N = 3$, comparable to the POITSE calculation [61]; however, the rotational energies reach the nanodroplet limit quite rapidly at $N = 12$. This latter point is more consistent with the RQMC results [60]. These competing theoretical predictions give greater impetus for an experimental study of the rotational, microwave transitions of $\text{He}_N\text{-HCN}$ clusters.

3.2 Experimental

In order to locate and tentatively assign the *a*-type, $J = 1-0$, transitions of $\text{He}_N\text{-HCN}$ clusters, the chirped pulse Fourier-transform microwave (CP-FTMW) spectroscopy technique [116, 117, 119] was used. The experimental set-up follows very closely the design by the Cooke group [119], and only a brief description is given. A frequency chirped pulse (200–1000 MHz, 4 μs) generated by an arbitrary waveform generator is mixed with the output of a microwave synthesizer to produce 2 GHz wide chirps in the microwave range (with 400 MHz gaps in the center) in the 8–18 GHz range. These pulses are amplified with a 20 W solid state microwave amplifier and then propagated into free space using a wide band, high gain, microwave horn antenna.

The chirped microwave pulse interacts with the molecular ensemble generated by the pulsed expansion of a suitable precursor gas mixture through a General Valve, Series 9, pulsed nozzle. The resulting molecular emission signal is collected by a second, identical horn antenna, passes through a power limiter and a protective microwave switch, and is then amplified by a low noise microwave amplifier. After down-conversion into the frequency range from 0 – 2 GHz, the signal is digitized at a rate of 40 Gsamples/s, transferred to a computer, averaged, and Fourier-transformed to yield the frequency spectrum.

The $J = 1-0$ transitions of $\text{He}_N\text{-HCN}$ clusters with $N > 5$ fall into the frequency range from 18 to 26.5 GHz, and a Balle-Flygare-type [77], cavity-based Fourier-transform microwave (FTMW) spectrometer [110] was used to search for and measure these lines. Additionally, this spectrometer was used to confirm the assignments achieved with the chirped pulse Fourier-transform microwave spectrometer and to study the ^{14}N nuclear quadrupole hyperfine structure of all $J = 1-0$ transitions. The cavity FTMW spectrometer usually required fewer averaging cycles (by a factor from 10 to 100) to achieve a signal to noise ratio comparable to that of the CP-FTMW spectrometer, albeit at a much narrower bandwidth of about 1 MHz.

Hydrogen cyanide was synthesised by mixing a potassium cyanide solution with concentrated sulfuric acid. Helium gas was bubbled through the mixture to carry the evolved HCN through a drying tube filled with calcium chloride into a sample cold trap immersed into a Dewar with liquid nitrogen. The collection time was from 1 to 2 hours. Finally, HCN was transferred to a 3 L glass bulb.

Special attention was paid to avoid water contamination since in supersonic jets HCN will tend to form complexes with water rather than with helium atoms. The $J = 2-1$ transitions of the $\text{HCN-H}_2\text{O}$ dimer [71] fall in the range from 12.1 to 12.2 GHz and were used as water indicator. We estimated that the HCN contained less than 5% water vapour. The HC^{15}N and DCN isotopologues were produced in a similar way, using KC^{15}N and sulfuric acid- d_2 solution in D_2O , respectively. The DCN mixture contained about 10 to 20 % of HCN as a result of H/D exchange in storage and transportation containers. The gas samples contained from 0.002 % to 0.006 % HCN in helium at pressures between 20 to 80 bar.

3.3 Results and Discussion

3.3.1 Rotational Spectra

The CP-FTMW spectrometer was used to find and record the initial spectra of the $J = 1-0$ transitions of the $\text{He}_N\text{-HCN}$ clusters and its isotopologues,

for $N = 1-5$. From previous work it is known that the size of the helium clusters formed in supersonic jets increases with increasing sample backing pressure [35, 40], and we used this dependence to make the N -number assignments.

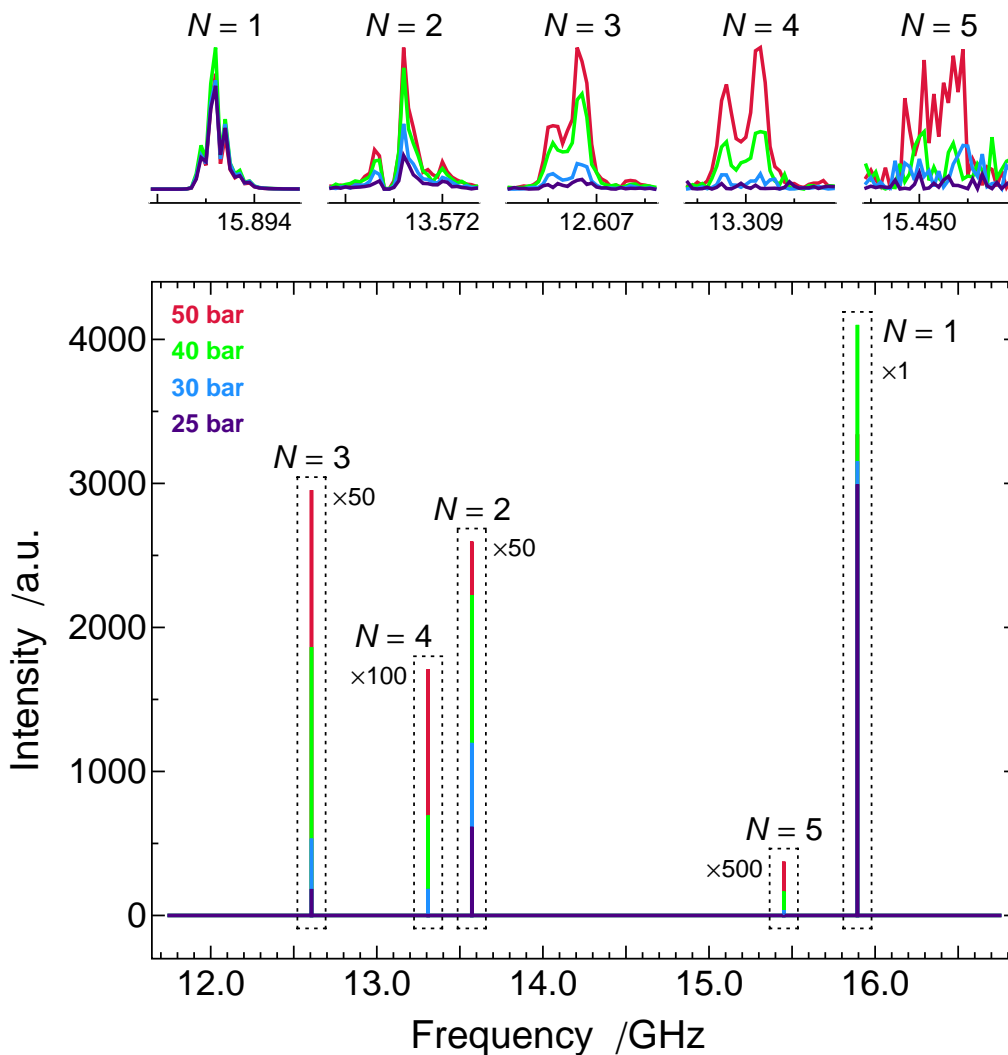


Figure 3.1 The pressure dependence of the a -type, $J = 1-0$, transitions of $\text{He}_N\text{-HCN}$ clusters with $N = 1$ to 5 , recorded on the broadband CP-FTMW spectrometer. The ^{14}N nuclear quadrupole hyperfine structure of the transitions is partially resolved. For the spectra on top, 250 averaging cycles were used. The additional splitting pattern observed in the $\text{He}_1\text{-HCN}$ cluster is attributed to Doppler splitting

Figure 3.1 shows the pressure dependence of the observed spectra. The transitions of the smaller clusters are already observed with relatively high intensities at backing pressures of 20 to 30 bar. The larger clusters ($N > 3$) start to form at higher pressures of 40 to 50 bar, with usually lower intensities. The concentration of HCN in the sample mixture was kept constant at each particular sample pressure. There is only a slight difference in intensity of the He₂-HCN and He₃-HCN transitions in Figure 3.1. This is a result of a variation of the excitation efficiency during the chirped excitation pulse. In the upper part of Figure 3.1, one can see indications of the ¹⁴N nuclear quadrupole hyperfine structures, which could, however, not be fully resolved at the spectral resolution of ~50 kHz.

In order to nicely resolve the hyperfine structures and also to search for transitions of larger clusters that are expected to fall outside the spectral range of the chirped pulse spectrometer, our cavity FTMW spectrometer was used. In total, $J = 1-0$ rotational transitions of He_{*N*}-HCN clusters of five different isotopologues (i.e., those containing H¹²C¹⁴N, H¹³C¹⁴N, H¹²C¹⁵N, D¹²C¹⁴N and D¹³C¹⁴N) with $N = 1$ to 6 were measured. For the sake of brevity, the ¹²C and ¹⁴N isotopes in molecular formula will herein be referred to as simply C and N.

A comparison of the high resolution spectra of He₆-HCN clusters is given in Figure 3.2—note that the spectra of HC¹⁵N containing clusters lack nuclear quadrupole splitting. The $J = 1-0$ transition of the $N = 7$ cluster could only be measured for the DCN containing isotopologue. The search and the identification of other HCN isotopologues with $N = 7$ or even larger clusters was hampered by the operational limits of both spectrometers with the Balle-Flygare-type spectrometer having an upper frequency limit of about 26.5 GHz. Figure 3.3 contains the high resolution spectrum of the $J = 1-0$ transition of He₇-DCN. The assignment of this transition is supported by the ¹⁴N nuclear quadrupole hyperfine structure, which confirms the presence of one HCN molecule and a $J = 0-1$ quantum number assignment. Also the sample pressure dependence and the effect of D₂O/H₂O conditioning of the sample system are consistent with this assignment.

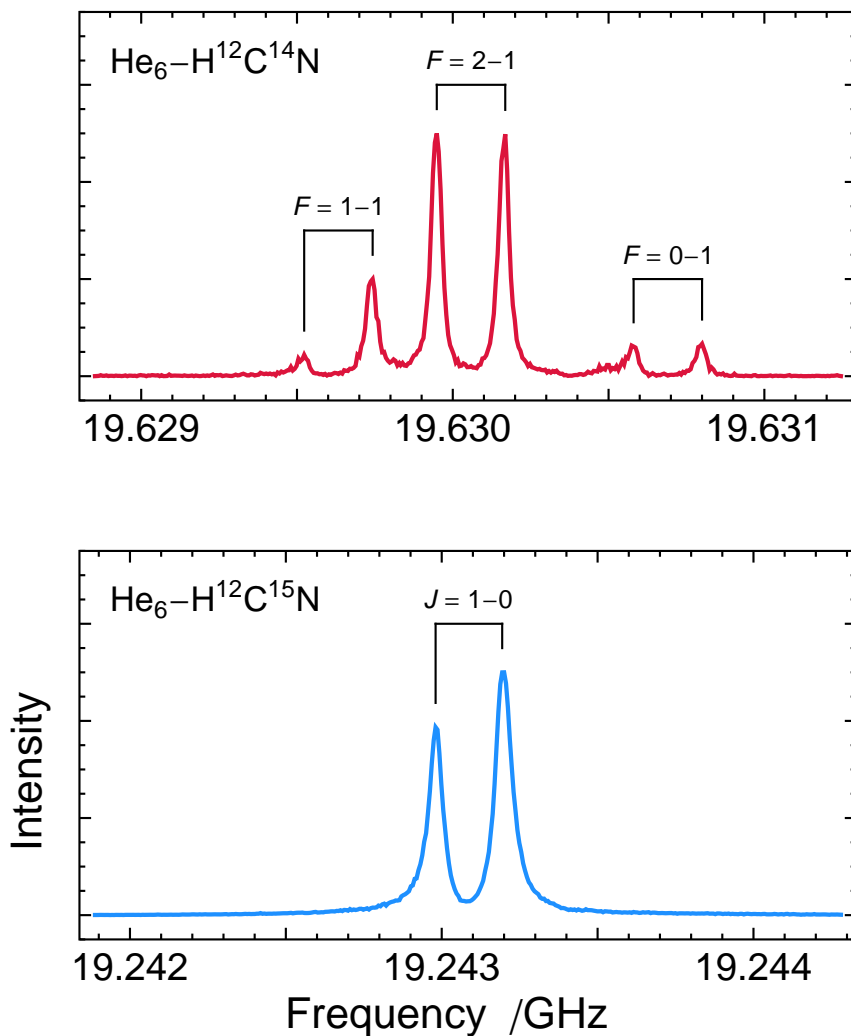


Figure 3.2 A comparison of the $J = 1-0$ transition of $\text{He}_6\text{-HCN}$ measured on the cavity FTMW spectrometer for the most abundant isotopologue, HCN , and HC^{15}N . Each transition is Doppler split due to the coaxial orientation of the molecular beam relative to the axis of the Fabry-Pérot resonator of the instrument. The number of averages per spectra range from 100 (HCN) to 500 (HC^{15}N).

The measured transition frequencies are summarized in Table 3.1. As mentioned above, all microwave transitions, except those of the $\text{He}_N\text{-HC}^{15}\text{N}$ isotopologues, possess ^{14}N nuclear quadrupole hyperfine structure. The quantum

number assignments of the hyperfine components are given in brackets and are consistent with the assignment for He₁-HCN, given by Drucker and coworkers [87].

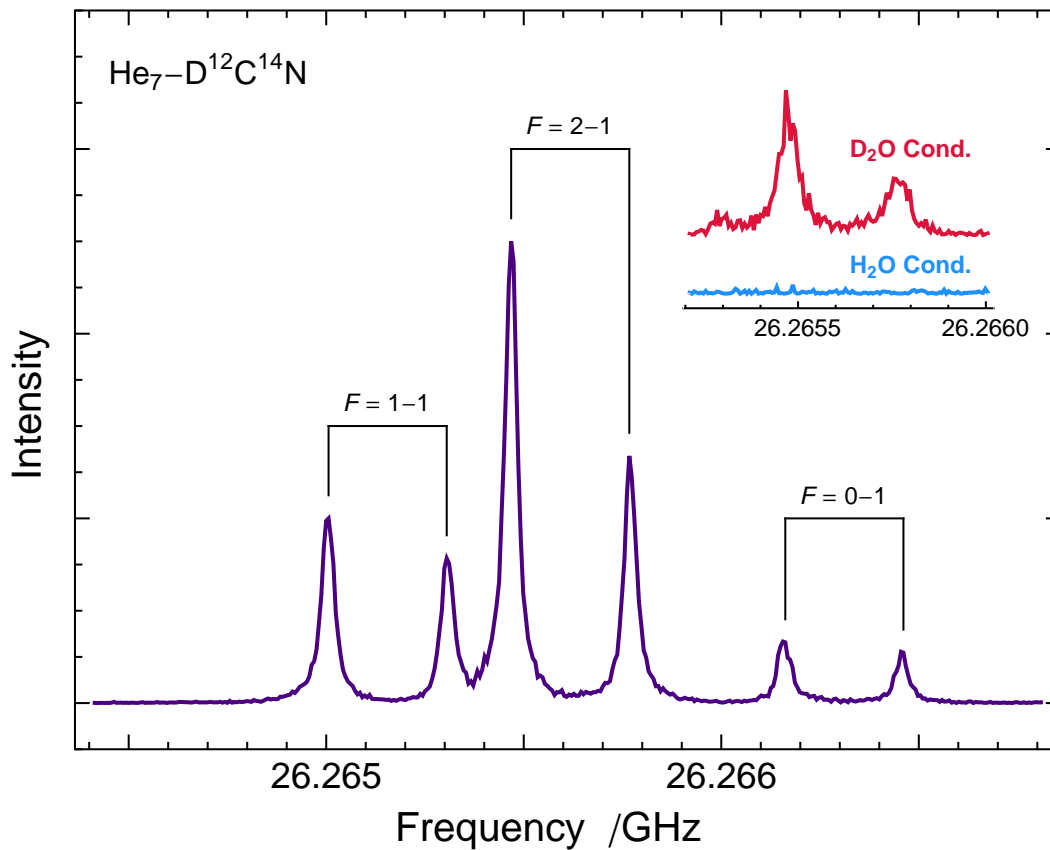


Figure 3.3 The high resolution spectrum of $J = 1-0$ transition of He₇-DCN measured on the cavity FTMW spectrometer. The inset plot shows the result of conditioning the gas handling system with D₂O and H₂O prior to measuring the $F = 2-1$ transition.

Table 3.1 Measured frequencies of the a -type, $J = 1-0$, rotational transitions (in MHz) of $\text{He}_N\text{-HCN}$ clusters and its isotopologues. The ^{14}N nuclear quadrupole hyperfine structures of transitions of ^{14}N containing species could be resolved and the components are labelled with quantum numbers F , corresponding to $F = J + I$, with $I = 1$ being the nuclear spin angular momentum quantum number of the ^{14}N nucleus. The standard deviation of the measured transition frequencies are on the order of \sim kHz.

Size $F'-F$	$\text{H}^{12}\text{C}^{14}\text{N}$	$\text{H}^{13}\text{C}^{14}\text{N}$	$\text{D}^{12}\text{C}^{14}\text{N}$	$\text{D}^{13}\text{C}^{14}\text{N}$	$\text{H}^{12}\text{C}^{15}\text{N}$
He₁					
1-1	15,893.4713	15,822.5977	15,503.0129	15,440.7295	$J = 1-0$
2-1	15,893.6432	15,822.7755	15,503.2902	15,441.0116	15,750.7812
0-1	15,893.8932	15,823.0478	15,503.6964	15,441.4342	
He₂					
1-1	13,571.3801	13,394.4948	12,620.8401	12,501.3434	$J = 1-0$
2-1	13,571.6554	13,394.7754	12,621.2250	12,501.7433	13,378.1963
0-1	13,572.0588	13,395.1994	12,621.8115	12,502.3454	
He₃					
1-1	12,606.5287	12,370.7147	11,401.4905	11,254.0902	$J = 1-0$
2-1	12,606.8616	12,371.0631	11,401.9401	11,254.5540	12,392.1024
0-1	12,607.3586	12,371.5811	11,402.6190	11,255.2433	
He₄					
1-1	13,308.7842	13,017.2524	11,855.5054	11,676.9555	$J = 1-0$
2-1	13,309.1585	13,017.6388	11,855.9842	11,677.4525	13,061.1799
0-1	13,309.7146	13,018.2192	11,856.7146	11,678.1918	
He₅					
1-1	15,449.9993	15,076.9784	13,567.2371	13,337.6699	$J = 1-0$
2-1	15,450.3995	15,077.3918	13,567.7447	13,338.1844	15,149.4787
0-1	15,450.9995	15,078.0070	13,568.5055	13,338.9599	
He₆					
1-1	19,629.6269	19,157.5433	17,141.0312	16,845.3198	$J = 1-0$
2-1	19,630.0524	19,157.9795	17,141.5646	16,845.8631	19,243.0842
0-1	19,630.6812	19,158.6341	17,142.3677	16,846.6767	
He₇					
1-1			26,265.1494		
2-1			26,265.6117		
0-1			26,266.2997		

3.3.2 Rotational Constants

To visualize the trend in the rotational transition frequencies, the data from Table 3.1 are plotted in Figure 3.4 as function of N . Shown is an effective rotational constant, B_{eff} , which was taken as $\frac{1}{2}$ of the $J = 1-0$ transition frequency. In case of hyperfine structure, B_{eff} was determined from the frequency of the strongest, i.e., the $F = 2-1$, component.

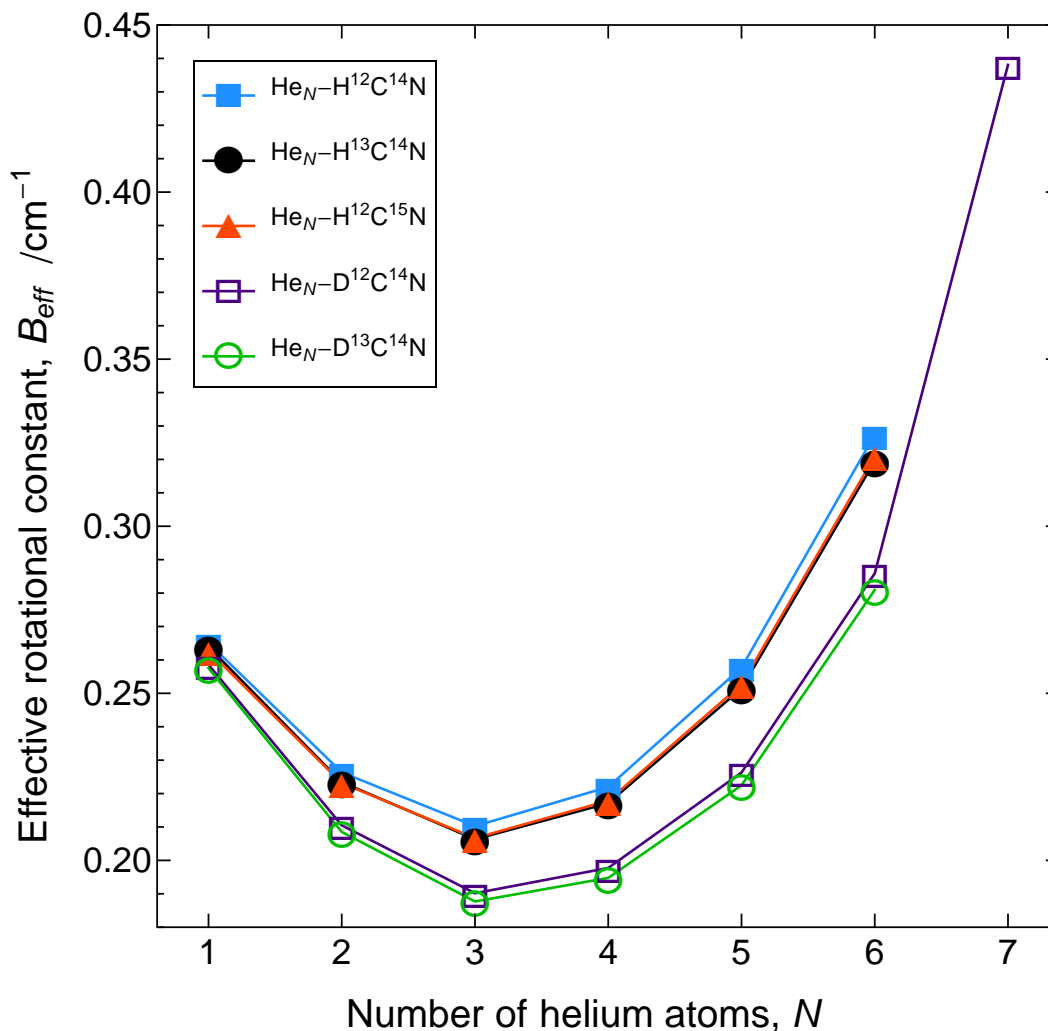


Figure 3.4 The effective rotational constants, B_{eff} , plotted against the number of 4He atoms, N , of several isotopologues of He_N-HCN clusters. The B_{eff} values were taken as $\frac{1}{2}$ of the $J = 1-0$ transition frequency. Note that the uncertainty in each data point is much less than the size of the representative symbol.

The turnaround point in B_{eff} for all the measured HCN isotopologues is at $N = 3$. Beyond $N = 3$, the rotational constants move quickly towards the nanodroplet value, $B_{eff} = 1.204(3) \text{ cm}^{-1}$ for $N \sim 10^3$ [129]. The increase in B_{eff} at $N > 3$ indicates that there is significant decoupling of the helium density from the rotational motion of the chromophore molecule. It is also interesting to note that the behaviour of the B_{eff} is similar to that of $\text{He}_N\text{-CO}$ clusters [40, 41]. In particular, the turnaround point is at $N = 3$ for both chromophores. Furthermore, the B_{eff} for clusters with $N \geq 5$ is greater than the $N = 1$ value, which implies that, for these clusters, less than the equivalent of one helium atom is rotating with the probe molecule. The similarity between $\text{He}_N\text{-HCN}$ and $\text{He}_N\text{-CO}$ clusters can be attributed to the similarity of some of the molecular properties and the similarities in the corresponding He–molecule interaction potentials. For example, the gas phase rotational constant of CO, $B_0 = 1.913 \text{ cm}^{-1}$ [43], also falls into the same, intermediate regime as HCN, following the description of Suárez and coworkers [39]. In addition, the He–molecule interaction potentials for HCN [134] and CO [135] are both weakly anisotropic with well depths of $\sim 29 \text{ cm}^{-1}$ and $\sim 22 \text{ cm}^{-1}$, and binding energies of $\sim 9 \text{ cm}^{-1}$ and $\sim 6 \text{ cm}^{-1}$, respectively.

Despite the aforementioned similarities, the rotational constants of HCN and CO are reduced to $\sim 81\%$ and $\sim 63\%$, respectively, when embedded in helium nanodroplets. The more significant renormalization of CO is attributed to the somewhat higher anisotropy of the He–CO interaction potential. [43] A closer inspection of the data from the current work reveals that the different behavior of HCN and CO embedded in helium nanodroplets manifests itself already in the smaller droplets. Figure 3.5 provides a plot of the incremental effective moments of inertia, $\Delta I = I_N - I_{N-1}$, for $\text{He}_N\text{-DCN}$ and $\text{He}_N\text{-CO}$ calculated from the respective rotational constants. Since the $\text{He}_1\text{-}$ and $\text{He}_2\text{-}$ molecule clusters are asymmetric tops we consider the trends from $N = 3$ onward; the corresponding symmetric top rotational constants allow a more straightforward comparison. The negative values for ΔI in both cases reflect the increase in rotational constant from $N = 4$ on. The more negative slope for $\text{He}_N\text{-DCN}$ is a qualitative indicator of a

greater reduction of helium density that is rotating with the molecule compared to $\text{He}_N\text{-CO}$, which, in turn, can be attributed to the more isotropic He-HCN interaction potential.

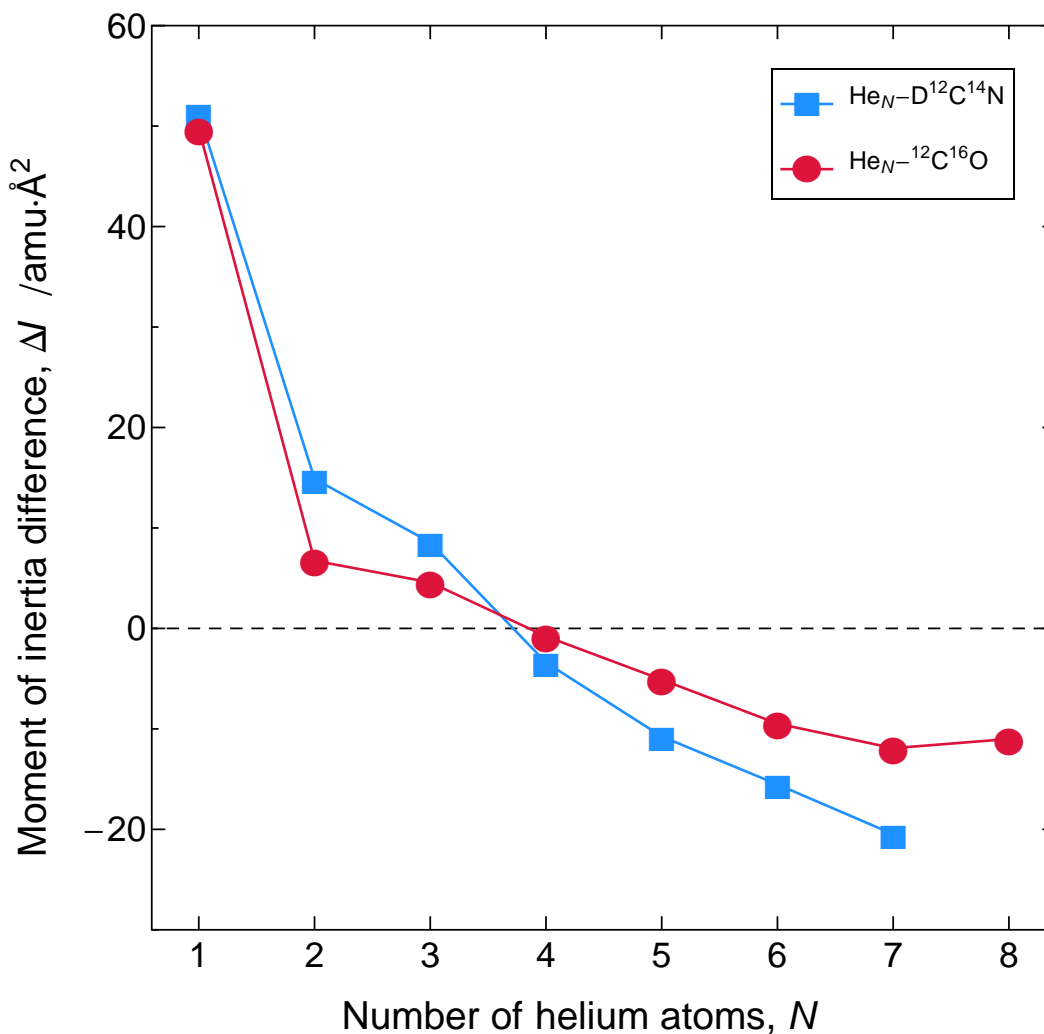


Figure 3.5 Incremental moments of inertia, $\Delta I = I_N - I_{N-1}$, for $\text{He}_N\text{-DCN}$ and $\text{He}_N\text{-CO}$ clusters. The effective moments of inertia of isolated DCN, CO, and $\text{He}_N\text{-CO}$ were calculated using data from References [130], [43], and [41], respectively.

An interesting isotope effect was noted in the trends of the B_{eff} values of $\text{He}_N\text{-H}^{13}\text{CN}$ and $\text{He}_N\text{-HC}^{15}\text{N}$. For $N = 1$ and 2 , the B_{eff} value for the HC^{15}N containing isotopologue is smaller than for $\text{He}_{1,2}\text{-H}^{13}\text{CN}$, which is expected since the helium density will initially accumulate at the hydrogen side. However, from $N = 3$ on, the rotational constants of the H^{13}CN containing clusters become smaller. A similar crossover in B_{eff} is observed for the $\text{He}_N\text{-}^{13}\text{C}^{16}\text{O}$ and $\text{He}_N\text{-}^{12}\text{C}^{18}\text{O}$ clusters between $N = 2$ and 3 [40]. This isotope effect is the result of a combination of factors, such as position of the substituted nucleus relative to the helium density and the change in rotational anisotropy with center of mass shift upon substitution [43, 136]. The former effect has the greatest influence for smaller cluster sizes [136]. In any case, isotope effects in these types of systems appear to be rather complex, as pointed out already by McKellar [136] for the case of $\text{He}_N\text{-CO}$.

Figure 3.6 shows a comparison of the B_{eff} values of $\text{He}_N\text{-HCN}$ clusters determined in this study with those from simulations [59-61]. In regards to overall accuracy, the POITSE method of Viel and Whaley [61] provides, on average, the closest match to the experimental B_{eff} values for $N = 1$ to 6 and reproduces the observed turnaround at $N = 3$. However, the contour of the POITSE predictions is somewhat different from that of the experimental values, as seen in Figure 3.6. As mentioned before, the RQMC predictions by Paolini *et al.* [60] lack a turnaround in B_{eff} . From $N = 3$ on, the trend in the experimental rotational constants is reproduced, but the B_{eff} values from the simulations are significantly higher, indicating a too severe decoupling of helium density from the molecule rotation. The two-level node DMC predictions by Mikosz *et al.* [59] provide the best trend in the B_{eff} values compared to experiment, but also overestimate the rotational constants. Mikosz *et al.* [59] and Paolini *et al.* [60] predict a rapid convergence of the B_{eff} value to the nanodroplet value, that occurs within the first solvation shell, whereas Viel and Whaley [61] propose a slow approach. It would be nice to extend the current study to larger clusters and to determine if the B_{eff} values, for example, overshoot the nanodroplet, as inferred in the case of $\text{He}_N\text{-CO}$ [40].

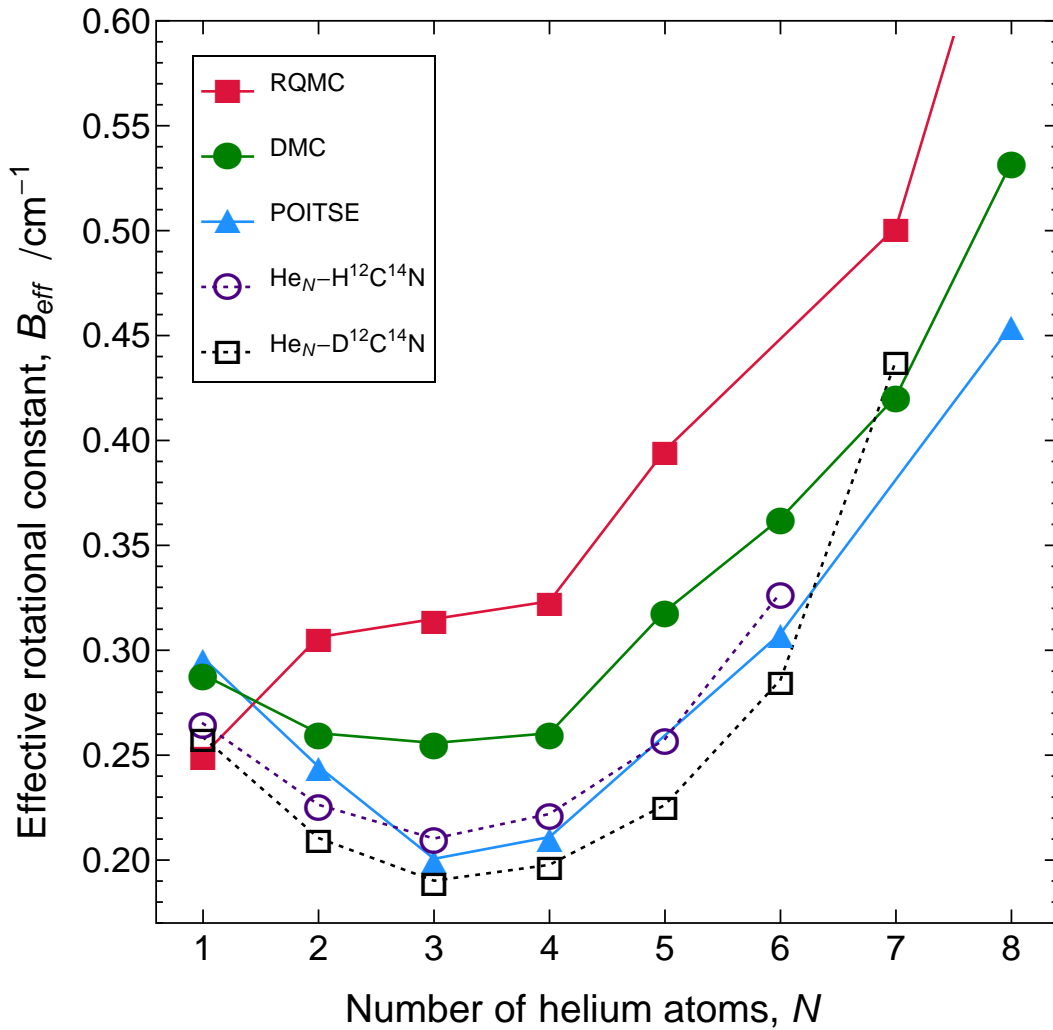


Figure 3.6 Comparison of the effective rotational constants, B_{eff} , of $\text{He}_N\text{-HCN}$ clusters from experiment with previous theoretical predictions. The $\text{He}_N\text{-DCN}$ experimental data have been included as well to emphasize the sharp increase of B_{eff} after $N = 3$. The solid markers and lines pertain to the work of Viel and Whaley [61] (POITSE), Paolini *et al.* [60] (RQMC), and Mikosz *et al.* [59] (DMC).

3.3.3 ^{14}N Nuclear Quadrupole Hyperfine Structure

In “regular” semi-rigid molecules, the nuclear quadrupole hyperfine structures of rotational transitions and the derived nuclear quadrupole coupling constants are delicate probes of the electronic environment of the respective atom with a quadrupole nucleus. In the case of weakly bound clusters it is typically assumed that the electronic and structural properties of the molecular monomers are not altered upon formation of the weak bond—this assumption has been justified previously by comparing the spin-spin and nuclear quadrupole coupling constants in Ar–DF [94]. Under these circumstances, the nuclear quadrupole coupling constants contain information about the orientation of the molecular monomer within the principal inertial axes system of the cluster. The nuclear quadrupole coupling constants of the cluster are then given by the projections of the monomer coupling tensor onto the a -, b -, and c -inertial axes of the cluster. For a linear monomer $\chi_{gg} = \chi_0 \langle P_2(\cos \theta) \rangle = \frac{1}{2} \chi_0 \langle 3 \cos^2 \theta - 1 \rangle$.

Here, χ_{gg} represents the nuclear quadrupole coupling constant of the cluster measured along $g = a, b,$ and c principal inertial axes, χ_0 is the coupling constant of the free molecule (the ^{14}N quadrupole coupling constants for HCN and DCN are $-4.70789(8)$ MHz and $-4.70396(47)$ MHz, respectively [62]), and θ is the instantaneous angle between the g -inertial axis of the complex and the (linear) monomer axis. The brackets indicate an average over the internal large amplitude bending motion of the system. A summary of the hyperfine structure data for ^{14}N nucleus containing isotopologues is provided in Table 3.2.

For a system near the semi-rigid rotor limit, the above equation can be solved for θ to give an effective bending angle, θ_{eff} , which contains some structural information. However, for a system near the free internal rotation limit, the $\langle P_2(\cos \theta) \rangle$ values carry information about the potential anisotropy in the angular coordinate. The $\langle P_2(\cos \theta) \rangle$ values are also influenced by the relative mass of the monomer with the quadrupolar nucleus in the sense that a heavier monomer determines, to some degree, the orientation of the principal axes of the moment of inertia tensor.

Table 3.2 Summary of the ^{14}N nuclear quadrupole coupling constants, χ_{aa} , in MHz and $\langle P_2(\cos \theta) \rangle$ values for the ^{14}N containing isotopologues of $\text{He}_N\text{-HCN}$ clusters. The standard deviation in both quantities was determined to be 0.001 MHz and 0.0003, respectively.

Size	$\text{H}^{12}\text{C}^{14}\text{N}$	$\text{H}^{13}\text{C}^{14}\text{N}$	$\text{D}^{12}\text{C}^{14}\text{N}$	$\text{D}^{13}\text{C}^{14}\text{N}$
He₁				
χ_{aa}	-0.564	-0.599	-0.913	-0.940
$\langle P_2(\cos \theta) \rangle$	0.1199	0.1272	0.1942	0.1998
He₂				
χ_{aa}	-0.907	-0.939	-1.293	-1.336
$\langle P_2(\cos \theta) \rangle$	0.1927	0.1994	0.2749	0.2839
He₃				
χ_{aa}	-1.107	-1.156	-1.504	-1.539
$\langle P_2(\cos \theta) \rangle$	0.2352	0.2456	0.3197	0.3271
He₄				
χ_{aa}	-1.242	-1.289	-1.610	-1.650
$\langle P_2(\cos \theta) \rangle$	0.2637	0.2738	0.3422	0.3507
He₅				
χ_{aa}	-1.334	-1.373	-1.691	-1.719
$\langle P_2(\cos \theta) \rangle$	0.2833	0.2916	0.3596	0.3655
He₆				
χ_{aa}	-1.408	-1.454	-1.781	-1.809
$\langle P_2(\cos \theta) \rangle$	0.2990	0.3089	0.3787	0.3847
He₇				
χ_{aa}			-1.535	
$\langle P_2(\cos \theta) \rangle$			0.3263	

The $\langle P_2(\cos \theta) \rangle$ values for four $\text{He}_N\text{-HCN}$ isotopologues are plotted in Figure 3.7, together with those of the $\text{He}_N\text{-N}_2\text{O}$ [48] and $\text{He}_N\text{-HCCCN}$ [137] clusters. The value for $\text{He}_1\text{-HCN}$ is close to zero, indicating nearly free internal rotation of the HCN unit within the complex, in accord with the low angular anisotropy of the He-HCN interaction potential [87]. As the number of helium atoms increases, the $\langle P_2(\cos \theta) \rangle$ values increase smoothly; this is interpreted as an

increasingly hindered internal rotation. For $\text{He}_7\text{-DCN}$, there is a sharp decrease in this value. In the cases of $\text{He}_N\text{-N}_2\text{O}$ [48] and $\text{He}_N\text{-HCCCN}$ [137], $\langle P_2(\cos \theta) \rangle$ shows little variation with N , which is probably related to the larger mass of the monomers, as mentioned above. For $\text{He}_N\text{-HCN}$, it is interesting to note that the turnaround in B_{eff} at $N = 3$ occurs without a concomitant feature in $\langle P_2(\cos \theta) \rangle$.

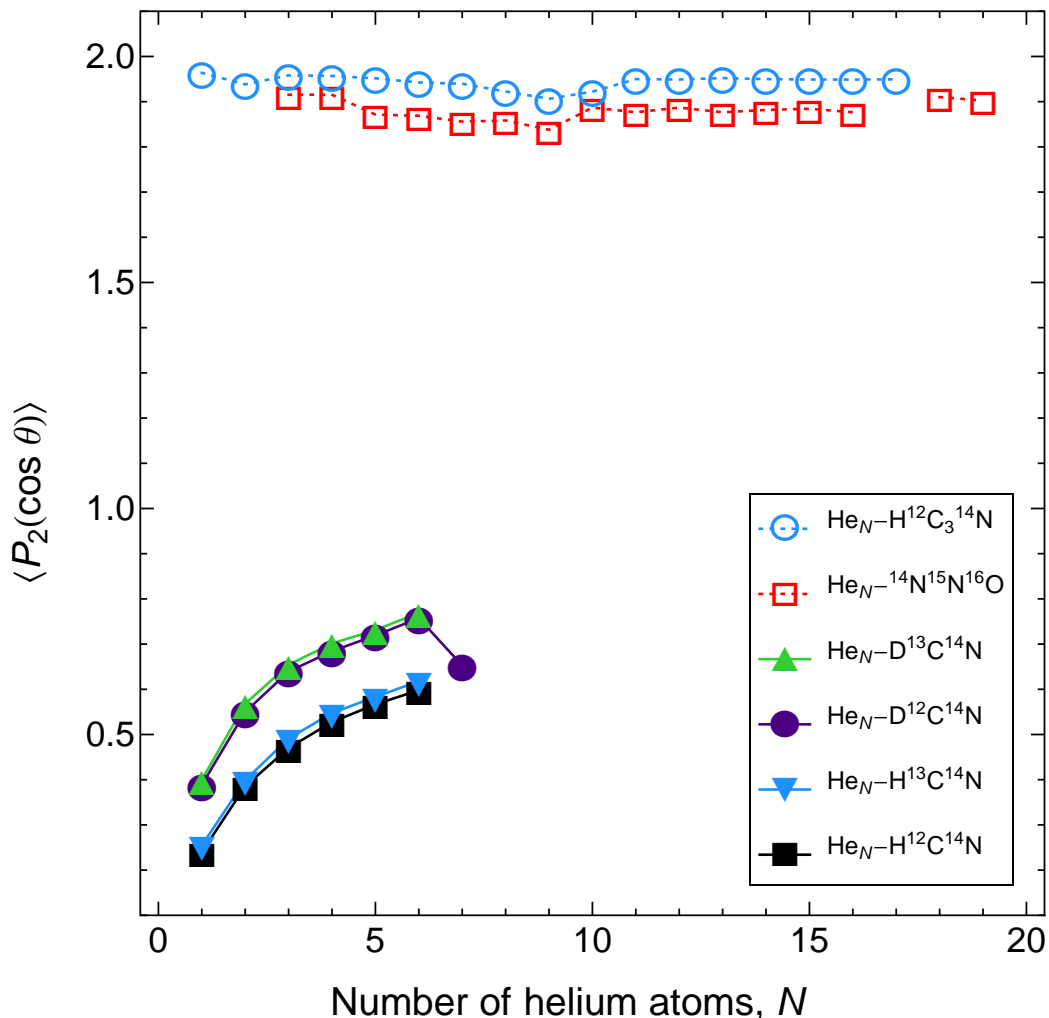


Figure 3.7 A comparison of $P_2(\cos \theta)$ values from the ^{14}N hyperfine structures of rotational transitions of $\text{He}_N\text{-HCN}$, $\text{He}_N\text{-N}_2\text{O}$, and $\text{He}_N\text{-HCCCN}$ isotopologues as a function of cluster size. The data for the N_2O and HCCCN containing clusters are taken from References [48] and [137], respectively.

The sudden drop in $\langle P_2(\cos \theta) \rangle$ for He₇-DCN could be experimental evidence for the incremental helium density shifting from the H/D end to the N side of the monomer, which has been predicted by Paolini *et al.* [60] to occur at $N = 6$. Despite confidence in the assignment of the He₇-DCN line, it is still worth urging caution in this interpretation, as the He₇-D¹³CN has yet been measured to confirm this trend.

It is clear, however, that the hyperfine structure of the He_N-HCN clusters is influenced by the helium distribution around the chromophore and, consequently, contains information about the incremental change in the helium density. However, since the structural information of these weakly bound systems is averaged over the large amplitude motions, it can no longer be extracted from experimental measurements alone. It would therefore be very insightful if the χ_{aa} and $\langle P_2(\cos \theta) \rangle$ values could be calculated in theoretical simulations to be compared against these results.

3.3.4 Helium Density Distribution

The rotational constants of the He_N-HCN clusters are inversely proportional to the corresponding moments of inertia, and contain thus information about the mass distribution within the clusters. For He_N-OCS clusters with $N = 1$ to 8, it was possible to obtain qualitative information about the location of the incremental helium density from the moments of inertia, when going from N to $N + 1$ helium atoms. This information could be extracted by comparing magnitudes of moment of inertia changes and by assessing the moment of inertia changes of different isotopologues. The experimentally determined trend is in accord with that found from subsequent path integral Monte Carlo simulations [38]. It was hoped that the rich isotopic data available for the He_N-HCN clusters would allow for a similar analysis. It turns out, however, that the moments of inertia are “contaminated” by the significant increase in superfluid helium fraction already at low N -values.

Table 3.3 The $|z|$ coordinates of $\text{He}_N\text{-HCN}$ determined by the Kraitchman substitution procedure. The coordinates are given in Å.

N	$\text{He}_N\text{-H}^{12}\text{C}^{14}\text{N}$		
	H	^{12}C	^{14}N
1	1.24	0.52	0.75
2	2.33	0.98	1.02
3	2.86	1.22	1.17
4	3.01	1.29	1.19
5	2.97	1.26	1.13
6	2.70	1.11	1.01

Table 3.4 A comparison of the molecular radii, r_s , determined from Kraitchman substitution analysis, of two light rotors (HCN and CO) and two heavy rotors (OCS and N_2O) weakly bound to N ^4He atoms. Note, $\Delta r = r_s - r$; where r is the accepted length of the molecule (or the N=N bond length in N_2O) with values of $r_{\text{HCN}} = 2.2187(5)$ Å [62], $r_{\text{CO}} = 1.12834(1)$ Å [138], $r_{\text{OCS}} = 2.7171(14)$ Å [62], and $r_{\text{N=N}} = 1.1281(8)$ Å [138]. The experimental B_{eff} values of $\text{He}_N\text{-CO}$ [40, 41], $\text{He}_N\text{-OCS}$ [35], and $\text{He}_N\text{-N}_2\text{O}$ [48] were used in the same fashion to determine the $|z|$ coordinates for their respective nuclei.

N	$\text{He}_N\text{-H}^{12}\text{C}^{14}\text{N}$		$\text{He}_N\text{-}^{12}\text{C}^{16}\text{O}$		$\text{He}_N\text{-}^{16}\text{O}^{13}\text{C}^{32}\text{S}$		$\text{He}_N\text{-}^{15}\text{N}_2^{16}\text{O}$	
	$r_{s,\text{HCN}}$	Δr	$r_{s,\text{CO}}$	Δr	$r_{s,\text{OCS}}$	Δr	$r_{s,\text{N=N}}$	Δr
1	1.99	-0.23	0.92	-0.21				
2	3.35	1.13	1.43	0.30	2.71	-0.01		
3	4.03	1.81	1.76	0.63	2.68	-0.03	1.15	0.02
4	4.20	1.98	1.98	0.85	2.65	-0.07		
5	4.10	1.88	2.11	0.98	2.63	-0.09		
6	3.71	1.49	2.09	0.96	2.81	0.10	1.12	-0.01
7			1.89	0.76	2.81	0.09	1.13	0.01
8			1.59	0.46			1.20	0.07
9							1.16	0.03
10							1.24	0.11

The moments of inertia provide, of course, only a measure of the normal fluid helium density distribution (and the HCN location), and it is not possible to separate the effects of total mass increase, change in superfluid fraction, and helium density redistribution upon addition of a further helium atom. For example, calculation of the Kraitchman substitution coordinates [97], $|z|$, for the H, C, and N atoms was attempted (see Table 3.3). For $N = 2$ to 6, unrealistic values for the C–N bond distances between 2.0 and 2.5 Å were obtained (the C–N distance in isolated HCN is 1.1532(1) Å [62]).

This discrepancy is not only a problem for HCN, but appears to be the case for all comparatively light rotors. Table 3.4 contains the molecular radii, r_s , determined by Kraitchman substitution analysis for two light rotors (HCN and CO) and two heavy rotors (OCS and N₂O) seeded in small clusters of ⁴He. Table 3.4 also includes the difference between these r_s from the accepted molecular radii of the bare chromophore.

The discrepancies presented in Table 3.4 are significant for the light rotors, with deviations of nearly 2 Å (or ~ 90% difference). However, a full propagation of error for HCN and CO accounts for only 0.1-0.2 Å. This usually implies that error lies within the method itself (i.e., questioning the validity of approximations made); however, if this were true then it would not be restricted to light rotors. This is clearly not the case as OCS and N₂O themselves show a much more reasonable agreement of ~0.1 Å between the calculated r_s and their actual radii. It appears that a detailed interpretation of the cluster rotational constants in terms of, for example, changes in helium density distribution and variation of superfluid helium fraction, awaits the completion of path integral Monte Carlo simulations, similar to those done for He_N-N₂O [51] and (*para*-H₂)_N-CO [139].

3.4 Summary

The high resolution spectra of the a -type, $J = 1-0$ transitions of several isotopologues of $\text{He}_N\text{-HCN}$ clusters, with N ranging from 1 to 7, have been measured. A plot of the effective rotational constants, B_{eff} , versus cluster size N reveals a turnaround at $N = 3$ and a subsequent fast approach to the ^4He nanodroplet limit. These experimental results closely resemble those of $\text{He}_N\text{-CO}$ and its isotopologues [40, 41] and is attributed to the similarities in the respective He–molecule interaction potentials.

Upon comparison with previous quantum Monte Carlo simulations on the rotational transitions of $\text{He}_N\text{-HCN}$ clusters [59-61], the fixed-node DMC predictions of Mikosz *et al.* [59] reproduce the contour of the experimental B_{eff} versus N data well for cluster sizes $N = 1$ to 4, but do not capture the steep increase in rotational constant observed in the $N = 6$ and $N = 7$ clusters.

Analysis of the ^{14}N nuclear quadrupole hyperfine data suggests that the internal rotation of the HCN unit within the cluster becomes increasingly hindered upon the further addition of ^4He atoms. A marked drop in $\langle P_2(\cos \theta) \rangle$ is observed for $\text{He}_7\text{-DCN}$ and potentially provides experimental evidence for a shift in the incremental helium density from the linear (H/D side) to the anti-linear (N end) configuration. This shift has been predicted to occur at $N = 6$ by Paolini and coworkers [60].

The isotopic substitution data of the $\text{He}_N\text{-HCN}$ clusters measured in this study contain significant discrepancies of calculated C–N bond lengths of clusters against accepted values of the bare chromophore. A comparison of Kraitchman substitution coordinates between light rotors (HCN and CO) and heavy rotors (OCS and N_2O) suggest the errors reside solely in the former class of rotors. Consequently, a theoretical study into the solvation dynamics of $\text{He}_N\text{-HCN}$ clusters is necessary to provide a thorough analysis of the helium density distribution and superfluid fraction.

CHAPTER 4: CONCLUDING REMARKS

The construction and optimization of a next generation Fourier-transform microwave spectrometer was successively completed. This chirped-pulse FTMW instrument, originally designed by the Pate group [116, 117] with modifications made by Grubbs *et al.* [119], exploits the transient phenomenon of fast passage, where the excitation frequency is linearly swept through molecular resonance on a time scale short compared to relaxation processes [115]. Currently the CP-FTMW spectrometer built in the Jäger group is capable of exciting transitions within a spectral window of 2 GHz.

A brief theoretical treatment of fast passage transition dynamics using the optical Bloch equations was also provided. Results from numerical integration of Equations 2.36a-c predicted a strong dependence of signal intensity on both the molecular system's Rabi frequency and the chirp sweep rate. It appears, based on this information, that the sweep rate must be adjusted for a particular transition dipole moment to optimally polarize a molecular ensemble.

In order to study small $\text{He}_N\text{-HCN}$ clusters, an affordable, high purity source of HCN gas was required. This was accomplished by locally synthesizing hydrogen cyanide under an inert helium atmosphere. The procedure was extended to produce a total of five isotopologues ($\text{H}^{12}\text{C}^{14}\text{N}$, $\text{D}^{12}\text{C}^{14}\text{N}$, $\text{H}^{13}\text{C}^{14}\text{N}$, $\text{H}^{12}\text{C}^{15}\text{N}$, and $\text{D}^{13}\text{C}^{14}\text{N}$) with excellent yields of 85–90%. To help limit the environmental impact and, of course, the workplace hazards that would ensue if HCN gas were released, a thorough procedure for the safe disposal of excess hydrogen cyanide was implemented and strictly followed.

Finally, the high resolution microwave spectra of the end-over-end $J = 1-0$ transition of small $\text{He}_N\text{-HCN}$ clusters and their isotopologues were measured. These weakly bound clusters were generated in a seeded supersonic jet-expansion, with observed clusters ranging in size from $N = 1$ up to 6 (or, in the case of DCN, up to $N = 7$). The CP-FTMW spectrometer provided initial survey scans in the

frequency region of 8–18 GHz and correct intensity information. The latter was used to confirm cluster assignments using pressure dependency experiments. In addition to measuring the high resolution spectra, the Balle-Flygare FTMW spectrometer was used to search for clusters with transitions frequencies greater than 18 GHz.

Analysis of spectroscopic constants revealed the first signs of microscopic superfluidity in helium solvated HCN. This is evidenced by the turnaround point in B_{eff} versus N occurring suddenly at $N = 3$ and is followed by a rapid increase in the effective rotational constants with $N \geq 4$. This suggests that a significant amount of decoupling of angular momenta is occurring between the helium density and the HCN probe. In order to better compare the experimental rotational constants against the quantum Monte Carlo simulations [59-61], this study needs to be extended to larger cluster sizes. This would give a better prediction of the behaviour of B_{eff} as the cluster evolves into a solvated system.

It is rather unfortunate that the extreme *floppiness* of these clusters prevents the extraction of accurate structural information from the rich isotopic data obtained in this study. That being said, the hyperfine structure analyses of the ^{14}N nuclear quadrupole coupling constants seem to reveal promising results. However, with limited experimental data available and the lack of theoretical work, it is difficult to properly assess their potential as delicate probes of the local helium density distribution. Hope now lies in the hands of theoreticians, as this study undoubtedly provides valuable experimental information on the rotational dynamics of helium solvated rotors lying in the intermediate regime.

BIBLIOGRAPHY

- [1] J.F. Allen, A.D. Misener, *Nature*, 141 (1938) 75.
- [2] P. Kapitza, *Nature*, 141 (1938) 74.
- [3] D.D. Osheroff, W.J. Gully, R.C. Richards, D.M. Lee, *Phys. Rev. Lett.*, 29 (1972) 920.
- [4] D.D. Osheroff, R.C. Richards, D.M. Lee, *Phys. Rev. Lett.*, 28 (1972) 885.
- [5] A.B. Migdal, *Nuclear Physics*, 13 (1959) 655.
- [6] D.R. Tilley, J. Tilley, *Superfluidity and Superconductivity*, 3rd ed., Institute of Physics, Philadelphia, 1990.
- [7] J.F. Allen, H. Jones, *Nature*, 141 (1938) 242.
- [8] B.V. Rollin, F. Simon, *Physica*, 6 (1939) 219.
- [9] T. Guénault, *Basic Superfluids*, Taylor & Francis, New York, 2003.
- [10] F. London, *Nature*, 141 (1938) 643.
- [11] J. Bardeen, L.N. Cooper, J.R. Schrieffer, *Phys. Rev.*, 108 (1957) 1175.
- [12] E.L. Andronikashvili, *Zh. eksp. teor. Fiz.*, 16 (1946) 780.
- [13] S. Goyal, D.L. Schutt, G. Scoles, *Phys. Rev. Lett.*, 69 (1992) 933.
- [14] F. Stienkemeier, K.K. Lehmann, *J. Phys. B: At. Mol. Opt. Phys.*, 39 (2006) R127.
- [15] J.P. Toennies, A.F. Vilesov, *Angew. Chem. Int. Ed.*, 43 (2004) 2622.
- [16] M.Y. Choi, G.E. Douberly, T.M. Falconer, W.K. Lewis, C.M. Lindsay, J.M. Merritt, P.L. Stiles, R.E. Miller, *Int. Rev. Phys. Chem.*, 25 (2006) 15.
- [17] J.P. Toennies, A.F. Vilesov, K.B. Whaley, *Physics Today*, 54 (2001) 31.
- [18] M. Hartmann, A. Lindinger, J.P. Toennies, A.F. Vilesov, *Chem. Phys.*, 239 (1998) 139.
- [19] S. Grebenev, B.G. Sartakov, J.P. Toennies, A.F. Vilesov, *Science*, 289 (2000) 1532.
- [20] S. Grebenev, B.G. Sartakov, J.P. Toennies, A.F. Vilesov, *J. Chem. Phys.*, 132 (2010) 064501.

- [21] K. Nauta, R.E. Miller, *Science*, 283 (1999) 1895.
- [22] M. Hartmann, R.E. Miller, J.P. Toennies, A. Vilesov, *Phys. Rev. Lett.*, 75 (1995) 1566.
- [23] S. Grebenev, J.P. Toennies, A.F. Vilesov, *Science*, 279 (1998) 2083.
- [24] E. Lee, D. Farrelly, K.B. Whaley, *Phys. Rev. Lett.*, 83 (1999) 3812.
- [25] Y. Kwon, P. Huang, M.V. Patel, D. Blume, K.B. Whaley, *J. Chem. Phys.*, 113 (2000) 6469.
- [26] Y. Kwon, D.M. Ceperley, K.B. Whaley, *J. Chem. Phys.*, 104 (1996) 2341.
- [27] K. Szalewicz, *Int. Rev. Phys. Chem.*, 27 (2008) 273.
- [28] A.C. Legon, E.J. Campbell, W.H. Flygare, *J. Chem. Phys.*, 76 (1982) 2267.
- [29] P.D. Soper, A.C. Legon, W.G. Read, W.H. Flygare, *J. Chem. Phys.*, 76 (1982) 292.
- [30] A.W. Castleman, R.G. Keesee, *Science*, 241 (1988) 36.
- [31] J. Tang, Y. Xu, A.R.W. McKellar, W. Jäger, *Science*, 297 (2002) 2030.
- [32] A.R.W. McKellar, Y. Xu, W. Jäger, *J. Phys. Chem. A*, 111 (2007) 7329.
- [33] A.R.W. McKellar, Y. Xu, W. Jäger, *Phys. Rev. Lett.*, 97 (2006) 183401.
- [34] J. Tang, A.R.W. McKellar, *J. Chem. Phys.*, 119 (2003) 5467.
- [35] Y. Xu, W. Jäger, *J. Chem. Phys.*, 119 (2003) 5457.
- [36] F. Paesani, A. Viel, F.A. Gianturco, K.B. Whaley, *Phys. Rev. Lett.*, 90 (2003) 073401.
- [37] S. Moroni, A. Sarsa, S. Fantoni, K.E. Schmidt, S. Baroni, *Phys. Rev. Lett.*, 90 (2003) 143401.
- [38] N. Blinov, X. Song, P.-N. Roy, *J. Chem. Phys.*, 120 (2004) 5916.
- [39] A.G. Suárez, J.A. Ramilowski, R.M. Benito, D. Farrelly, *Chem. Phys. Lett.*, 502 (2011) 14.
- [40] P.L. Raston, Y. Xu, W. Jäger, A.V. Potapov, L.A. Surin, B.S. Dumes, S. Schlemmer, *Phys. Chem. Chem. Phys.*, 12 (2010) 8260.
- [41] L. Surin, A. Potapov, B. Dumes, S. Schlemmer, Y. Xu, P. Raston, W. Jäger, *Phys. Rev. Lett.*, 101 (2008) 233401.
- [42] P. Cazzato, S. Paolini, S. Moroni, S. Baroni, *J. Chem. Phys.*, 120 (2004) 9071.

- [43] K. von Haefen, S. Rudolph, I. Simanovski, M. Havenith, R. Zillich, K. Whaley, *Phys. Rev. B*, 73 (2006) 054502.
- [44] T. Škrbić, S. Moroni, S. Baroni, *J. Phys. Chem. A*, 111 (2007) 7640.
- [45] J. Tang, A.R.W. McKellar, *J. Chem. Phys.*, 119 (2003) 754.
- [46] A.R.W. McKellar, *J. Chem. Phys.*, 128 (2008) 044308.
- [47] J. Tang, A.R.W. McKellar, *J. Chem. Phys.*, 121 (2004) 181.
- [48] C.J. Knapp, Y.J. Xu, W. Jäger, *J. Mol. Spectrosc.*, 268 (2011) 130.
- [49] S. Moroni, N. Blinov, P.-N. Roy, *J. Chem. Phys.*, 121 (2004) 3577.
- [50] Y. Xu, W. Jäger, J. Tang, A.R.W. McKellar, *Phys. Rev. Lett.*, 91 (2003).
- [51] Y. Xu, N. Blinov, W. Jäger, P.-N. Roy, *J. Chem. Phys.*, 124 (2006) 081101.
- [52] A.R.W. McKellar, *J. Chem. Phys.*, 127 (2007) 044315.
- [53] W. Topic, W. Jäger, N. Blinov, P.-N. Roy, M. Botti, S. Moroni, *J. Chem. Phys.*, 125 (2006) 144310.
- [54] J.L. Way, *Ann. Rev. Pharmacol. Toxicol.*, 24 (1984) 451.
- [55] A. Brack, *The Molecular Origins of Life: Assembling Pieces of the Puzzle*, Cambridge University Press, 1998.
- [56] K. Sorai, N. Nakai, N. Kuno, K. Nishiyama, *Publ Astron Soc Jpn*, 54 (2002) 179.
- [57] J. Tennyson, *Astronomical Spectroscopy: An Introduction to the Atomic and Molecular Physics of Astronomical Spectra*, World Scientific Pub Co Inc, 2010.
- [58] J. Tang, A.R.W. McKellar, F. Mezzacapo, S. Moroni, *Phys. Rev. Lett.*, 92 (2004) 145503.
- [59] A.A. Mikosz, J.A. Ramilowski, D. Farrelly, *J. Chem. Phys.*, 125 (2006) 014312.
- [60] S. Paolini, S. Fantoni, S. Moroni, S. Baroni, *J. Chem. Phys.*, 123 (2005) 114306.
- [61] A. Viel, K.B. Whaley, *J. Chem. Phys.*, 115 (2001) 10186.
- [62] A.G. Maki, *J. Phys. Chem. Ref. Data*, 3 (1974) 221.
- [63] E. Gail, S. Gos, R. Kulzer, J. Lorösch, A. Rubo, M. Sauer, *Cyano Compounds, Inorganic*, in: *Ullmann's Encyclopedia of Industrial Chemistry*, Wiley-VCH Verlag GmbH & Co. KGaA, 2000.

- [64] S. National Research Council . Committee on Prudent Practices for Handling, D.o.C.i. Laboratories, Prudent Practices in the Laboratory: Handling and Disposal of Chemicals, National Academy Press, 1995.
- [65] R. Brooker, E. Widmaier, L. Graham, P. Stiling, Biology, McGraw-Hill Companies, Inc., 2010.
- [66] B. Vennesland, E.M.B. Organization, Cyanide in biology, Academic Press, 1981.
- [67] R. Cipollone, P. Ascenzi, P. Tomao, F. Imperi, P. Visca, J. Mol. Microbio. Biotechn., 15 (2008) 199.
- [68] T. Wadsten, S. Andersson, Acta Chem. Scand., 13 (1959) 1069.
- [69] W.F. Giauque, R.A. Ruehrwein, J. Am. Chem. Soc., 61 (1939) 2626.
- [70] E.H. Gause, P.D. Montgomery, J. Chem. Eng. Data, 5 (1960) 351.
- [71] A.J. Fillery-Travis, A.C. Legon, L.C. Willoughby, Proc. R. Soc. Lond. A, 396 (1984) 405.
- [72] M.H. Moore, R.L. Hudson, Icarus, 161 (2003) 486.
- [73] P.A. Gerakines, M.H. Moore, R.L. Hudson, Icarus, 170 (2004) 202.
- [74] B. A.P, Chem. Phys. Lett., 61 (1979) 532.
- [75] Y. Xu, W. Jäger, Chem. Phys. Lett., 350 (2001) 417.
- [76] L.W. Buxton, E.J. Campbell, W.H. Flygare, Chem. Phys., 56 (1981) 399.
- [77] T.J. Balle, W.H. Flygare, Rev. Sci. Instrum., 52 (1981) 33.
- [78] A.C. Legon, Ann. Rev. Phys. Chem., 34 (1983) 275.
- [79] P.W. Atkins, Physical Chemistry, 6th ed., W. H. Freeman and Co., New York, 1999.
- [80] T.A. Miller, Science, 223 (1984) 545.
- [81] A. Amirav, U. Even, J. Jortner, Chem. Phys., 51 (1980) 31.
- [82] E.J. Campbell, L.W. Buxton, T.J. Balle, M.R. Keenan, W.H. Flygare, J. Chem. Phys., 74 (1981) 829.
- [83] W. Gordy, W.V. Smith, R.F. Trambarulo, Microwave Spectroscopy, Dover Publications, 1966.
- [84] C.H. Townes, A.L. Schawlow, Microwave Spectroscopy, Dover Publications, 1955.

- [85] D.A. McQuarrie, *Quantum Chemistry*, 2nd ed., University Science Books, Sausalito, California, 2008.
- [86] E.J. Campbell, L.W. Buxton, A.C. Legon, *J. Chem. Phys.*, 78 (1983) 3483.
- [87] S. Drucker, F.-M. Tao, W. Klemperer, *J. Phys. Chem.*, 99 (1995) 2646.
- [88] G.T. Fraser, A.S. Pine, *J. Chem. Phys.*, 91 (1989) 3319.
- [89] T.C. Germann, T. Emilsson, H.S. Gutowsky, *J. Chem. Phys.*, 95 (1991) 6302.
- [90] H.S. Gutowsky, J.D. Keen, T.C. Germann, T. Emilsson, J.D. Augspurger, C.E. Dykstra, *J. Chem. Phys.*, 98 (1993) 6801.
- [91] K.R. Leopold, G.T. Fraser, F.J. Lin, J. D. D. Nelson, W. Klemperer, *J. Chem. Phys.*, 81 (1984) 4922.
- [92] C.H. Townes, B.P. Dailey, *J. Chem. Phys.*, 17 (1949) 782.
- [93] M.R. Keenan, T.K. Minton, A.C. Legon, T.J. Balle, W.H. Flygare, *Proc. Natl. Acad. Sci. USA*, 77 (1980) 5583.
- [94] M.R. Keenan, L.W. Buxton, E.J. Campbell, A.C. Legon, W.H. Flygare, *J. Chem. Phys.*, 74 (1981) 2133.
- [95] P.D. Soper, A.C. Legon, W.H. Flygare, *J. Chem. Phys.*, 74 (1981) 2138.
- [96] E.J. Campbell, A.C. Legon, W.H. Flygare, *J. Chem. Phys.*, 78 (1983) 3494.
- [97] J. Kraitchman, *Am. J. Phys.*, 21 (1953) 17.
- [98] J.D. Macomber, *The Dynamics of Spectroscopic Transitions: Illustrated by Magnetic Resonance and Laser Effects*, Wiley, 1976.
- [99] H. Dreizler, *Mol. Phys.*, 59 (1986) 1.
- [100] H. Dreizler, *Ber. Bunsen. Phys. Chem.*, 99 (1995) 1451.
- [101] W.H. Flygare, *Molecular Structure and Dynamics*, Prentice-Hall, Englewood Cliffs, New Jersey, 1978.
- [102] J.-U. Grabow, *Fourier Transform Microwave Spectroscopy Measurement and Instrumentation*, in: *Handbook of High-resolution Spectroscopy*, John Wiley & Sons, Ltd., 2011.
- [103] B.W. Shore, *Manipulating Quantum Structures Using Laser Pulses*, Cambridge University Press, 2011.
- [104] F. Bloch, *Phys. Rev.*, 70 (1946) 460.
- [105] R.P. Feynman, F.L. Vernon, R.W. Hellwarth, *J. Appl. Phys.*, 28 (1957) 4.

- [106] L. Allen, J.H. Eberly, *Optical Resonance and Two-Level Atoms*, John Wiley & Sons, Inc., New York, 1975.
- [107] J. Ekkers, W.H. Flygare, *Rev. Sci. Instrum.*, 47 (1976) 448.
- [108] R.R. Ernst, W.A. Anderson, *Rev. Sci. Instrum.*, 37 (1966) 93.
- [109] J.C. McGurk, T.G. Schmalz, W.H. Flygare, *Adv. Chem. Phys.*, 25 (1974) 68.
- [110] Y. Xu, W. Jäger, *J. Chem. Phys.*, 106 (1997) 7968.
- [111] J.-U. Grabow, W. Stahl, *Z. Naturforsch.*, 45 (1990) 1043.
- [112] U. Andresen, H. Dreizler, J.-U. Grabow, W. Stahl, *Rev. Sci. Instrum.*, 61 (1990) 3694.
- [113] E.J. Campbell, L.W. Buxton, T.J. Balle, W.H. Flygare, *J. Chem. Phys.*, 74 (1981) 813.
- [114] M.B. Steer, *Microwave and RF Design - A Systems Approach*, SciTech Publishing, Raleigh, NC, 2010.
- [115] J.C. McGurk, T.G. Schmalz, W.H. Flygare, *J. Chem. Phys.*, 60 (1974) 4181.
- [116] G.G. Brown, B.C. Dian, K.O. Douglass, S.M. Geyer, B.H. Pate, *J. Mol. Spectrosc.*, 238 (2006) 200.
- [117] G.G. Brown, B.C. Dian, K.O. Douglass, S.M. Geyer, S.T. Shipman, B.H. Pate, *Rev. Sci. Instrum.*, 79 (2008) 053103.
- [118] B.C. Dian, G.G. Brown, K.O. Douglass, B.H. Pate, *Science*, 320 (2008) 924.
- [119] G.S. Grubbs, II, C.T. Dewberry, K.C. Etchison, K.E. Kerr, S.A. Cooke, *Rev. Sci. Instrum.*, 78 (2007) 096106.
- [120] S.P. Dempster, O. Sukhorukov, Q.-Y. Lei, W. Jäger, "Rotational spectroscopic study of hydrogen cyanide embedded in small ^4He clusters", submitted to *J. Chem. Phys.*, 2012.
- [121] R.E. Bumgarner, G.A. Blake, *Chem. Phys. Lett.*, 161 (1989) 308.
- [122] H.S. Gutowsky, E. Arunan, T. Emilsson, S.L. Tschopp, C.E. Dykstra, *J. Chem. Phys.*, 103 (1995) 3917.
- [123] H.S. Gutowsky, T.D. Klots, C.E. Dykstra, *J. Chem. Phys.*, 93 (1990) 6216.
- [124] T.D. Klots, C.E. Dykstra, H.S. Gutowsky, *J. Chem. Phys.*, 90 (1989) 30.

- [125] K. Tanaka, S. Bailleux, A. Mizoguchi, K. Harada, T. Baba, I. Ogawa, M. Shirasaka, *J. Chem. Phys.*, 113 (2000) 1524.
- [126] K. Harada, K. Tanaka, T. Tanaka, S. Nanbu, M. Aoyagi, *J. Chem. Phys.*, 117 (2002) 7041.
- [127] R.R. Toczyłowski, F. Doloresco, S.M. Cybulski, *J. Chem. Phys.*, 114 (2001) 851.
- [128] K. Nauta, R.E. Miller, *Phys. Rev. Lett.*, 82 (1999) 4480.
- [129] A. Conjusteau, C. Callegari, I. Reinhard, K.K. Lehmann, G. Scoles, *J. Chem. Phys.*, 113 (2000) 4840.
- [130] A.G. Maki, *J. Mol. Spectrosc.*, 58 (1975) 308.
- [131] C. Callegari, A. Conjusteau, I. Reinhard, K.K. Lehmann, G. Scoles, F. Dalfovo, *Phys. Rev. Lett.*, 83 (1999) 5058.
- [132] S. Baroni, S. Moroni, *Phys. Rev. Lett.*, 82 (1999) 4745.
- [133] S.L. Holmgren, M. Waldman, W. Klemperer, *J. Chem. Phys.*, 67 (1977) 4414.
- [134] K.M. Atkins, J.M. Hutson, *J. Chem. Phys.*, 105 (1996) 440.
- [135] K.A. Peterson, G.C. McBane, *J. Chem. Phys.*, 123 (2005) 084314.
- [136] A.R.W. McKellar, *J. Chem. Phys.*, 125 (2006) 164328.
- [137] W.C. Topic, Ph.D. Thesis, Department of Chemistry, University of Alberta, Edmonton, 2006.
- [138] J.K.G. Watson, *J. Mol. Spectrosc.*, 48 (1973) 479.
- [139] P.L. Raston, W. Jäger, H. Li, R.J. Le Roy, P.-N. Roy, *Phys. Rev. Lett.*, 108 (2012) 063411.